PhD Dissertation

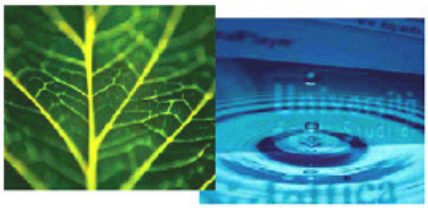

International Doctorate School in Information and Communication Technologies

DISI - University of Trento

ALGORITHMS AND PERFORMANCE ANALYSIS FOR SYNCHROPHASOR AND GRID STATE ESTIMATION

Grazia Barchi

Advisor:

Prof. Dario Petri

University of Trento

January 2015

Dedicated to everyone I love,
especially to my two grandmothers

Abstract

The electrical quantities of future power networks are expected to exhibit strong fluctuations caused by dynamic bidirectional energy flows transferred from/to a multitude of "prosumers". Such variations have to be accurately measured in real-time either for efficient power distribution or for safety and protection purposes. This task can be accomplished by the Phasor Measurement Units (PMUs), which measure the phasor of voltage or current waveforms synchronized to the Coordinated Universal Time (UTC). Accuracy of synchrophasor measurements is one of the many open challenges that need to be addressed in order to guarantee smart grid reliability and availability. Synchrophasor measurement has gained an undisputed relevance in the research community working on power delivery issues for various reasons. Among them, state estimation (SE) of both transmission and distribution networks is one of the most important. Within this general context, this dissertation covers two complementary topics.

In the first part, starting from the concept of synchrophasor and from the definition of the parameters to evaluate PMU performances, useful guidelines to design a filter-based synchrophasor estimator are provided. Afterwards, an extensive performance comparison of some state-of-the-art synchrophasor estimation algorithms is reported in most of the static and dynamic conditions described in the IEEE Standards C37.118.1-2011. Also, a novel technique able to address both static and dynamic disturbances is presented and analyzed in depth. In this respect, special attention is devoted to phasor angle estimation accuracy, which is particularly important for active distribution networks.

The second part of the dissertation is focused on the role and the impact of PMUs for grid state estimation. After recalling the state estimation problem and the traditional Weighted Least Square (WLS) technique to solve it, a general uncertainty sensitivity analysis to different types of measurements is introduced and justified both theoretically and through simulations. Afterwards, the effect of a growing number of PMUs on WLS-based state estimation uncertainty is evaluated as a function of instrumental accuracy and line parameters tolerance. Finally, a Bayesian linear state estimator (BLSE) based on a linear approximation of power flow equations for distribution networks is presented. The main advantage of BLSE is that in most cases it is so accurate as the WLS technique, but it is computationally lighter, faster and more stable from the numerical point of view.

Keywords– *Phasor Measurement Unit, synchrophasor estimation, state estimation, power system measurement, uncertainty.*

Acknowledgements

This work is the conclusion of three years of passionate research, which has involved also several other people.

First of all, I would like to express my gratitude to my advisor, Prof. Dario Petri, for his guidance and motivation during the whole PhD program. I would like to thank Dr. David Macii and Dr. Daniele Fontanelli for their suggestions and precious support.

Special thanks goes to Prof. Kameshwar Poolla and to Prof. Alexandra von Meier for the opportunity that they gave me to be a visiting scholar at the University of California, Berkeley; and to Prof. Luca Schenato, Dr. Reza Arghandeh and Dr. Guido Cavraro for the fruitful scientific collaboration while I was there.

Finally, I would like to thank my family and my friends for their endless support and the colleagues who I have met in these years.

Grazia

Publications as author and co-author

International Journals

[J.1] **G. Barchi**, D. Fontanelli, D. Macii and D. Petri, "On the Accuracy of Phasor Angle Measurements in Power Networks", *on IEEE Trans. Instrumentation and Measurement*,vol., no., pp., . 2015

[J.2] **G. Barchi**, D. Macii, D. Belega and D. Petri, "Performance of synchrophasor estimators in transient conditions: A comparative analysis", *IEEE Trans. Instrumentation and Measurement*,vol.62, no.9, pp.2410-2418, Sept. 2013

[J.3] **G. Barchi**, D. Macii and D. Petri, "Synchrophasor Estimators Accuracy: A Comparative Analysis," *IEEE Trans. Instrumentation and Measurement*,vol.62, no.5, pp.963-973, May 2013

International Conference Proceedings

[I.1] L. Schenato, **G. Barchi**, D. Macii, R. Arghandeh, K. Poolla and A. Von Meier, "Bayesian Linear State Estimation using Smart Meters and PMUs Measurements in Distribution Grids," *IEEE International Conference on Smart Grid Communications 2014*, pp. 1-6, Venice, Italy, 3-6 Nov 2014.

[I.2] D. Macii, **G. Barchi** and D. Petri,"Uncertainty Sensitivity Analysis of WLS-based Grid State Estimators," *IEEE International Workshop on Applied Measurements for Power Systems*, pp. 1-6, Aachen, Germany, 24-27 Sep 2014.

[I.3]D. Macii,**G. Barchi** and L.Schenato, "On the Role of Phasor Measurement Units for Distribution System State Estimation," *IEEE Workshop on Environmental, Energy and Structural Monitoring*, pp. 1-6, Naples, Italy, 17-18 Sep 2014.

[I.4]**G. Barchi**, D. Fontanelli, D. Macii and D. Petri, "Frequency-domain Phase Measurement Algorithms for Distribution Systems," *IEEE International Instrumentation and Measurement Technology Conference (I2MTC)*, pp. 1828-1833, Montevideo, Uruguay, 12-15 May 2014.

[I.5]**G. Barchi**, D. Macii, and D. Petri, "Phasor Measurement Units for Smart Grids: Estimation Algorithms and Performance Issues", *AEIT Meeting 2013*, Oct. 2013.

[I.6]D. Macii, **G. Barchi** and D. Petri, "Design Guidelines of Digital Filters for Synchrophasor Estimation", *IEEE International Instrumentation and Measurement Technology Conference (I2MTC)*, pp.1579-1584, May 2013.

[I.7]**G. Barchi**, D. Macii and D. Petri,"Effect of transient conditions on DFT-based synchrophasor estimator performance", *IEEE International Workshop on Applied Measurements for Power Systems (AMPS)*, pp. 1-6, Sep. 2012.

[I.8] **G. Barchi** and D. Petri,"An improved dynamic synchrophasor estimator", *IEEE International Energy Conference and Exhibition (ENERGYCON)*, pp. 812-817, Sep. 2012.

[I.9]**G. Barchi**, D. Macii and D. Petri, "Accuracy of One-cycle DFT-based Synchrophasor Estimators in Steady-state and Dynamic Conditions", *IEEE International Instrumentation and Measurement Technology Conference (I2MTC)*, pp. 1529-1534, May 2012.

Contents

Chapter 1

Introduction

1.1 Context of the research

The worldwide growing demand for electrical energy and, at the same time, the compelling need for reducing carbon dioxide emissions, have recently created new challenges not only in the traditional area of energy generation from renewable sources, but also in power flow control and management. In 2008 the yearly electricity production worldwide was in the order of about 15,000 billion kWh, but a large increment is envisioned in the near future especially in those countries (most notably India and China) that have been experiencing an outstanding economic growth for several years [1]. Of course, the emissions of carbon dioxide related to energy consumption have enormously grown as well in the same countries (see Fig. 1.1), thus leading to a significant global increment of greenhouse gas emissions, in spite of the increasingly aggressive policies for their reduction in Europe and North America. While, till now, more than 50% of the primary energy consumption per capita has been due to European or North American users (see Fig. 1.2), this situation is expected to change drastically in the near future as soon as large masses of people with improved economic conditions will have steady access to electricity. It is wellknown that an increasing energy demand, greenhouse gas emission can be reduced only with a massive deployment of generators based on renewable sources. Even if their penetration has constantly grown in the last 25 years, especially in Asia as shown in Fig. 1.3, the way towards a fully sustainable energetic scenario is still very long. In this context, in industrialized countries the forthcoming widespread deployment of distributed micro-generators and energy storage elements will turn typical consumers into significant producers of electrical energy, thus substantially changing the present structure of the power grid [2]. In particular, the old paradigm based on a few large power plants and on quite different passive networks for transmission and distribution is expected to be replaced by active networks in which all the actors involved will enable bidirectional power

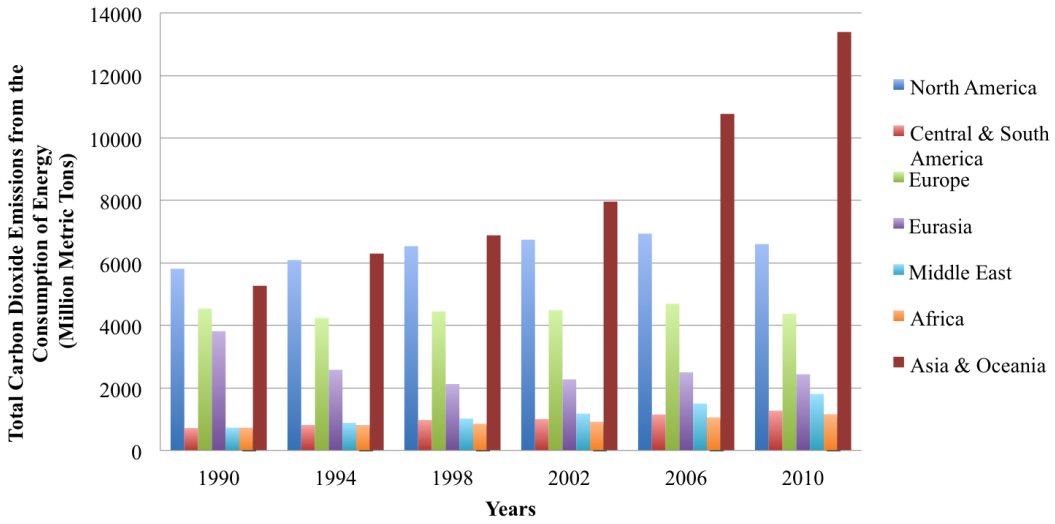

Figure 1.1: Total carbon dioxide emissions from the consumption of energy (millions metric tons) [Source: Energy Information Administration, U.S. Government]

flows supported by suitable infrastructures for both communication and protection. The introduction of information and communication technologies (ICT) in the power networks creates the so-called smart power grids. In the near future the smart grid will allow us to integrate small production plants and new loads devices (e.g. the electric vehicles) thus giving to prosumers (producers-consumers) an active role in electricity pricing. At the same time continuous service, adequate amplitude and frequency stability at the minimum cost, security, and an acceptable impact on the environment will have to be ensured and possibly improved. The term *continuous service* refers mainly to reliability and availability of the network [3]. Indeed, in the recent years much research work has focused on solutions to increase transmission capacity with a low environmental impact, to improve system operation after the integration of variable energy resources (VERs) such as wind-based or photovoltaic plants [4], and to avoid catastrophic black-outs like those happened in the North-East of U.S. and in Italy in 2003.

Traditionally, grid monitoring relies on Supervisory Control and Data Acquisition (SCADA) systems that collect information related to breaker status as well as measurement data of meaningful electrical quantities of the network (such as bus voltages or injected currents) through Remote Terminal Units (RTUs). On the basis of such data, various countermeasures can be taken in response to a particular event. Unfortunately, while a SCADA system typically takes several seconds to support decisions, today some events require much faster response times. For such reasons, new advanced Wide Area Monitoring/Measurement System (WAMS) are used for monitoring, protection and control services.

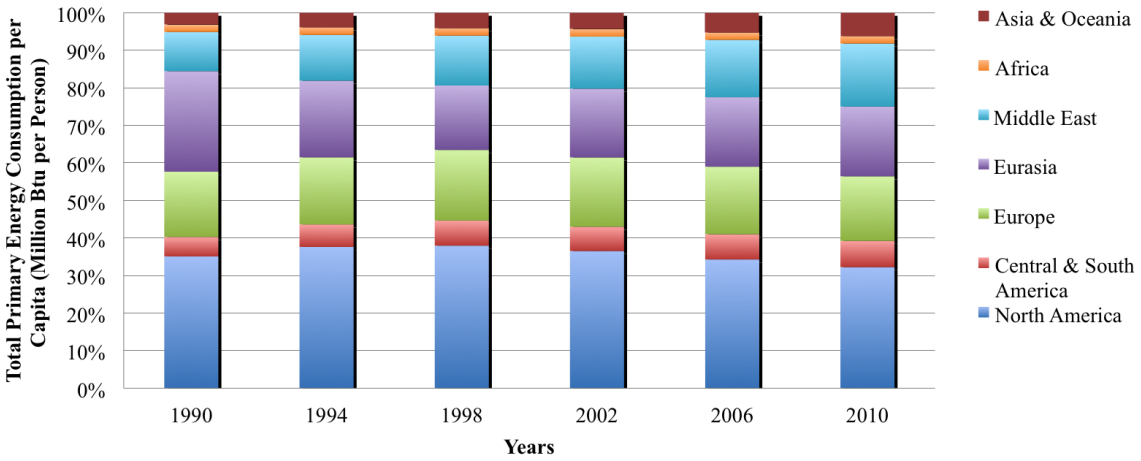

Figure 1.2: Total primary energy consumption per capita (millions Btu per person) [Source: Energy Information Administration, U.S. Government]

The WAMS is an infrastructure able to acquire data from strategic points of the grid. The increasing diffusion of Distributed Generation (DG), i.e. small production plants based on renewable energy sources, requires novel measurement systems and techniques characterized by a good trade-off between accuracy and responsiveness [5]. For this reason, in the last years various advanced measurement instruments have been introduced at the transmission and distribution level in order to reinforce the existing infrastructure. Among them, the so-called Phasor Measurement Units (PMUs) play a central role in WAMS. Generally speaking, a PMU is able to measure the phasors of electrical quantities (i.e. currents or voltages) over intervals of various length synchronized to the Coordinated Universal Time (UTC) [6]. The reference time is usually provided by a Global Positioning System (GPS) receiver. Using multiple PMUs in different points allows us to take a snapshot of the state of the network at a given time. The main advantages of the PMU-based measurements compared to the conventional current/voltage measurements are: higher accuracy in both magnitude and phase, availability of synchronous data and fast reporting rates (i.e. ranging between about 10 Hz and 100 Hz). Unfortunately, such high rates (which are expected to grow further in the future) require to store and to manage huge amounts of data, thus creating serious scalability issues due to the *data tsunami* that could affect next-generation active distribution networks [7]. Because of this problem and of other economic or logistic reasons, at the moment the PMUs are supposed just to support and to complement other traditional measurement techniques, e.g. those based on smart meters. However, as soon as the active distribution networks will be available on a wide scale, cheaper PMUs with enhanced functionalities could be used directly to support multiple applications possibly using the same infrastructure, thus further boosting

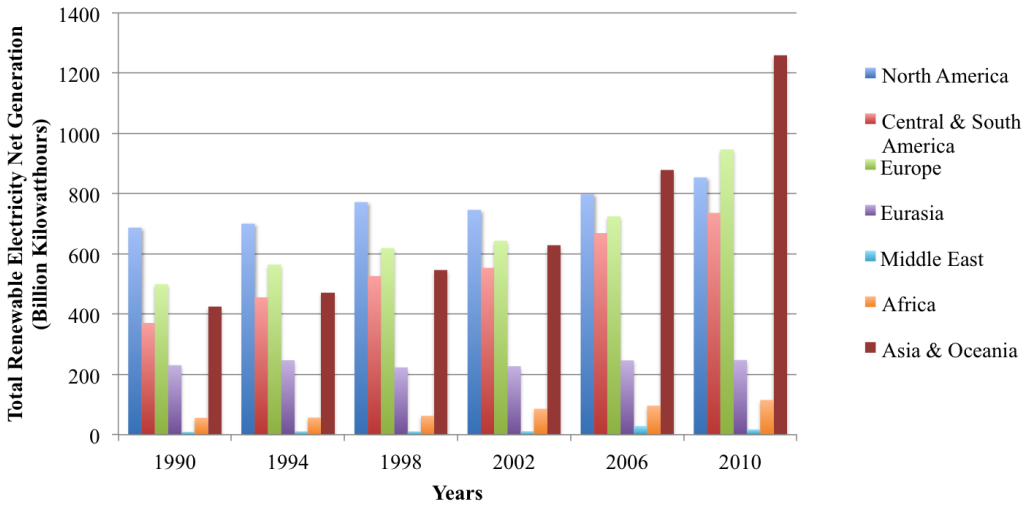

Figure 1.3: Total renewable electricity net generation (Billions kWh) [Source: Energy Information Administration, U.S. Government]

the role of this type of instruments. These applications include (but are not limited to) fast protection equipment (i.e. with response times in the order of few ms) [8], voltage stability and oscillation monitoring [9, 10], fault detection and location [11], islanding maneuvers [12, 13], state estimation [14] and load modeling [15].

1.2 Objectives and contribution of the research work

Next-generation PMUs are required to exhibit superior accuracy and responsiveness at lower costs. Also, they are supposed to measure not only phasors, but also waveform frequencies and frequency changes. Even if PMU performances are affected by different uncertainty sources, the estimation algorithm plays an essential role in instrument performance. Several novel estimation techniques have been developed in the last years in the attempt of both mitigating the effect of static disturbances (such as harmonics and inter-harmonics) and tracking fast phasor changes due to intrinsic variations of the network operating conditions. Due to the recent definition of various algorithms based on the so-called phasor dynamic model, a detailed comparison between their performances can be hardly found in the literature. So one of the primary goals of this research work is to fill at least partially this gap by presenting and testing quite famous estimation algorithms in a common and widely accepted framework: the conditions described in the IEEE Standards C37.118.1-2011 and its Amendment IEEE C37.118.1a-2014.

In addition, a novel estimator that exhibits high accuracy, good responsiveness and a reasonable computational complexity is described and analyzed. Special attention will

be devoted to the problem of phasor angle estimation, which is quite unexplored and is particularly important at the distribution level, where PMU deployment is expected to be massive in the near future.

The second part of the thesis covers a complementary aspect, namely the role of PMUs for grid state estimation, which is considered as one of the most relevant applications of synchrophasor measurements. Many works related to this topic already exist, but most of them focus on optimal PMU placement to maximize state estimation accuracy or to minimize the overall monitoring costs. In this thesis instead the emphasis is mainly on how the number and the accuracy of synchrophasor measurements influence state estimation especially at the distribution level. At first, a theoretical analysis of the sensitivity to measurement uncertainty of the well-known Weighted Least Squares (WLS) estimation technique is reported (properly supported by meaningful simulations) in order to identify what types of measurements are most critical for state estimation. Thus this analysis paves the way to a deeper understanding of the impact of PMUs on state estimation uncertainty in distribution systems. Then, a novel linear Bayesian state estimation algorithm relying on both PMU-based phasor measurements and real/reactive power pseudo-measurements is proposed in order to achieve reasonably accurate state estimates with less numerical problems and with a lower computation burden than using the WLS approach.

In conclusion, the thesis is structured as follows.

Chapter 2 deals with an overview of synchrophasor measurements and PMUs. At first, the common structure of PMUs is described, along with how the synchrophasor data are collected. Then, important definitions as well as some static and dynamic testing conditions based on the IEEE Standard C37.118.1-2011 are introduced. Such testing conditions will be also used in Chapter 3 and Chapter 4. Finally, some general guidelines to design a filter for synchrophasor estimation are reported.

In Chapter 3 three state-of-the-art techniques for synchrophasor estimation are described and their performances are extensively analyzed and compared under the steady-state and dynamic conditions reported in the IEEE Standard C37.118.1-2011.

In Chapter 4 a novel synchrophasor estimator is proposed and validated through simulations in most of the conditions reported in the Standard. In view of using this algorithm in PMUs for distribution systems (where a superior phase measurement accuracy is required), the phasor angle measurement accuracy alone is analyzed and compared with the accuracy of other two state-of-the-art algorithms.

In Chapter 5 the problem of state estimation is introduced and the classic static WLS state estimator is recalled. A sensitivity analysis to measurement uncertainty is performed to identify which kinds of measurements are preferable for state estimation to achieve observability when their number is minimum. In this way, the role of PMU-based

measurements in state estimation with respect to other traditional measurements is also partially clarified. This aspect is further analyzed in Chapter 6, which investigates more in depth how a growing number of PMUs and their accuracy affect grid state estimation accuracy. This analysis, mainly focused on distribution systems, paves the way to the definition of a novel Bayesian and Linear State Estimation (BLSE) algorithm, which proves to be faster and more numerically stable than the traditional WLS-based approach.

Finally, Chapter 7 summarizes the main results of the research work and provides an overview of ongoing and future activities.

Chapter 2

Synchrophasors and PMUs

As stated in Chapter 1, the PMUs are the key elements of the WAMS, as they measure the phasors of different waveforms over a wide area at the same time. This chapter presents at first an overview of a common PMU architecture which the specific function of each block. Then, the main concepts taken from the current synchrophasor Standard IEEE C37.118.1-2011 and used in the rest of the thesis are introduced. At last some guidelines to design suitable filters for synchrophasor measurement are proposed.

2.1 Phasor Measurement Unit

The first prototypes of PMUs were built at the Virginia Tech in the early 1980s. At present, PMUs by different manufacturers may differ in various important aspects. Nonetheless, a quite general PMU architecture is shown in Fig. 2.1 [6]. The input waveform, i.e.

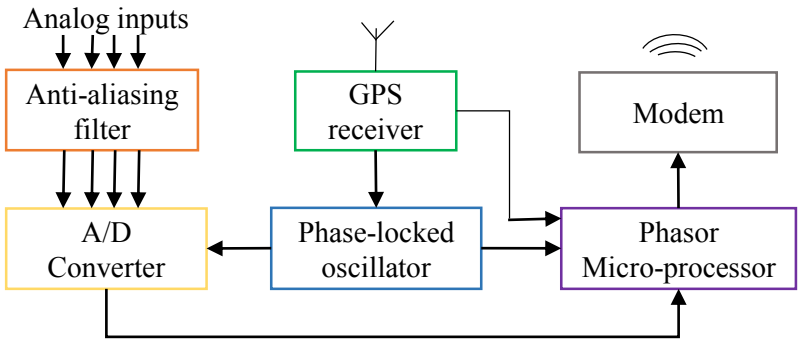

Figure 2.1: A common Phasor Measurement Unit architecture. Source: [6].

Part of this chapter was published in
D. Macii, G. Barchi and D. Petri, "Design Guidelines of Digital Filters for Synchrophasor Estimation", *IEEE International Instrumentation and Measurement Technology Conference (I2MTC)*, pp.1579-1584, May 2013.

voltage or current, is acquired by a signal conditioning module (that typically just consists of an anti-aliasing filter), followed by an Analog-to-Digital Converter (ADC). The sampling clock signal (with a frequency in the order of tens of kilo-samples/second) is phase-locked with a train of pulses synchronized to the UTC through a GPS receiver or through wired synchronization protocols such as IRIG-B or the Precision Time Protocol (PTP) [16]). The digitized electrical waveform is sent to an embedded processing component, such as a microprocessor (μP), which calculates the synchronized phasor using a specific estimation algorithm, frequency and rate of change of frequency (ROCOF). Additionally, it relies on the synchronization block to time-stamp the measurements. Finally, the estimated values are transmitted to other PMUs or the Phasor Data Concentrators (PDCs), which are able to collect data from different PMUs and align their in time. Generally, four types of files are exchanged between PMUs, i.e. configuration, header and data files. In addition, command files are used to control the PMUs from a higher level of the network hierarchy [17]. The PMUs are placed and installed in power system substations. In order to use PMUs measurement in different applications (e.g. state estimation, fault detection, stability estimation, control...), they have to be controlled remotely. For such reasons a hierarchical architecture that involves PMUs, communication systems and PDC, as shown in Fig. 2.2 has to be realized. The PMUs measurement data can be stored locally for diagnostic purposes or can be sent to PDCs for high-level filtering and monitoring. Many applications require data from several PMUs. After bad data exclusion, time-stamps alignment, coherent records are gathered by the PDCs themselves. In order to extend the PDCs data-gathering capability the Super Data Concentrator or direct (monitoring system/station) is used at a higher hierarchical level.

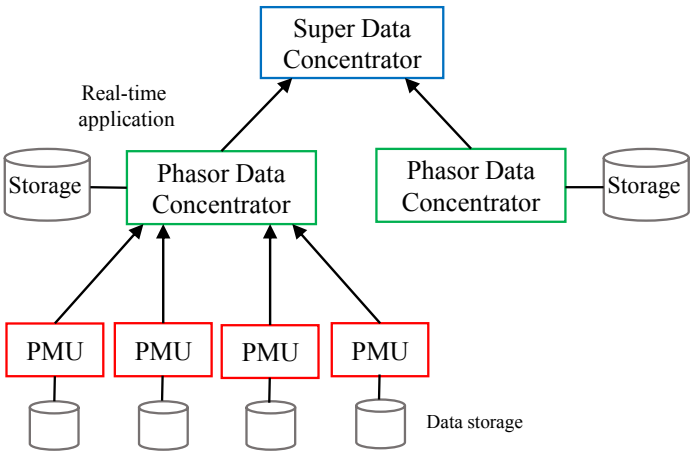

Figure 2.2: Phasor measurement systems architecture [6].

2.2 Concept of synchrophasor in the series of standards IEEE C37.118-2011

The goal of PMU is to perform real-time and accurate measurements of the phasors synchronized to the UTC, in order to track possible variations, to detect abnormal phenomena and to support control operations in power grid. However, to operate correctly it is necessary that synchrophasor measurements and data messaging are compliant with the definition and the performance requirements of suitable Standards. The synchrophasor definition was standardized for the first time in 1995 in the IEEE Std 1344. This standard introduces also concepts such time accuracy, synchronization to UTC and requirements for waveform sampling. Ten years later, more complete and meaningful changes were introduced in the IEEE Std C37.118-2005. This specifies how to evaluate the measurement performance and the message structure for synchrophasor data. It defines the Total Vector Error (TVE) as the main accuracy index and its limits in steady-state conditions in order to fulfill the compliance requirements. However the need to analyze synchrophasor performance also under dynamic conditions (i.e in presence of amplitude/phase variations or frequency ramp) led to the current and revised version in late 2011.

The new standard, IEEE Std C37.118-2011, is divided in two parts: the first one, i.e IEEE Std C37.118.1-2011 in the following simply called "the Standard" [18], provides the definitions of synchrophasor, waveform frequency and rate of change of frequency (ROCOF). Moreover it deals with the compliance boundaries and tests to evaluate the performance of PMUs under steady-state and dynamic conditions. The second part, IEEE Std C37.118.2-2011 deals with the synchrophasor data transfer and data formats [17]. Two performance classes are defined in the Standard IEEE C37.118.1-2011, i.e. *P-class* and *M-class*, in order to meet orthogonal applicative needs. The *P-class* PMUs are mainly oriented to those applications requiring a fast measurement response time (e.g. for safety-critical, protection purposes). Conversely, the *M-class* PMUs are used when measurement accuracy is more important than measurement speed. All the compliance tests under steady-state and dynamic conditions are specified in the Standard. Recently, an amendment of the Standard, called IEEE C37.118.1a-2014 was published in order to fix some inconsistencies and to relax some constraints difficult to meet especially related to frequency and ROCOF estimation (see 2.2.1). In spite of the recent publication of Amendment IEEE Std C37.118.1a-2014 in the rest of the dissertation the IEEE Std C37.118.1-2011 will be considered as reference document, except in the few particular cases.

According to the Standard, the PMU supports a reporting rate at multiple or submultiples of the nominal frequency. The compliant reporting rate values, expressed in

Frames per second, for 50 Hz and 60 Hz systems are listed in the Tab.2.1. Other reporting rates(100 frames/s or 120 frames/s or rates lower than 10 frames/s, such as 1 frames/s), are also encouraged.

Table 2.1: PMU reporting rates[18].

System frequency	50Hz			60 Hz					
Reporting rates (F_s - frames per second)	10	25	50	10	12	15	20	30	60

In the following the main concepts introduced in the Standard and used in the rest of dissertation are presented and explained.

2.2.1 Synchrophasor, frequency and ROCOF definitions

Model signal and synchrophasor

In AC power systems an electrical waveform (i.e. current or voltage) $x(t)$ of nominal frequency f_0 (i.e. 50 Hz or 60 Hz) can be expressed as

$$x(t) = A\cos(2\pi f_0 t + \phi) \tag{2.1}$$

where A is the amplitude and ϕ is the initial phase. A common representation of (2.1) through its complex static phasor is defined as

$$\bar{X} = \frac{A}{\sqrt{2}} e^{j\phi}. \tag{2.2}$$

A synchronized phasor or synchrophasor of an electrical signal in (2.1) is the value $\bar{X}$ in (2.2) at a known reference time, t_r, synchronized to the Coordinated Universal Time (UTC) [18]. The convention reported in the Standard for synchrophasor representation is shown in Fig. 2.3. On the left, the synchrophasor angle is 0 degrees when the maximum of (2.1) occurs at the UTC second rollover, on the right the synchrophasor angle is –90 degrees when the positive zero crossing occurs at the UTC second rollover.

In steady-state conditions the waveform frequency, amplitude and phase parameters can be considered as constant during the whole observation interval, while in a more realistic scenario they are affected by both amplitude and phase variations caused by power oscillations and other disturbances. So, in order to analyze the behavior of a power system under both steady-state and dynamic conditions, a generalization of the electrical waveform model in (2.1) is

$$x(t) = A[1 + \varepsilon_a(t)] \cdot \cos[2\pi f_0(1 + \delta)t + \varepsilon_p(t) + \phi] + \eta(t) \tag{2.3}$$

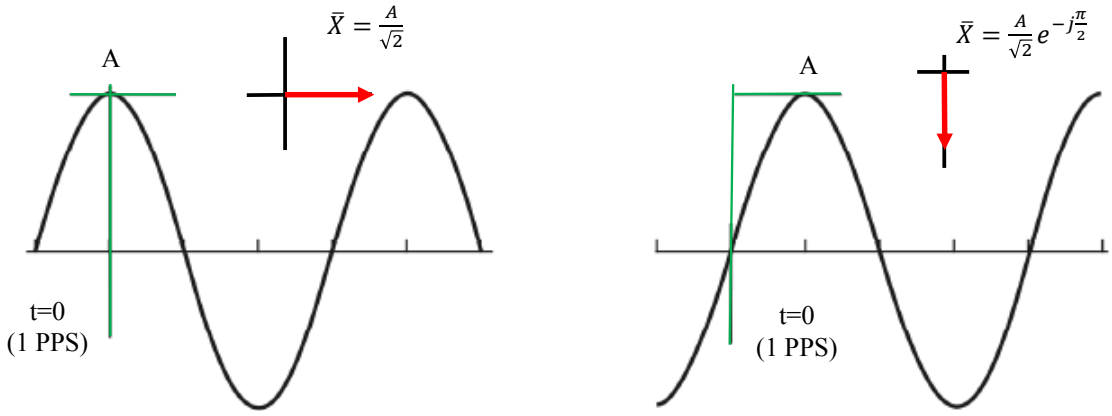

Figure 2.3: Convention for synchrophasor representation [18].

where A, f_0 and ϕ have the same meaning as in (2.1), $2\pi\delta f_0 t$ is the accumulated phase shift due to the static fractional off-nominal frequency offset δ, $\varepsilon_a(t)$ describes the time-varying amplitude fluctuations, $\varepsilon_p(t)$ includes possible phase fluctuations and $\eta(t)$ generally includes possible narrowband components (e.g. harmonics and additive wideband noise).

Since both amplitude and phase in (2.3) change as a function of time, the synchrophasor at the UTC reference time t_r is defined as

$$\bar{X}_r = \bar{X}(t_r) = \frac{A(t_r)}{\sqrt{2}} e^{j\varphi(t_r)} = \frac{A}{\sqrt{2}}[1 + \varepsilon_a(t_r)] \cdot e^{j[2\pi f_0(1+\delta)t_r + \varepsilon_p(t_r) + \phi]} \tag{2.4}$$

Frequency and rate of change of frequency estimation

A last generation PMU is able to measure not only the synchrophasor, but also the waveform frequency and the rate of change frequency estimation (ROCOF). Starting from equation (2.3), if $\varepsilon_a(\cdot)$ and $\eta(\cdot)$ are negligible, the sinusoidal signal can be rewritten as

$$x(t) = A\cos[\varphi(t)] \tag{2.5}$$

where $\varphi(t) = 2\pi f_0(1+\delta)t + \varepsilon_p(t) + \phi$. Thus frequency of signal $x(t)$ in (2.5) at time t_r is defined by

$$f_r = f(t_r) = \frac{1}{2\pi}\frac{d\varphi(t_r)}{dt} = f_0 + f_0\delta + \frac{1}{2\pi}\frac{d\varepsilon_p(t_r)}{dt} = f_0 + \Delta f(t_r) \tag{2.6}$$

where $\Delta f(t_r)$ is the instantaneous deviation frequency from the nominal value. Finally, the corresponding ROCOF is defined as follow

$$ROCOF_r = ROCOF(t_r) = \frac{df(t_r)}{dt} = \frac{1}{2\pi}\frac{d^2\varphi(t_r)}{dt^2} = \frac{d\Delta f(t_r)}{dt} \tag{2.7}$$

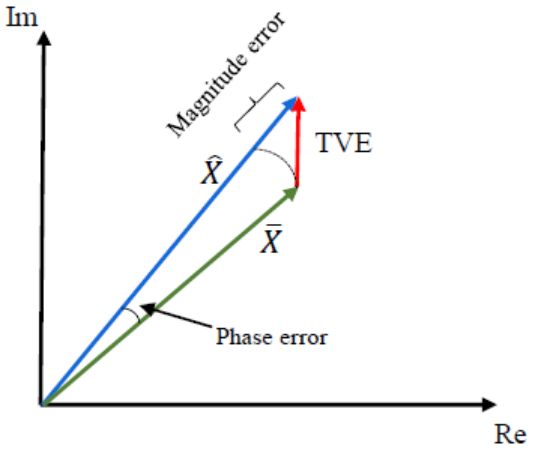

Figure 2.4: Graphical representation of TVE definition.

2.2.2 Measurement evaluation

Total Vector Error

The estimation accuracy of the synchrophasor measured by PMU is in the Standard typically expressed in terms of *Total Vector Error* (TVE). Indeed, TVE combines the effect of magnitude errors, phase errors and synchronization uncertainty. If we denote the estimated phasor as $\hat{\bar{X}}$ and the actual phasor value as $\bar{X}$, the TVE can be defined as

$$TVE_r = \frac{|\hat{\bar{X}}_r - \bar{X}_r|}{|\bar{X}_r|} \tag{2.8}$$

where the subscript r indicates that both the estimated and the actual value of the phasor are computed at the reference time t_r.

Frequency and ROCOF measurement error

In the last version of the Standard the frequency measurement error and the ROCOF measurement error are given by the difference between the actual values and the estimated values. They are defined as

$$FE_r = |f_r - \hat{f}_r| = |\Delta f_r - \Delta \hat{f}_r| \tag{2.9}$$

$$RFE_r = \left| \frac{df_r}{dt} - \frac{d\hat{f}_r}{dt} \right| \tag{2.10}$$

where the subscript r indicates that both the estimated and the actual value of the phasor are computed at the reference time t_r.

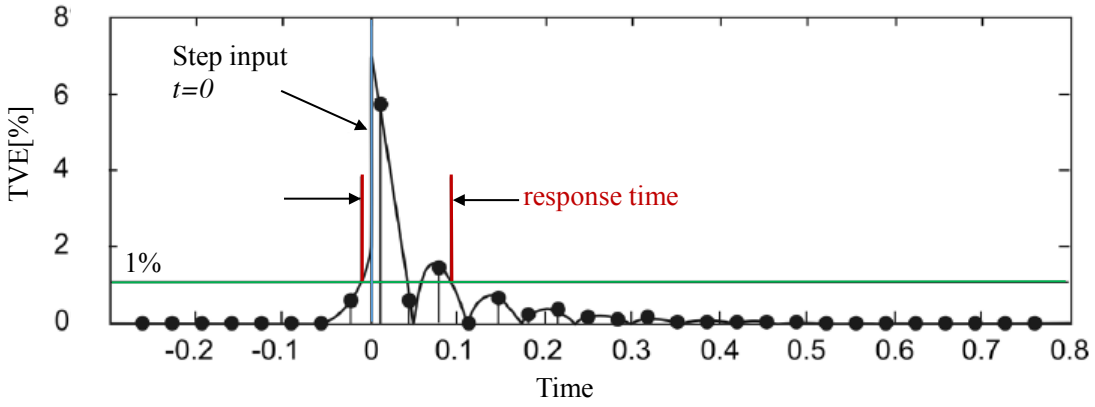

Figure 2.5: Example of amplitude step change over the time [18].

Response time and delay time

In order to evaluate the performance of an algorithm when sudden amplitude or phase change occurs, the Standard suggests to evaluate both the response time and the delay time. Especially the response time will be used in the following. However both definitions as they are reported in the Standard are recalled.
The measurement response time "*is the time to transition between two steady-state measurements before and after a step change is applied to the input. It shall be determined as the difference between the time that the measurement leaves a specified accuracy limit and the time it reenters and stays within that limit when a step change is applied to the PMU input.[...] Accuracy limits are the TVE, FE, and RFE values for the phasor, frequency, and ROCOF measurements, respectively*"[18]. In the case of TVE (that is the only parameter considered in next sections) the limit specified by the Standard is set equal to 1%. In Fig. 2.5 an example of TVE response time resulting from an amplitude step is shown.
The delay time is defined as "*the time when the stepped parameter achieves a value that is halfway between the starting and ending steady-state values*"[18].

2.3 Reference signal processing models

Since the PMUs can be made by different manufactures there is no indication in the Standard on the preferred estimation algorithm. Annex C of IEEE Std C37.118.1-2011 describes a reference signal processing model used to verify the Standard requirements. However the following disclaimer is also reported in the Standard: "*It is given for information purpose only, and does not imply being the only (or recommended) method for estimation synchrophasor*"[18]. Basically, the phasor estimation model relies on frequency

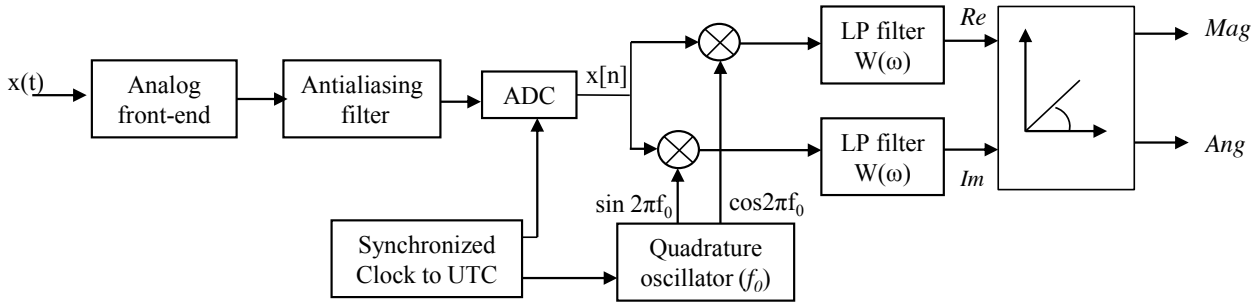

Figure 2.6: Block diagram of the synchrophasor estimation model suggested in the Standard IEEE C37.118.1-2011.

down-conversion and digital low-pass filtering of the in-phase and quadrature components of voltage and current waveforms. Two examples of low-pass filters having quite different performances in terms of latency and accuracy are also reported in the same annex: one for protection-oriented applications (*P-class* reference model) and the other when high measurement accuracy is required (*M-class* reference model). Starting from (2.3), if the phase fluctuations $\varepsilon_p(t)$ are negligible, but $\delta \neq 0$, then phasor (2.4) rotates at a constant rate δf_0. The block diagram of the basic synchrophasor estimation model described in Annex C of the Standard is shown in Fig. 2.6 [18]. The expression of the estimator is

$$\hat{\tilde{X}}_r = \begin{cases} \frac{\sqrt{2}}{W(0)} \cdot \sum_{n=-\frac{N-1}{2}}^{\frac{N-1}{2}} w[n]x[r+n] \cdot e^{-j\frac{2\pi}{M}(r+n)} & N \text{ odd} \\ \frac{\sqrt{2}}{W(0)} \cdot \sum_{n=-\frac{N}{2}}^{\frac{N}{2}} w[n]x[r+n] \cdot e^{-j\frac{2\pi}{M}(r+n)} & N \text{ even} \end{cases} \tag{2.11}$$

where:

- $x[\cdot]$ is the digitized input waveform sampled at a rate f_s by the front-end analog-to-digital converter (ADC);
- N is the number of impulse response coefficients of the chosen filter;
- $M = f_s/f_0$ represents the number of samples in one nominal waveform cycle. Accordingly, $2\pi/M$ is the angular frequency of the two quadrature digital sine-waves that are mixed with the input signal;
- $w[\cdot]$ is the impulse response of the adopted low-pass Finite Impulse Response filter;
- $W(\nu)$ is the frequency response of the filter, $\nu = f/f_s$ is the normalized digital frequency and $W(0)$ is the filter DC gain.

Estimator (2.11) returns the synchrophasor value referred to the observation interval centered at time t_r. Such a timestamp coincides with the sampling instant r/f_s, when N

is odd, whereas it lies between two subsequent samples (i.e., at time $(r-1/2)/f_s$), when N is even. As a consequence, while $W(\nu)$ is generally designed to provide a linear phase response, in (2.11) no phase delay is introduced by the filter (i.e. its phase response is zero). Notice that if we refer to $C = N/M$ as the number of nominal waveform cycles in N samples, (2.11) can be equivalently regarded as the $C-th$ sample of the windowed Discrete-time Fourier Transform of the sequence $x[\cdot]$ centered at time t_r. Therefore, the estimation approach described in [18] and the windowed DFT-based phasor estimators basically coincide, since the adopted sliding window simply acts as a filter [19].

2.3.1 P-Class filter model

The Annex C suggests a fixed-length two-cycle triangular FIR filter, with an odd number of samples, regardless of PMU reporting rates. The filter coefficients $w[n]$ are:

$$w[n] = \left(1 - \frac{2}{N+2}|n|\right) \tag{2.12}$$

where $n = -N/2, .., N/2$ and N is the filter order. The *P-class* filter works well at the nominal frequency when the observation interval matches exactly the period of the collected sine-wave. However in presence of off-nominal frequency deviations, a magnitude correction applied to the final phasor is required [18].

2.3.2 M-Class filter model for phasor

The *M-class* requires that the filter is able to attenuate significantly the signals above the Nyquist frequency for a given reporting rate. This filter provides more accurate results in the presence of noise and interfering signals, but with longer reporting delays. In the amendment to the Standard the filter mask specifications are shown in Fig. 2.7. The window coefficients can be computed with

$$w[n] = \frac{sin\left(2\pi \times \frac{2F_{fr}}{F_{samp}} \times n\right)}{2\pi \times \frac{2F_{fr}}{F_{samp}} \times n} h[n] \tag{2.13}$$

where $n = -N/2, ..., N/2$, N is the filter order, F_{fr} is the low-pass filter reference frequency (which depend on the reporting rate), F_{samp} is the sampling frequency and $h(n)$ is the Hamming window sequence.

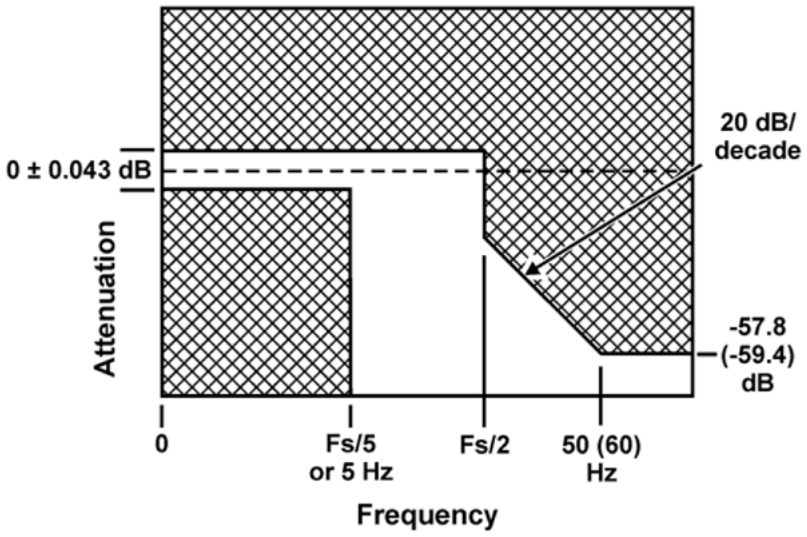

Figure 2.7: Reference algorithm filter frequency response mask specification for M class [18].

2.4 Proposed guidelines for filter-based synchrophasor estimation

As shown in paragraph 2.3.1 and 2.3.2, the Standard reports two examples of low-pass filters with different performances in terms of latency and accuracy. However, no clear filter design criteria are provided. In [20] and [21] the authors describe and analyze the performance of two orthogonal filters with time-frequency characteristics that are particularly suitable for fault location and measurement. In [22] a raised-cosine filter with a negligible phase distortion is described to halve the phasor estimation delay. In [23] and [24] two filters for *P-class* and *M-class* phasor estimation, respectively, are proposed to improve the performance of the basic model reported in Annex C of the Standard.

In this section, the same model is used as a starting point to identify optimal filter design criteria. Some simulation results support the proposed analysis.

2.4.1 Filter design criteria

According to (2.3), an electrical waveform in dynamic conditions can be regarded as an amplitude and phase modulated signal around a carrier of frequency $(1 + \delta) \cdot f_0$. If we suppose, for the sake of simplicity, that the modulating signals are two sine waves, $\varepsilon_a(t)$ and $\varepsilon_p(t)$ can be expressed as

$$\varepsilon_a(t) = k_a \cos[2\pi\delta_a f_0 t + \alpha_a] \tag{2.14}$$

and

$$\varepsilon_p(t) = k_p \cos[2\pi\delta_p f_0 t + \alpha_p] \tag{2.15}$$

where k_a (with $k_a \leq k_{a_M}$) is the amplitude modulation index, $\delta_a = f_a/f_0$ is the corresponding fractional frequency, k_p (with $k_p \leq k_{p_M}$) is the amplitude (expressed in radians) of the phase modulation signal and $\delta_p = f_p/f_0$ is the fractional modulation frequency. Under this assumption, it can be easily proved that the spectrum of (2.3) consists of an infinite series of monochromatic terms located at frequencies $[h\cdot(1+\delta)+ m\cdot\delta_p+l\cdot\delta_a]\cdot f_0$, for $h \leq 1$, and $l = -1, 0, 1$ [25]. This is due to the fact each tone resulting from phase modulation is in turn modulated also in amplitude, thus generating three spectral components at frequencies $(m \cdot \delta_p + l\cdot\delta_a)\cdot f_0$. The two side terms (i.e., shifted by $\pm\delta_a\cdot f_0$ with respect to $m \cdot \delta_p\cdot f_0$) are proportional to k_a. Moreover, the amplitude of each triple of spectral components is proportional to $J_m(k_p)$, i.e. the first-kind Bessel function of order m computed at k_p. Since the values of $|J_m(k_p)|$, for a given k_p, decrease monotonically as a function of $|m|$, the effective bandwidth of (2.3) containing 98% of the signal power around the carrier is $2 \cdot \beta \cdot f_0$, with $\beta = (k_p + 1)\delta_p + \delta_a$ [25]. Notice that, in accordance with (2.4), $\varepsilon_a(t)$ and $\varepsilon_p(t)$ are intrinsically part of the phasor to be estimated, whereas harmonics in (2.3) represent a disturbance and, consequently, must be suitably filtered to improve synchrophasor estimation. By mixing the digitized input sequence with two quadrature sine-waves of nominal frequency f_0 (or equivalently, of normalized frequency $1/M$), the fundamental component as well as the modulating terms of (2.3) are down-converted to the baseband, around frequency $\delta \cdot f_0$. Thus, if the static fractional frequency offset δ lies in the interval $[-\delta_M, \delta_M]$ (where δ_M represents the maximum value of the frequency measurement uncertainty assured by the considered PMU), the one-sided normalized filter bandwidth that must be used to preserve both static and dynamic phasor contributions is:

$$BW_p = \frac{(\delta_p + \beta_M) \cdot f_0}{f_s} = \frac{\delta_M + (k_{p_M} + 1) \cdot \delta_{p_M} + \delta_{a_M}}{M}, \tag{2.16}$$

where β_M, δ_{a_M} and δ_{p_M} denote the maximum allowed values of β, δ_a and δ_p, respectively. Such values can be hardly known a priori. However, for filter design purposes, they can be set in compliance with the requirements of some standard document such as the IEEE C37.118.1-2011 and the amendment IEEE C37.118.1a-2014. It is worth noticing that β_M/M is the bandwidth increment needed to track fast phasor fluctuations.

Fig. 2.8 provides a qualitative overview of the main features of the low-pass filter to be used for phasor estimation after signal down-conversion. Parameters r_1 and r_2 represent the maximum ripple amplitudes in the filter pass-band. In general, the flatness in-band requirements can be relaxed in the frequency interval $[\pm\delta_M/M, \pm(\delta_M + \beta_M)/M]$ (i.e. $r_2 > r_1$), because phase and amplitude fluctuations are expected to be quite small (e.g., in the order of 0.1 rad and 10% of phasor nominal amplitude, respectively). Observe that

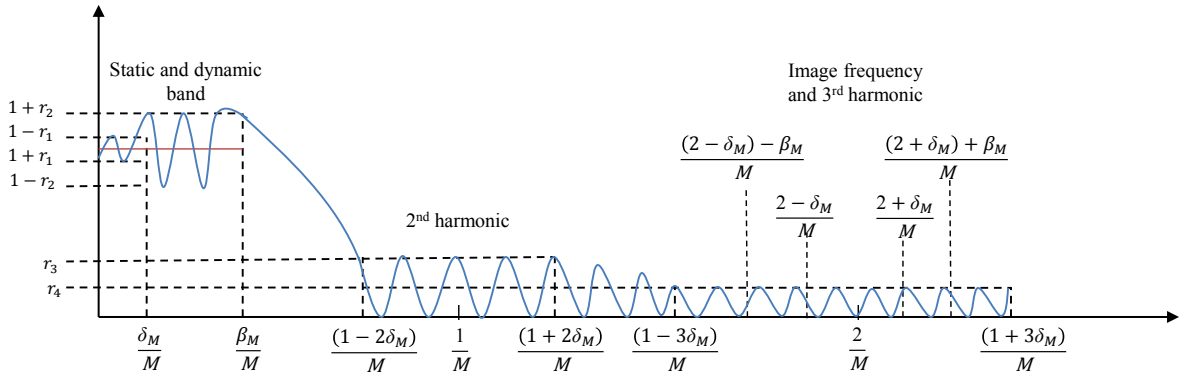

Figure 2.8: Qualitative representation of the filter design requirements in the frequency domain, including static and dynamic in-band flatness specifications, second-order and third-order harmonic attenuation and image tone cancellation.

the transition band of the filter must not exceed $(1–2\delta_M)/M$. This value corresponds to the lower end of the frequency interval $[(1–2\delta_M)/M, (1+2\delta_M)/M]$, where the second-order signal harmonic lies as a result of signal down-conversion.

In the following, we will refer to r_3 as the maximum amplitude of the filter frequency response in the band $[(1–2\delta_M)/M, (1+2\delta_M)/M]$. A similar attenuation affects the residual DC offset of the acquired signal as well, which after down-conversion is located at normalized frequency $–1/M$. The frequency band around $2/M$ deserves some special attention, because it includes two different contributions. First of all, the band $[(2–3\delta_M)/M, (2+3\delta_M)/M]$ contains the down-converted third-order harmonic of the collected signal. In addition, $(2+\delta)/M$ represents the normalized image frequency after down-conversion. This means that the band $[(2-\delta_M-\beta_M)/M, (2+\delta_M+\beta_M)/M]$ has exactly the same spectral content as the band $[(-\delta_M-\beta_M)/M, (\delta_M+\beta_M)/M]$. Thus, the magnitude of the filter frequency response in the band $[(2–\delta_M–\beta_M)/M, (2+\delta_M+\beta_M)/M]$ must be attenuated by a factor $r_4 \ll r_3$, in order to make the joint effect of the image component and the third-order harmonic negligible on estimation results. worth noticing that amplitude of the harmonic is generally at most one order of magnitude smaller than the fundamental. Therefore, if the filter magnitude for $\nu \geq (2+\delta_M+\beta_M)/M$ is smaller than r_4, the influence of higher-order harmonics on phasor estimation results becomes negligible. As known, the main performance parameter describing the accuracy of phasor measurement is the Total Vector Error (TVE) [18]. In particular, if (2.11) is applied to (2.3) to estimate the dynamic phasor described by (2.4), the following expression holds,

i.e.

$$TVE = \frac{\left|\hat{\bar{X}}_r - \bar{X}_r\right|}{\left|\bar{X}_r\right|} = \frac{\left|\hat{\bar{X}}_{b,r} + \hat{\bar{X}}_{i,r} + \sum_{h=2}^{H} \hat{\bar{X}}_{h,r} - \bar{X}_r\right|}{\left|\bar{X}_r\right|} \leqslant \frac{\left|\hat{\bar{X}}_{b,r} - \bar{X}_r\right|}{\left|\bar{X}_r\right|} + \frac{\left|\hat{\bar{X}}_{i,r}\right|}{\left|\bar{X}_r\right|} + \sum_{h=2}^{H} \frac{\left|\hat{\bar{X}}_{h,r}\right|}{\left|\bar{X}_r\right|}, \tag{2.17}$$

where $\hat{\bar{X}}_{b,r}$ is the baseband waveform component of the estimated phasor (namely the component of interest of the input signal), $\hat{\bar{X}}_{i,r}$ is the error contribution caused by the infiltration of the image component and $\hat{\bar{X}}_{h,r}$, for $h = 1, \cdots, H$ are the error terms due to imperfect harmonics filtering. If the phase modulation index is small enough (namely if $k_p \ll 1$, as it is typically expected in practice), then $J_0(k_p) \approx 1$, $|J_{-1}(k_p)| = |J_1(k_p)| < 0.1$ and $|J_m(k_p)| \approx 0$, for $m > 1$. Therefore, after a few algebraic steps it can be shown that the following inequality holds, i.e.

$$\frac{|\ \hat{\bar{X}}_{b,r} - \bar{X}_r\ |}{|\ \bar{X}_r\ |} < r_1 + |\ r_2 - r_1\ | \cdot \frac{\left[\frac{k_{a_M}}{2} + \frac{k_{a_M}+1}{10}\right]}{(1 - k_{a_M})}. \tag{2.18}$$

As far as the image and harmonic contributions are concerned, it is straightforward to show that

$$\frac{\left|\hat{\bar{X}}_{i,r}\right|}{\left|\bar{X}_r\right|} + \sum_{h=2}^{H} \frac{\left|\hat{\bar{X}}_{h,r}\right|}{\left|\bar{X}_r\right|} \left|\bar{X}_r\right| \leqslant r_4 + \frac{r_3 X_2 + \sum_{h=3}^{H} r_4 X_h}{X(1 - k_{a_M})}. \tag{2.19}$$

If TVE_{max} represents the maximum tolerable TVE value, the following general design conditions must be fulfilled:

- $1 - r_1 \leq |W(\nu)| \leq 1 + r_1$ with $r_1 \leq F_1 \cdot TVE_{max}$ for $\nu \in \left[0, \frac{\delta_M}{M}\right]$;
- $1 - r_2 \leq |W(\nu)| \leq 1 + r_2$ with $r_2 \leq F_2 \cdot TVE_{max}$ for $\nu \in \left[\frac{\delta_M}{M}, \frac{\delta_M + \beta_M}{M}\right]$;
- $|W(\nu)| \leq r_3$ with $r_3 \leq F_3 \cdot TVE_{max}$ for $\nu \in \left[\frac{1 - 2\delta_M}{M}, \frac{2 - \delta_M - \beta_M}{M}\right]$;
- $|W(\nu)| \leq r_4$ with $r_4 \leq F_4 \cdot TVE_{max}$ for $\nu \in \left[\frac{2 - \delta_M - \beta_M}{M}, +\infty\right]$;
- $F_1 + |F_2 - F_1| \cdot \frac{\left[\frac{k_{a_M}}{2} + \frac{k_{a_M}+1}{10}\right]}{1 - k_a} + F_4 + \frac{F_3 X_2 + \sum_{h=3}^{H} F_4 X_h}{X(1 - k_{a_M})} \leq 1;$ (2.20)

where F_1, F_2, F_3 and F_4 are adimensional factors that can be used to adjust filter pass-band and stop-band magnitude, so as to assure that TVE values are smaller than or equal to TVE_{max} both in static and dynamic conditions. Evidently, no unique criteria exist to select the values of fractions F_1, F_2, F_3 and F_4.

However, a few rules of thumb can be followed in order to make filter design simpler. For instance, F_2 can be up to one order of magnitude larger than F_1, since the value of k_{a_M} in the second term of design conditions above is about 0.1 [18]. This helps relaxing the flatness filter requirements in the pass-band. The impact of harmonic distortion depends on the relative amplitude of each harmonic with respect to the fundamental tone. According to the Standard [18], the relative amplitude of each harmonic till the $50th$ (i.e. $A_h = X_h/X$ for $h = 2, \cdots, H$, with $H = 50$ [18]) can be so large as 1% or 10% of the fundamental tone for *P-class* and *M-class*, respectively. As known, the second-order harmonic is the most critical, but it can be hardly removed due to the narrow transition band requirements of the filter. Thus, relaxing r_3 is essential for filter design feasibility over reasonably short intervals. Therefore, since $\frac{1}{(1-k_a)} \approx 1+k_{a_M}$ the relative contribution of the second-order harmonic to TVE becomes comparable to F_1 if $F_3 \approx \frac{F_1}{A_2\left(1+k_{a_M}\right)}$. Similarly, the overall joint TVE contribution due to image infiltration and higher-order harmonics may become comparable to F_1 when $F_4 \approx \frac{F_1}{(H-2)(1+k_{a_M})\underset{h=1,\cdots,H}{max}(A_h)+1}$. Notice that if the *P-class* specifications are good enough for the intended application, the TVE is generally dominated by image infiltration. In the case of *M-class* requirements instead, harmonic distortion is typically the main source of estimation uncertainty.

2.4.2 Simulation Results

In order to confirm the validity of the design criteria described in Section 2.4.1, two examples of filters have been proposed. Such filters do not result from any specific optimization procedure. Indeed, they have been obtained using known filter design techniques iteratively, while checking if condition (2.20) is satisfied a posteriori, but the globally compliance with the Standard is not guaranteed. All simulations have been performed assuming that $f_s = 6.4$ kHz and $M = 128$.

Example 1: Two-cycle filter

The accuracy of three two-cycle FIR filters have been compared, i.e.

- a 255-order filter with a triangular impulse response similar to the one suggested in the Annex C of the Standard IEEE C37.118.1-2011 [18];
- a filter minimizing the effect of phasor image infiltration [19];

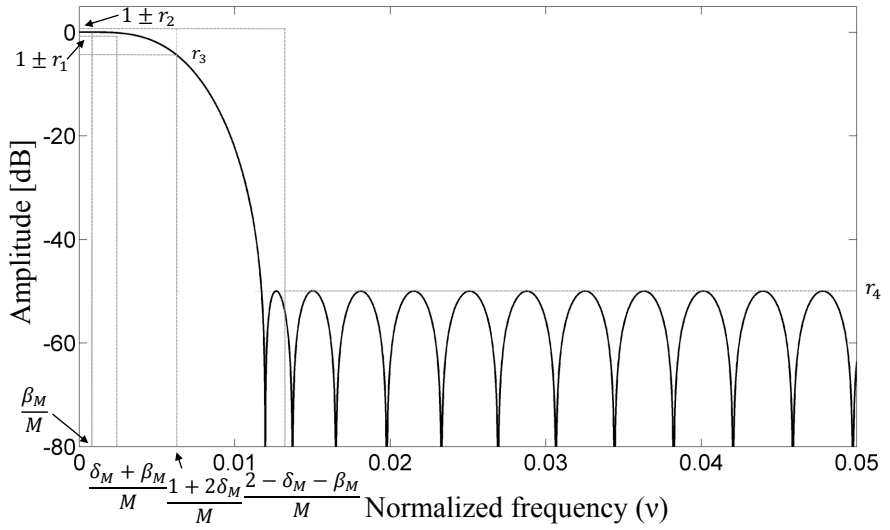

Figure 2.9: Frequency response magnitude of an equiripple FIR filter potentially compliant with the *P-class* requirements specified in the Standard IEEE C37.118.1-2011.

- an equiripple filter resulting from the Parks-McClellan algorithm and based on the general criteria described in Section 2.4.1 with $\delta_M = 0.1$, $\beta_M = 0.21$, $TVE_{max} \approx 1\%$, $F_1 = 0.8$, $F_2 = 8$,$F_3 = 60.7$ and $F_4 = 0.32$.

A common feature of all the considered filters is that their impulse response is about two nominal waveform cycles long. The frequency response magnitude of the designed FIR filter is shown in Fig. 2.9. The envelopes of the TVE curves resulting from 300 simulation runs (each one corresponding to a different set of random initial phases of the sine-waves in (2.3) and (2.4)) are shown in Fig. 2.10(a)- 2.10(b) as a function of the off-nominal frequency offset δ, with $|\delta| \leq \delta_M$. All parameter values have been set in accordance with the worst-case *P-class* static and dynamic testing conditions specified in the Standard [18]. In Fig. 2.10(a) no fluctuations nor harmonics disturbances are considered, whereas the curves in Fig. 2.10(b) result from the joint effect of worst-case amplitude modulation (with $k_a = 0.1$ and $\delta_a = 0.1$), phase modulation (with $k_p = 0.1$ and $\delta_p = 0.1$) and 50 harmonics, each one with a magnitude equal to 1% of the fundamental tone. However, while according to the Standard, one harmonic at a time should be added to the signal, in Fig. 2.10(b) all harmonics are added together, which is a worse and more realistic scenario. For static *P-class* compliance, TVE cannot exceed 1% for $|\delta| \leq 4\%$ even under the effect of harmonic distortion. This limit is extended to 3% when the effect of amplitude and phase modulations is taken into account. Notice that even in the presence of worst-case static and dynamic contributions, the TVE_{max} constraint is met. Quite interestingly, the maximum TVE values associated with the designed filter around the

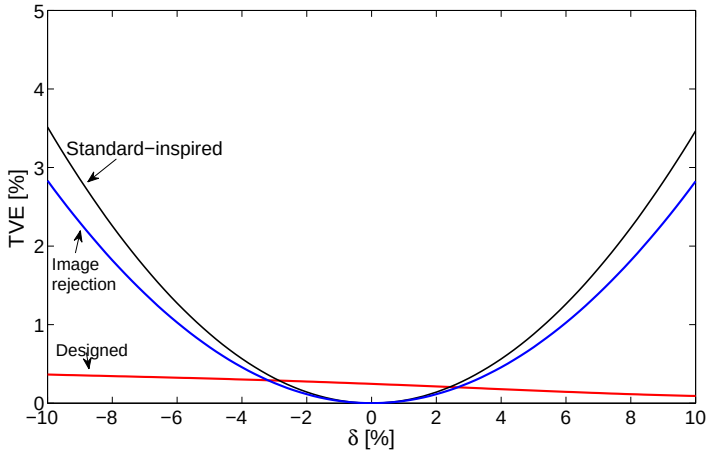

(a)

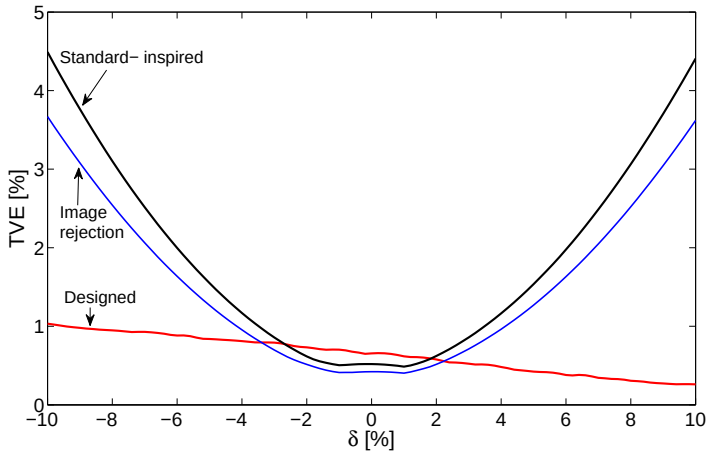

(b)

Figure 2.10: Maximum TVE curves for three different two-cycle filters (i.e., using a triangular impulse response [18], minimizing the image tone infiltration [19], and using the criteria described in this section): (a) off-nominal frequency offset δ only; (b) joint effect of off-nominal frequency offsets, amplitude modulation, phase modulation and 50 harmonics with amplitude equal to 1% of the fundamental.

nominal frequency (i.e., for $\delta \approx 0$) are slightly higher than the corresponding values of the other two solutions, because the DC gain of the proposed filter is slightly larger than 1. Nevertheless, its global behavior is better, because the chosen filter tends to minimize the joint effect of different contributions over the whole spectrum. Observe also that the TVE pattern of the designed filter is asymmetric because its frequency response magnitude in the band $[(1–2\delta_M)/M, (1 + 2\delta_M)/M]$ decreases monotonically. As a consequence, the attenuation of the second-order harmonic between $(1–2\delta_M)/M$ and $(1 + 2\delta_M)/M$ grows

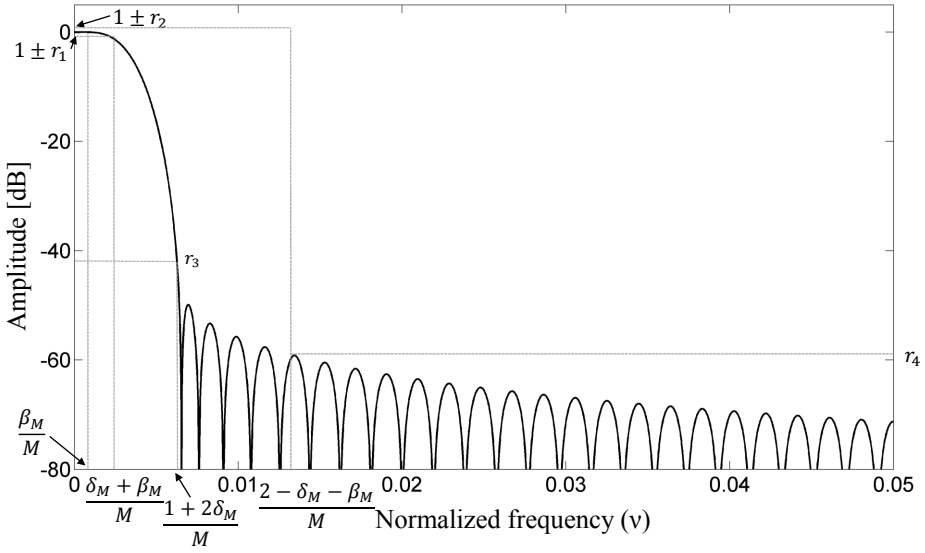

Figure 2.11: Frequency response magnitude of a least squares FIR filter compliant with the *M-class* requirements specified in the Standard IEEE C37.118.1-2011.

accordingly.

Example 2: Four-cycle filter

As explained in Section 2.4.1, *M-class* filter design requires tighter filtering specifications due to the presence of possible large harmonics. For this reason, filter impulse responses must be longer than in the *P-class* case. In the following, the performance of three four-cycle long filters are compared through simulations, i.e.

- a 512-order filter resulting from the product between a Hamming window and a truncated sinc sequence, as described in Annex C of Standard IEEE C37.118.1-2011 for a reporting rate of 50 fps [18];
- the four-cycle raised cosine filter (RCF) proposed in [26];
- a linear-phase FIR filter resulting from least-squares error minimization and based on the general criteria described in Section 2.4.1 with $\delta_M = 0.1$, $\beta_M = 0.21$, $TVE_{max} \approx 0.5\%$, $F_1 = 0.4$, $F_2 = 18$, $F_3 = 1.59$ and $F_4 = 0.22$.

The frequency response magnitude of the designed filter is shown in Fig. 2.11. The envelopes of the TVE patterns of all filters under the effect of off-nominal frequency offsets only, and worst-case amplitude modulation, phase modulation and harmonics are shown in Fig. 2.12(a) and 2.12(b), respectively. The simulation parameters are the same

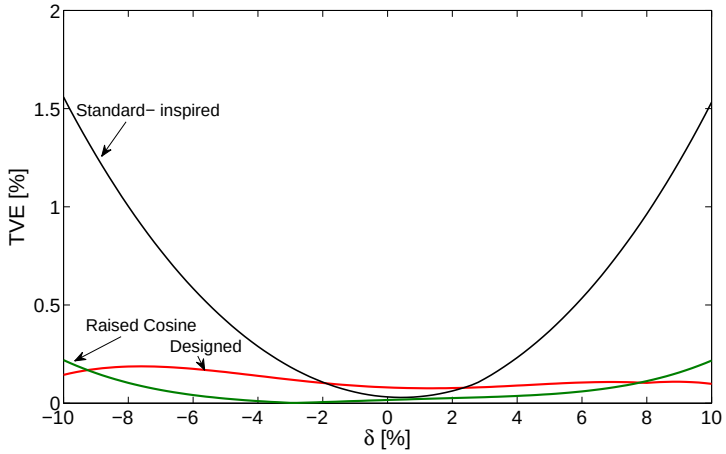

(a)

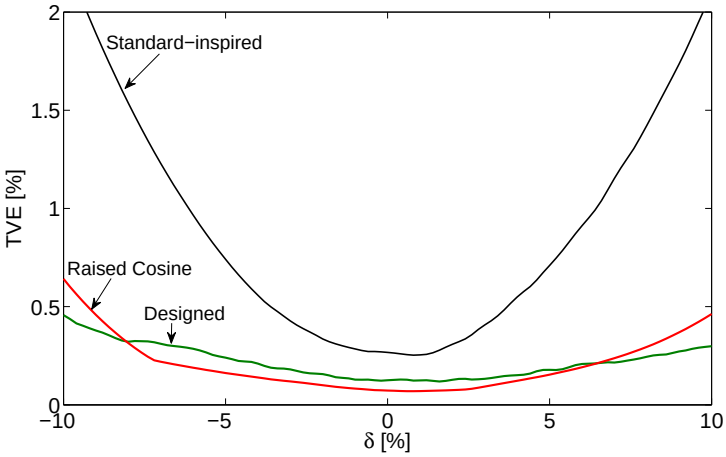

(b)

Figure 2.12: Maximum TVE curves of three different four-cycle filters (i.e., using a Hamming-windowed sinc sequence [18], a raised cosine [26], or the criteria described in this section): (a) off-nominal frequency offset δ only; (b) joint effect of off-nominal frequency offsets, amplitude modulation, phase modulation and 50 harmonics with amplitude equal to 10% of the fundamental.

as in the previous case, except for harmonics amplitude, which is now equal to 10% of the fundamental. Clearly, the performance of the filter based on the approach suggested in the Standard is quite disappointing, whereas the RCF exhibits superior accuracy around the nominal frequency (i.e., for $\delta \approx 0$). This is mainly due to its maximal flatness in the pass-band. Even if such a filter was not explicitly designed using the criteria described in Section 2.4.1, as a matter of fact, it meets them almost everywhere, with a small exception around frequencies $\pm(\delta_M + \beta_M)/M$, where the lower bound $1–r_2$ is violated. Observe that

the maximum TVE of the proposed filter instead is approximately constant and below 0.5%, as expected.

2.5 Conclusion

This chapter introduces the synchrophasor estimation problem. Starting from the description of a general PMU, the main quantities of interest are defined and some practical guidelines to design filters for synchrophasor estimation based on the architecture of Annex C of IEEE Std C37.118.1-2011 are proposed. Such criteria rely on:

i) a detailed analysis of the spectral characteristics of the power waveforms to be monitored in both static and dynamic conditions as they are defined with the Standard IEEE C37.118.1-2011;
ii) the impact of the main uncertainty contributions on the overall TVE.

In general, the tight transition band requirements make lowpass filter design challenging, especially when the observation interval is shorter than four waveform cycles. Some simulation results confirm the correctness of the proposed design methodology. However, to assure accurate and fast synchrophasor estimation, more sophisticated algorithms and techniques are needed.

Chapter 3

Synchrophasor Estimation Algorithms

In the recent years a multitude of synchrophasor estimators have been proposed in the literature. Some of them rely from the static phasor model; others rely are on a dynamic model. In this chapter, starting from a short literature review of the main synchrophasor measurement methods, an extended comparative analysis of three selected techniques is presented, while considering the well known one-cycle DFT estimator as a reference benchmark. The performance analysis is done under the steady-state and dynamic conditions specified in the IEEE Standard C37.118.1-2011.

3.1 Literature overview

The traditional synchrophasor measurements algorithms are based on the static phasor concept. One of the most widely used techniques implemented is the windowed Discrete Fourier Transform (DFT) shown in (2.11). It is simple, fast and exhibits good performance applied to data records with a possible different length corresponding to a half, one or multiple waveform cycles at the nominal frequency of 50 Hz or 60 Hz. The most used is the one-cycle DFT. However, the DFT returns very inaccurate results in the case of the significant off-nominal frequency offset. Performance can be greatly improved through suitable windows as in [19] or using the so-called interpolated-DFT (IpDFT) algorithm, which compensates the scalloping loss of the window spectrum by interpolating the DFT

Part of this chapter were published in

G. Barchi, D. Macii and D. Petri, "Synchrophasor Estimators Accuracy: A Comparative Analysis," *IEEE Trans. Instr. and Meas.*,vol.62, no.5, pp.963-973, May 2013.

G. Barchi, D. Macii, D. Belega and D. Petri, "Performance of synchrophasor estimators in transient conditions: A comparative analysis", *IEEE Trans. Instr. and Meas.*,vol.62, no.9, pp.2410-2418, Sept. 2013.

values around the fundamental waveform frequency [27].

Several variants of this basic method have been proposed in the last years. Among them, the half-cycle DFT-based techniques proved to be particularly effective to track sudden phasor changes during transients [28],[29], but they are also quite sensitive to noise, harmonics and out-of-band interferers.

Conversely, the two-cycle DFT solutions assure better accuracy in static conditions, but at the expense of a lower responsiveness when the waveform parameters change significantly within a single period. Alternative solutions based on sample value adjustment to compensate for the lack of the coherence in the presence of frequency offset have been proposed [30]. The classic DFT algorithms are fairly inaccurate also under dynamic or transient conditions [31], [32], [33]. So, in the last years various alternatives based on the Taylor's series expansion of the phasor have been proposed.

The temporal evolution of the phasor can be indeed tracked with good accuracy by estimating its first- and second-order derivative with respect to the time, e.g. through finite difference equations of two or three non-overlapped subsequent one-cycle DFTs [34]. Alternatively, the dynamic phasor and its derivatives can be estimated through least-square (LS) [35] or weighted least squares (WLS) optimization [36]. A similar approach is also used in the so-called Taylor-Fourier Transform (TFT), which in addition provides one-shot estimates of the derivatives of the complex envelops of the largest harmonics through a linear transform.

Although the basic performance of different synchrophasor estimators has been analyzed in the literature [37, 38], an extensive characterization with respect to the requirements of the Standard IEEE C37.118.1-2011 is not available yet.

3.2 Analyzed Synchrophasor Estimators

In the previous chapter a generic electrical waveform $x(t)$ is defined in (2.3), where its related synchrophasor at the UTC reference time t_r is expressed by (2.4). Considering $\bar{X}(t)$ as the phasor at a generic time $t = t_r + \Delta t$ (with Δt small enough), the phasor itself can be described with a good approximation by its Taylor's series expansion truncated to the Kth order term, with K arbitrary, i.e.

$$\bar{X}(t) \cong \bar{X}_r + \bar{X}'_r \Delta t + \frac{\bar{X}''_r}{2!}\Delta t^2 + ... + \frac{\bar{X}_r^K}{K!}\Delta t^K \tag{3.1}$$

where $\bar{X}_r^K$, for $k = 1, ..., K$ is the kth-order derivative of (2.4) computed at the reference time.

Assume that a PMU collects N samples of $x(t)$ in an observation interval synchronized to the UTC at a sampling rate $f_s = M \cdot f_0$. A basic approach to avoid unnecessary phase

estimation errors is to center each observation interval at the time in which the phasor has to be estimated. If an even number of samples N is considered, the interval central point lies exactly between the two central samples. This equivalently means that each sampling instant must be shifted by 1/2 sample with respect to the reference timestamp in order to assure centering. Conversely, if N is an odd number, the center of the observation interval just coincides with one of the available samples, and no time shift is required. The data record used to estimate the phasor at time t_r can be formalized using the following expression, i.e.

$$x_r[n] = A\left[1+\varepsilon_{a_r}\left(\frac{n+r+s}{f_s}\right)\right]\cdot\cos\left[\frac{2\pi}{M}(n+r+s)+\varepsilon_{p_r}\left(\frac{n+r+s}{f_s}\right)+\phi\right]+\eta[n] \tag{3.2}$$

where, $n=-(N-1)/2-s,\cdots,(N-1)/2-s$, $s=0$ or $1/2$ depending on whether N is an odd or an even number, respectively; and $\eta(n)$ includes both the harmonics of the fundamental component and the additive wideband noise. Observe that (3.2) holds for any value of r, i.e. not only for disjoint observation intervals, but also when they are just shifted by one sample at a time.

As described in section 3.1, various phasor estimators of (3.2) exist. The most common one is the basic DFT, here defined as:

$$\hat{\bar{X}}_r^{DFT} = \frac{\sqrt{2}}{N}\sum_{n=\frac{-N-1}{2}-s}^{\frac{N-1}{2}-s} x_r[n]e^{-j\frac{2\pi}{M}(n+s)}. \tag{3.3}$$

If the duration of the observation intervals in which synchrophasors are estimated coincides with a single, nominal waveform cycle, then $N=M$. It is interesting to observe that the complexity of (3.3) is $O(N)$, since just one spectral sample (i.e. corresponding to the fundamental waveform component) must be computed. In particular, N complex quantities (i.e. $2N$ real numbers corresponding to the exponential terms in (3.3)) and N real-valued samples have to be stored into memory at the same time. Therefore, about $2N$ real-valued products and additions are required to return a single estimate. Observe that (3.3) can hardly track fast phasor variations, because it implicitly relies on a 0-order Taylor model, i.e. $K=0$ in (3.1).

If we assume $K=1$, a possible dynamic phasor estimator is [34]

$$\hat{\bar{X}}_r^{4PM} \approx \hat{\bar{X}}_r^{DFT} - j\frac{\hat{\bar{X}}_r^{DFT^*} - \hat{\bar{X}}_{r-1}^{DFT^*}}{2M\sin\left(\frac{2\pi}{M}\right)}, \tag{3.4}$$

where $\hat{\bar{X}}_r^{DFT}$ is given by (3.3) for $N=M$, $\hat{\bar{X}}_r^{DFT^*}$ is the complex conjugate of $\hat{\bar{X}}_r^{DFT}$ and $\hat{\bar{X}}_{r-1}^{DFT}$ is the DFT of the data record in the one-cycle observation interval centered at time t_{r-1}. This phasor estimator is sometimes referred to as 4-parameter (4PM) model, as it

relies on four real-valued parameters (i.e., the real and imaginary parts of the synchrophasors estimated in two consecutive and disjoint one-cycle observation intervals). In terms of memory and computational resources, the requirements of the 4PM phasor estimator are almost the same as those of the one-cycle DFT estimator, provided that the $\hat{\bar{X}}_{r-1}^{DFT}$ values are temporarily buffered. Of course the accuracy of (3.4) depends on how well this estimator is able to track phasor variations. However, in the following just the case of disjoint intervals will be analyzed, in accordance with the original algorithm definition [34].

If the Taylor's series expansion of the phasor includes also the second-order derivative with respect to time (namely the phasor's acceleration, for $K = 2$) and, again, $N = M$ samples are used to compute each DFT values, a more sophisticated phasor estimator is

$$\begin{aligned}\hat{\bar{X}}_r^{6PM} \approx \hat{\bar{X}}_r^{DFT} &- j\frac{\left(\frac{3}{2}\hat{\bar{X}}_r^{DFT^*} - 2\hat{\bar{X}}_{r-1}^{DFT^*} + \frac{1}{2}\hat{\bar{X}}_{r-2}^{DFT^*}\right)}{2M\sin\left(\frac{2\pi}{M}\right)} \\ &- \frac{\left(1-\frac{1}{M}\right)\left(\hat{\bar{X}}_r^{DFT} - 2\hat{\bar{X}}_{r-1}^{DFT} + \hat{\bar{X}}_{r-2}^{DFT}\right)}{24} \\ &- \frac{\cos\left(\frac{2\pi}{M}\right)\left(\hat{\bar{X}}_r^{DFT^*} - 2\hat{\bar{X}}_{r-1}^{DFT^*} + \hat{\bar{X}}_{r-2}^{DFT^*}\right)}{2M^2\cdot\sin^2\left(\frac{2\pi}{M}\right)}.\end{aligned} \tag{3.5}$$

This estimator is usually referred to 6-parameter (6PM) model, as it relies on 6 real values (i.e., the real and imaginary parts of the phasors estimated in three consecutive and disjoint one-cycle observation intervals). Evidently, also in this case the memory and computational resources of the 6PM algorithm are roughly the same as those of a one-cycle DFT phasor estimator, provided that the $\hat{\bar{X}}_{r-1}^{DFT}$ and $\hat{\bar{X}}_{r-2}^{DFT}$values are temporarily stored. Observe that both in (3.4) and (3.5) the first- and second-order phasor derivatives are estimated through finite difference expressions.

Alternatively, the phasor and its derivatives can be obtained from a least squares minimization of the error between (3.1) and the values resulting from a linear transform of the data sequence acquired in the rth observation interval. In particular, if $\mathbf{x_r}$ is the N-long column vector containing the samples of (3.2) and $\bar{\mathbf{X}}_{r_K} = \left[\bar{X}_{r_K}^*, \bar{X}_{r_{K-1}}^*, ..., \bar{X}_{r_0}^*, \bar{X}_{r_0}, ..., \bar{X}_{r_{K-1}}, X_{r_K}\right]^T$ is the column vector composed by coefficients $\bar{X}_{r_K} = \frac{\bar{X}_r^K}{k!f_s^k}$ and their complex counterparts $\bar{X}_{r_K}^*$, for $k = 0, ..., K$, the phasor estimates and the corresponding derivatives result from [39][36]

$$\hat{\bar{\mathbf{X}}}_{r_K} = 2\left(B_K^H W^H W B_K\right)^{-1} B_K^H W^H W \mathbf{x}_r, \tag{3.6}$$

where

$$W = \begin{bmatrix} w_1 & 0 & \cdots & 0 \\ 0 & w_2 & \cdots & 0 \\ \vdots & \vdots & \ddots & \vdots \\ 0 & 0 & \cdots & w_N \end{bmatrix} \tag{3.7}$$

is a diagonal matrix containing the coefficients of the window mitigating the spectral effect of rectangular windowing and

$$B_K = \begin{bmatrix} B_{K,1} & B_{K,3} \\ B_{K,2} & B_{K,4} \end{bmatrix} \tag{3.8}$$

is a Nx2$(K+1)$ complex matrix. The elements of the individual sub-matrices $B_{K,1}$, $B_{K,2}$, $B_{K,3}$ and $B_{K,4}$ are defined as follows [36]:

$$\begin{aligned}
(b_{k,1})_{lq} &= \left(l - \frac{N-1}{2}\right)^{K-q} e^{j\left(\frac{N-1}{2}-l\right)\frac{2\pi}{M}} \\
&\qquad\qquad l = 0, \cdots, \frac{N-1}{2} - s \text{ and } q = 0, \cdots, K \\
(b_{k,2})_{lq} &= (l-s)^{K-q} e^{-j(l-s)\frac{2\pi}{M}} \\
&\qquad\qquad l = 1, \cdots, \frac{N-1}{2} + s \text{ and } q = 0, \cdots, K \\
(b_{k,3})_{lq} &= \left(l - \frac{N-1}{2}\right)^{q} e^{-j\left(\frac{N-1}{2}-l\right)\frac{2\pi}{M}} \\
&\qquad\qquad l = 0, \cdots, \frac{N-1}{2} - s \text{ and } q = 0, \cdots, K \\
(b_{k,4})_{lq} &= (l-s)^{q} e^{-j(l-s)\frac{2\pi}{M}} \\
&\qquad\qquad l = 1, \cdots, \frac{N-1}{2} + s \text{ and } q = 0, \cdots, K.
\end{aligned} \tag{3.9}$$

It is worth noticing that even if all $K+1$ terms of model (3.1) are computed in one shot from (3.6), the phasor estimated in the center of the considered observation interval corresponds just to the zero-order element of the output vector, i.e. $\hat{\hat{X}}_r^{TWLS} = \hat{\hat{X}}_{r_0}$, where the acronym TWLS stands for Taylor Weighted Least Squares. The computational requirements of the TWLS phasor estimator strongly depend on how it is implemented. If we assume that the elements in (3.6) (which consists of constant complex numbers for given values of K, N, M and W) are pre-computed and statically stored into memory as a look-up table, (3.6) requires $4N \times (K+1) + N$ real values at a time, and about $4N \times (K+1)$ real products and additions to return a single estimate. In addition, if just the phasor estimate $\hat{\hat{X}}_{r_0}$ is required, the number of real-valued sums and products

is given by a single row-column product, which requires $2N$ operations. In conclusion, the computational complexity burden of the TWLS algorithm, if properly optimized, is similar to the complexity of a plain DFT phasor estimator.

3.3 Accuracy performance analysis

In this section several simulations results are reported to compare the performance of DFT, 4PM, 6PM and TWLS estimators under the effect of various steady-state and dynamic tests. Specifically, the following cases are considered:

A. effect of static off-nominal frequency offsets;
B. effect of amplitude and phase modulation;
C. effect of harmonics;
D. effect of wideband noise.

Generally, the accuracy of phasor estimators is expressed in terms of TVE, which is defined in (2.8). Since the TVE depends on both the chosen estimators and the actual phasor value at reference time t_r it will be expressed in the following as, TVE_r^m where the superscript $m \in$={DFT, 4PM, 6PM, TWLS} refers to the specific estimator considered.

3.3.1 Effect of static off-nominal frequency-offset

Assume that the rth data record (3.2) is affected by a static fractional frequency offset $\delta \neq 0$, so that the actual waveform fundamental frequency is $f = (1 + \delta) \cdot f_0$, and no significant amplitude or phase variations occur in the same observation interval. In terms of notation this equivalently means that in (3.2) $\eta[n] = 0$, $\varepsilon_{a_r} = 0$ and

$$\varepsilon_{p_r}[n] = \frac{2\pi\delta}{M}(n + r \cdot N) \qquad -\frac{N-1}{2} \leq n \leq \frac{N-1}{2} \tag{3.10}$$

for $r \in Z$. When a one-cycle DFT is used as a synchrophasor estimator, the maximum TVE values can be expressed by the following function of δ [19]:

$$\mathrm{TVE}_{max}^{DFT}(\delta) \cong \frac{\pi^2\delta^2}{6} + \left|\frac{\delta}{2+\delta}\right|. \tag{3.11}$$

Similarly, it is possible to show that the maximum TVE associated with (3.4) is approximately given by

$$\mathrm{TVE}_{max}^{4PM}(\delta) \cong \left(\frac{\pi^2}{6} - \frac{1}{4} + \frac{1}{4}\sqrt{1+4\pi^2}\right)\delta^2 \cong 3.0 \cdot \delta^2. \tag{3.12}$$

Proof of expression (3.12).

If (3.3) is used to estimate the phasor, the corresponding estimator can be equivalently expressed as [19]:

$$\hat{\bar{X}}_r^{DFT} = \bar{X}_r \cdot D_N(-\delta)\left[1 + e^{-j2\varphi_r}\frac{D_N(2+\delta)}{D_N(-\delta)}\right] \tag{3.13}$$

where

$$D_N(\delta) = \frac{1}{N}\cdot\frac{\sin(\pi\delta)}{\sin(\frac{\pi\delta}{N})} \tag{3.14}$$

is the normalized *Dirichlet kernel*. Moreover, for δ close to zero we have that

$$D_N(\delta) \cong \left(1 - \frac{\pi^2\delta^2}{6}\right), \qquad |\delta| \leq 10\% \tag{3.15}$$

and

$$\frac{D_{P\cdot M}(2+\delta)}{D_{P\cdot M}(-\delta)} = \frac{\sin(\frac{\pi\delta}{N})}{\sin\left(\frac{\pi(2+\delta)}{N}\right)} \cong \frac{\delta}{2+\delta} \cong \frac{\delta}{2}\left(1 - \frac{\delta}{2}\right), \qquad |\delta| \leq 10\% \tag{3.16}$$

which results from the Taylor's series expansions of (3.14) around $\delta = 0$, truncated to the first-order term. Accordingly, (3.13) can be approximately expressed as

$$\begin{aligned}\hat{\bar{X}}_r^{DFT} &\cong \bar{X}_r \cdot \left[1 - \frac{\pi^2\delta^2}{6} + e^{-j2\varphi_r}\frac{\delta}{2}\left(1-\frac{\delta}{2}\right)\cdot\left(1-\frac{\pi^2\delta^2}{6}\right)\right] \\ &\cong \bar{X}_r \cdot \left[1 - \frac{\pi^2\delta^2}{6} + e^{-j2\varphi_r}\frac{\delta}{2}\left(1-\frac{\delta}{2}\right)\right]\end{aligned} \tag{3.17}$$

If a one cycle observation interval is used the difference between the rth and the $(r-1)$th reference timestamps is equal to $1/f_0$ and the corresponding phase difference is $\varphi_r - \varphi_{r-1} = 2\pi\cdot(1+\delta)$. Therefore, the difference between subsequent non-overlapped DFT-based phasor estimates is given by

$$\begin{aligned}\hat{\bar{X}}_r^{DFT} - \hat{\bar{X}}_{r-1}^{DFT} &= \bar{X}_r \cdot \left[D_N(-\delta)(1-e^{-j2\pi\delta}) + e^{-j2\varphi_r}D_N(2+\delta)(1-e^{j2\pi\delta})\right] \\ &\cong \bar{X}_r \cdot \left[\left(1-\frac{\pi^2\delta^2}{6}\right)(j2\pi\delta + 2\pi^2\delta^2) + e^{-j2\varphi_r}\frac{\delta}{2}\left(1-\frac{\delta}{2}\right)(-j2\pi\delta + 2\pi^2\delta^2)\right] \\ &\cong \bar{X}_r \cdot j2\pi\delta\left[1 - j\pi\delta + e^{-j2\varphi_r}\frac{\delta}{2}\left(1-\frac{\delta}{2}\right)(-1-j\pi\delta)\right] \\ &\cong \bar{X}_r \cdot j2\pi\delta\left[1 - j\pi\delta - e^{-j2\varphi_r}\frac{\delta}{2}\right]\end{aligned} \tag{3.18}$$

where in (3.18) the polynomial terms in δ of order higher than one can be neglected. By replacing (3.17) and (3.18) into (3.4) (since we can assume that $M \gg 2\delta$), it follows that

the 4PM estimator can be expressed as

$$\begin{aligned}\hat{\bar{X}}_r^{4PM} &= \hat{\bar{X}}_r^{DFT} - j\frac{\left(\hat{\bar{X}}_r^{DFT^*} - \hat{\bar{X}}_{r-1}^{DFT^*}\right)}{2M \cdot \sin\left(\frac{2\pi}{M}\right)} \\ &\cong \hat{\bar{X}}_r^{DFT} - j\frac{\left(\hat{\bar{X}}_r^{DFT^*} - \hat{\bar{X}}_{r-1}^{DFT^*}\right)}{4\pi} \\ &\cong \bar{X}_r \cdot \left[1 - \left(\frac{\pi^2}{6} - \frac{1}{4}\right)\delta^2 - e^{-j2\varphi_r}\frac{\delta^2}{2}\left(\frac{1}{2} + j\pi\right)\right]. \end{aligned} \tag{3.19}$$

Thus, by applying (2.8) the corresponding TVE is

$$\mathrm{TVE}_r^{4PM} = \left|\left(\frac{\pi^2}{6} - \frac{1}{4}\right) + e^{-j2\varphi_r}\frac{1}{2}\left(\frac{1}{2} + j\pi\right)\right|\delta^2 \tag{3.20}$$

and (3.12) results simply from the maximum of (3.20). □

A polynomial approximation of the TVE expression of the 6PM estimator also holds and it is given by

$$\mathrm{TVE}_{max}^{6PM}(\delta) \cong 82 \cdot \delta^4 + 1.6 \cdot \delta^3 + 0.7 \cdot \delta^2 + 0.007 \cdot \delta. \tag{3.21}$$

Expression (3.21) results from a polynomial fitting of the worst-case values obtained by changing randomly the initial phase ϕ of waveform in the range $[0, 2\pi]$, for a fixed fractional off-nominal frequency offset (i.e. $\delta = 0\%$, $\pm 2\%$, $\pm 4\%$, $\pm 6\%$, $\pm 8\%$, $\pm 10\%$). Similar considerations hold for the TWLS estimator, whose maximum TVE curves are hard to find analytically, because they depend on the number of considered K derivative terms in the model and on the elements of the matrix W used in (3.6). Assuming that $K = 3$ and that a Kaiser window with $\beta = 8$ is used [36], the maximum TVE curve associated with $\hat{\bar{X}}_r^{TWLS}$ for $N = 4M + 1$ (i.e. when four-cycle long observation intervals are considered), is given by

$$\mathrm{TVE}_{max}^{6PM}(\delta) \cong 9.1 \cdot \delta^4 + 0.0004 \cdot \delta^3 + 0.001 \cdot \delta^2 - 0.000001 \cdot \delta. \tag{3.22}$$

In Fig. 3.1 the TVE curves based on (3.11)–(3.22) are plotted as a function of δ in the range [–10%, 10%], as specified in the Standard IEEE C37.118.1. This interval corresponds to the broadest frequency variation range over which the TVE must be kept below 1% to assure *M-class* compliance at the maximum reporting rate [18]. Multiple Monte Carlo simulations consisting of 2000 runs each and obtained with different seeds for $N \geq 64$ and different values of in ϕ_r in $[0, 2\pi]$ and δ in[–10%, 10%] confirm that expressions (3.11)-(3.22) are very accurate. Indeed, the maximum absolute value of the differences between (3.11)-(3.22) and the respective simulation results range between $1.0 \cdot 10^{-6}$ for TWLS to

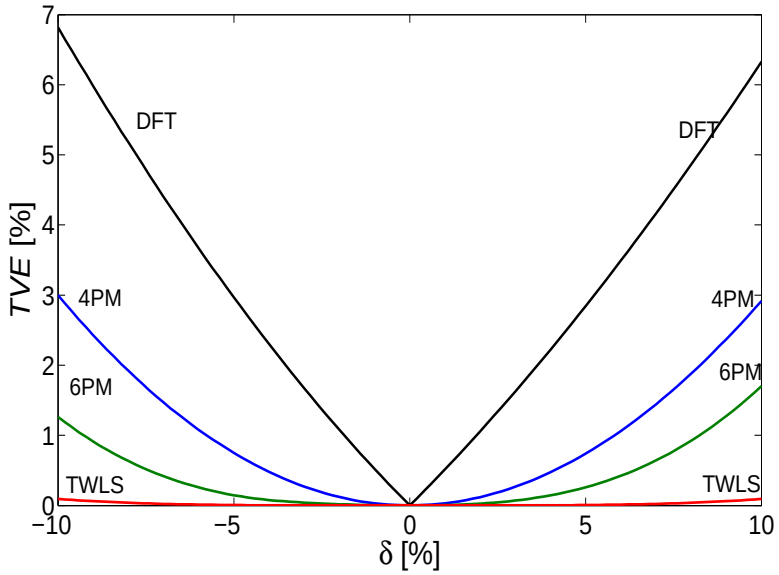

Figure 3.1: Maximum TVE values for different phasor estimators in steady-steate conditions as a function of the fractional frequency offset.

$2.0 \cdot 10^{-4}$ for 6PM. Observe that in Fig. 3.1 the accuracy of all the considered estimators degrades as the frequency offset increases.

However, the sensitivity of the one-cycle DFT, 4PM, 6PM and TWLS techniques to growing frequency offsets is clearly smaller and smaller, till becoming almost negligible (i.e. close to 0.1%) in the TWLS case. All curves (except the TVE pattern associated with the one-cycle DFT) are below 1% as long as $|\delta|$ is smaller than 4%. Thus, 4PM, 6PM and TWLS are potentially compliant with the steady state P-class requirements of the Standard IEEE C37.118.1-2011 (i.e.,$\text{TVE}^m_{max} \leq 1\%$ in the range ± 2 Hz). However, only the TWLS technique is potentially *M-class* compliant, since it does not exceed the 1% boundary for $\delta = \pm 10\%$. Evidently, the considered estimators (as they are commonly proposed in the literature) rely on a different number of collected waveform cycles to return a single phasor estimate, i.e. one cycle for DFT, two cycles for 4PM, three cycles for 6PM and four-cycles (plus 1 sample) for TWLS.

3.3.2 Effect of amplitude and phase modulation

Assume that the electrical waveform (3.2) exhibits significant sinusoidal oscillations in amplitude or in phase. In such cases, according to the Standard IEEE C37.118.1-2011, the TVE must be below 3% when:
i) the modulation depth factors are up to 0.1;
ii) the modulating signal frequencies lie between 0.1 Hz and 2 Hz for *P-class* compliance,

and between 0.1 Hz and 5 Hz for *M-class* compliance, respectively. If noise, harmonics and phase oscillations in (3.2) are negligible, then we have that $\eta[n] = 0$,

$$\varepsilon_{a_r}[n] = k_a \cos\left[\frac{2\pi}{M}\delta\,(n + r \cdot N) + \alpha_a\right] \quad -\frac{N-1}{2} \leq n \leq \frac{N-1}{2} \tag{3.23}$$

and $\varepsilon_{p_r}[n]$ is the same as (3.10), for a given $r \in Z$. In (3.23) k_a represents the amplitude modulation (AM) depth factor, δ_a is the ratio between the modulating frequency f_a and f_0, and α_a is the initial phase of the modulating signal.
Dually, if noise, harmonics and amplitude oscillations are negligible, but a significant phase modulation (PM) affects the electrical waveform, it follows that $\eta[n] = 0$, $\varepsilon_{a_r}[n] = 0$ and

$$\varepsilon_{p_r}[n] = \frac{2\pi\delta}{M}\,(n + r \cdot N) + k_p \cos\left[\frac{2\pi}{M}\delta_p(n + r \cdot N) + \alpha_p\right] \quad -\frac{N-1}{2} \leq n \leq \frac{N-1}{2} \tag{3.24}$$

for $r \in Z$. In this case, k_p represents the phase modulation depth factor in radians, δ_p is the ratio between the modulating signal frequency f_p and f_0, and α_p is the initial phase of the modulating signal. Finally, if both modulations are assumed to be significant, both (3.23) and (3.24) must be included in (3.2).

Fig. 3.2 shows the maximum TVE curves as a function of δ for all the considered estimators when the worst-case values of the modulation parameters recommended in [18] are used, i.e. AM only with $k_a = 0.1$ and $\delta_a = 0.1$ (a), PM only with $k_p = 0.1$ rad and $\delta_p = 0.1$ (b) and both AM and PM with the same parameters listed above (c). All TVE curves are obtained by computing the maxima of (2.8) for $M = 64$ over 2000 runs for each estimator $m \in \{\text{DFT, 4PM, 6PM, TWLS}\}$ and for 101 equally spaced fractional off-nominal frequency offsets in the range $[-10\%, 10\%]$.

In each run the initial phases α_a, α_p of the modulating signals (3.23) and (3.24) as well as the initial phase ϕ of (3.2) change randomly in the interval $[0, 2\pi]$. Additional Monte Carlo simulations have been performed using different seeds, a larger number of runs and different values of $N \geq 64$, but no significant differences have been observed. A quick visual comparison between the curves in Fig. 3.2 and the respective curves in Fig. 3.1 points out that the effect of either amplitude or phase fluctuations is generally less relevant than the influence of large off-nominal frequency offsets, despite the modulation factors are quite high. It is worth noticing that the 4PM, 6PM and TWLS techniques accurately track amplitude and phase oscillations when $|\delta|$ is close to zero, whereas they become slightly less effective when $|\delta|$ grows. Also, the TVE values associated with estimators 4PM, 6PM and TWLS are always below 3% as long as the frequency offset is less than 2 Hz (i.e., for $|\delta| \leq 4\%$). Such behavior confirms the potential *P-class* compliance of such estimators under dynamic conditions. However, only the 6PM and TWLS techniques meet the 3% TVE boundary for $|\delta| \leq 10\%$, as it is required for *M-class* compliance. If

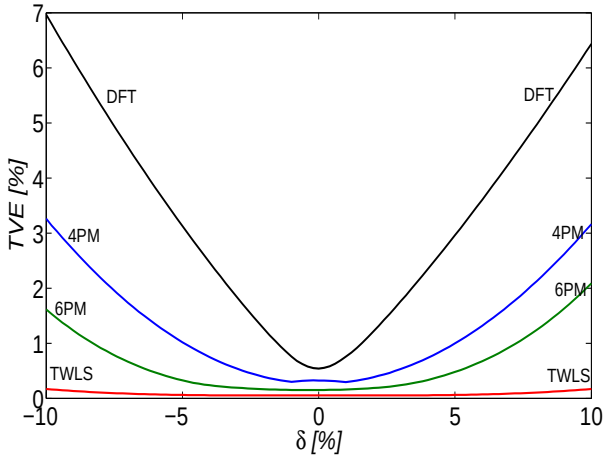

(a)

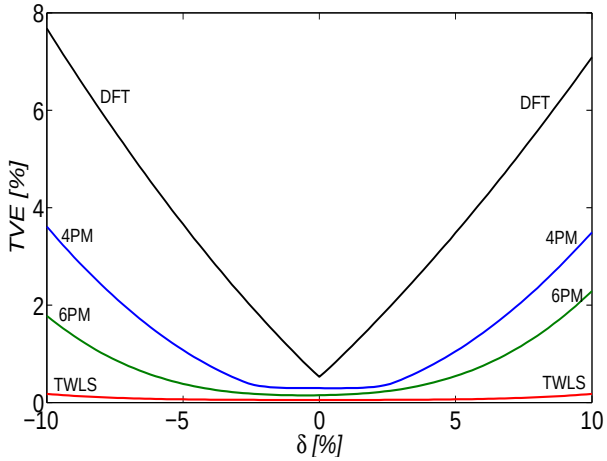

(b)

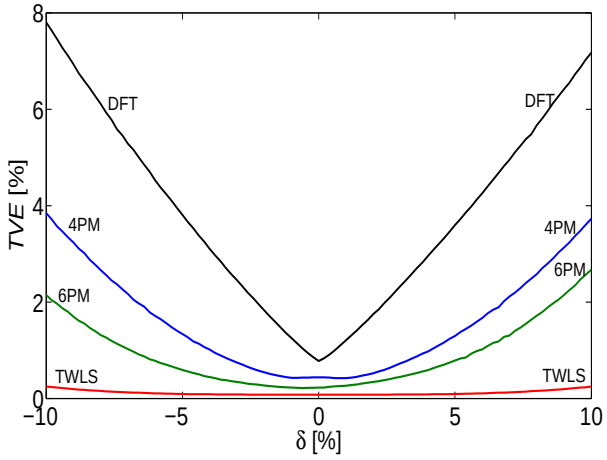

(c)

Figure 3.2: Worst-case TVE patterns associated with different phasor estimators under the influence of static off-nominal frequency offsets and sinusoidal amplitude modulation with $k_a = 0.1$ and $\delta_a = 0.1$ (a), off-nominal frequency offsets and sinusoidal phase modulation with $k_p = 0.1$ rad and $\delta_p = 0.1$ (b) or both (c).

Table 3.1: Maximum additional contribution to the TVE associated with different synchrophasor estimators due to AM or/and PM. All modulation parameters are set equal to the worst-case conditions recommended in the Standard IEEE C37.118.1-2011.

Δ_d^m	**DFT**	**4PM**	**6PM**	**TWLS**
AM	0.5%	0.3%	0.4%	0.08%
PM	0.8%	0.6%	0.6%	0.08%
AM+PM	0.9%	0.9%	0.9%	0.1%

we refer to Δ_d^m, for $d \in \{\text{AM, PM, AM+PM}\}$, as the largest TVE increments due to AM, PM or both, an upper-bound to the TVE in the presence of amplitude and/or phase modulation is given by:

$$\text{TVE}_{UB_d}^m(\delta) = \text{TVE}_{max}^m(\delta) + \Delta_d^m \tag{3.25}$$

where the superscript $m \in$\{DFT, 4PM, 6PM, TWLS\} refers to the chosen estimation technique and TVE_{max}^m results from (3.11)-(3.22), respectively. The values of Δ_d^m are summarized in Tab. 3.1 and are generally smaller than the TVE caused by the off-nominal frequency offsets alone, provided that $|\delta|$ is large enough. The only exceptions refer to the case of TWLS estimator, whose Δ_d^m values become comparable to the maximum TVE contributions due to the off-nominal frequency offsets alone, especially when both AM and PM occur. In any case the sensitivity of all algorithms to PM oscillations is always slightly larger than to AM fluctuations. The sensitivity of the four considered estimators to the various modulation parameters has been analyzed by changing both the modulation depth factor and the modulating frequency.

Fig. 3.3 shows the additional contributions to the maximum TVE values due to PM, after compensating the influence of the off-nominal frequency offsets. The lines in Fig. 3.3(a)-3.3(b) refer to different estimators and are plotted as a function of the modulation factor k_p, for $\delta = 0\%$ and $\delta = 10\%$, respectively, after setting $\delta_p = 0.1$ in both cases.

Fig. 3.3(c)-3.3(d) shows the TVE increments due to PM as a function of δ_p, for $\delta = 0\%$ and $\delta = 10\%$, respectively, after setting k_p= 0.1 rad. It is worth noticing that in most cases the maximum TVE values grow roughly linearly with the modulation parameters. As stated above, the 4PM and 6PM techniques effectively track the phasor variations around the nominal frequency with increasingly better performance. However, their sensitivity to PM degrades and become comparable to the DFT technique when $|\delta|$ grows. Therefore, when δ is close to one of the extreme values recommended in the Standard (i.e. $|\delta| = 10\%$), the 4PM and 6PM techniques outperform the DFT estimator mostly because of their capability to mitigate the TVE growth caused by the off-nominal frequency offsets,

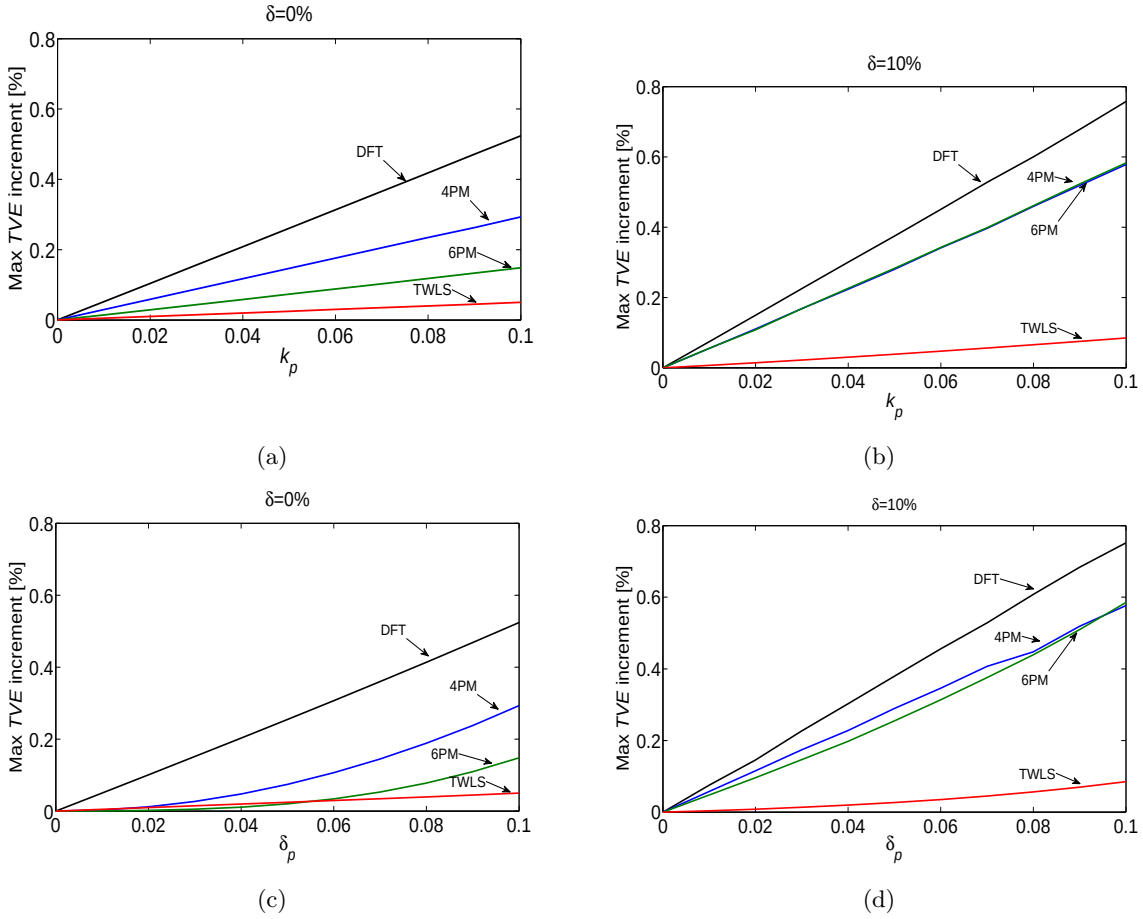

Figure 3.3: Worst-case TVE increments as a function of different PM parameters for $\delta = 0\%$ (a)-(c) and $\delta = 10\%$ (b)-(d). In (a) and (b) $\delta_p = 0.1$, while in (c) and (d) $k_p = 0.1$.

regardless of the amount of amplitude or phase modulations.

On the contrary, the TWLS estimator is more insensitive than the others to PM, while the influence of static frequency offsets and PM on the TVE are comparable. The results of the TVE sensitivity analysis to the AM parameters are shown in Fig. 3.4. The meaning of the curves and the values of the dual modulation parameters δ_a and k_a is the same as those in Fig. 3.3. The trend of the various patterns and the related considerations are also quite similar. Even if the curves in Fig. 3.4(d) do not exhibit a linear behavior any longer, the DFT, 4PM, 6PM and TWLS estimators (in this order) have increasingly better performance in tracking possible AM fluctuations.

In addition, the AM sensitivity variations of each method are less affected by static off-nominal offsets than in the PM case.

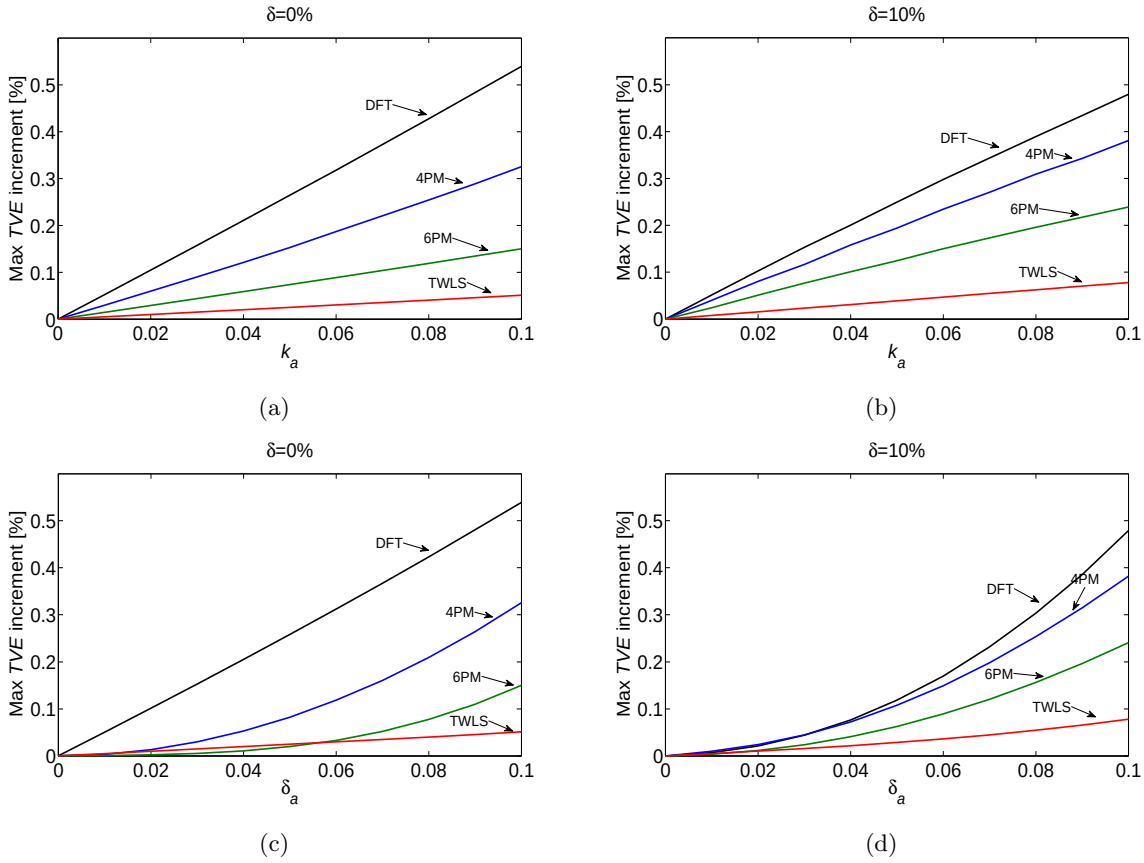

Figure 3.4: Worst-case TVE increments as a function of different AM parameters for $\delta = 0\%$ (a)-(c) and $\delta = 10\%$ (b)-(d). In (a) and (b) $\delta_a = 0.1$, while in (c) and (d) $k_a = 0.1$.

3.3.3 Effect of harmonics

In the previous section the effect of harmonics or wideband noise was assumed to be negligible. In the following the influence of either disturbance is evaluated separately. In terms of notation, the effect of harmonics in (3.2) can be modeled as

$$\eta[n] = \sum_{h=2}^{H} X_h \cdot \cos\left[\frac{2\pi}{M} h(1+\delta)\left(n + r \cdot + \frac{1}{2}\right) + \alpha_h\right] \qquad -\frac{N-1}{2} \leq n \leq \frac{N-1}{2} \tag{3.26}$$

for $r \in Z$. In (3.26) A_h and α_h are the amplitude and the initial phase of the hth harmonic for $h = 1, \ldots, H$ and H is the number of harmonics with a significant amplitude. According to the Standard IEEE C37.118.1-2011, the first 50 harmonics should be taken into account individually. In particular, a necessary condition for *P-class* or *M-class* compliance is to assure that $TVE \leq 1\%$ when the amplitude of each harmonic up to the $50th$ is either 1% or 10% of the fundamental component, respectively. In order to assess the impact of harmonic distortion, several Monte Carlo simulations have been performed

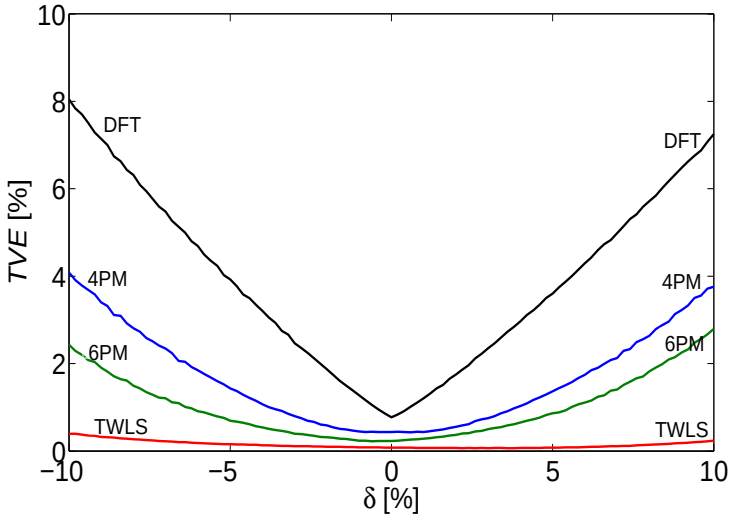

(a)

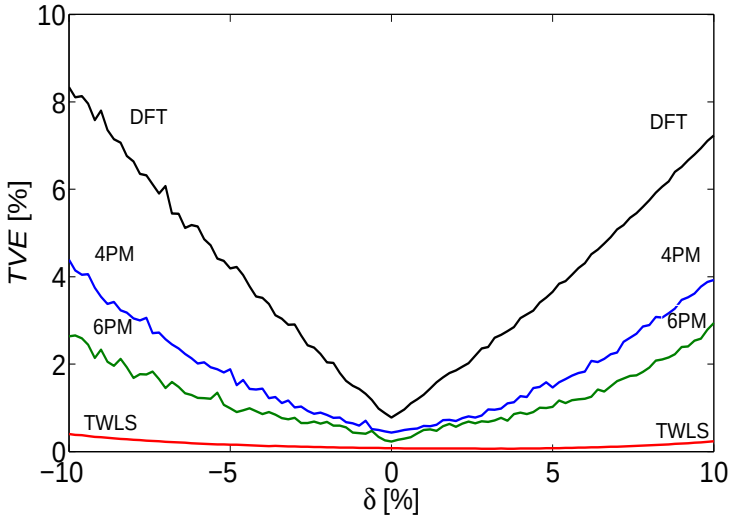

(b)

Figure 3.5: Worst-case TVE patterns associated with different phasor estimators under the influence of harmonics, static frequency offsets and sinusoidal amplitude and phase modulations with $k_a = 0.1$, $\delta a = 0.1$, $k_p = 0.1$ rad and $\delta_p = 0.1$. In (a) just the second-order harmonic is included, while in (b) all harmonics till the $50th$ are considered. In both cases the amplitude of all harmonics is set equal to 1% of the fundamental tone.

including AM and PM modulation, different static off-nominal frequency offsets in the range $[-10\%, 10\%]$ and one or multiple harmonics of relative amplitude equal to 1% of the fundamental component. Each simulation consists of 2000 runs. Also $M = 128$ samples per cycle was used to avoid aliasing problems. In each run the initial phases of the modulating signals, the fundamental tone and the harmonics change randomly in the interval $[0, 2\pi]$.

Fig. 3.5 shows the worst-case TVE patterns for every analyzed estimator when just only the second harmonic or all harmonics till the $50th$ are considered, respectively. In all cases the fundamental component is modulated both in amplitude and in phase with parameter values equal to the maxima specified in the Standard C37.118.1-2011 (i.e. $k_a = 0.1$, $\delta_a = 0.1$, $k_p = 0.1$ rad and $\delta_p = 0.1$). The corresponding upper bound to the TVE can be expressed as

$$\mathrm{TVE}^m_{UB_{H,d}}(\delta) \cong \mathrm{TVE}^m_{max}(\delta) + \Delta^m_d + \sum_{h=1}^{H} \Delta^m_{h_d}, \tag{3.27}$$

where $m \in$ {DFT, 4PM, 6PM, TWLS}, $d \in$ {AM, PM, AM+PM}, $\mathrm{TVE}^m_{max}(\delta)$ results from (3.11)-(3.22), the Δ^m_d values are those described in 3.1, and the sum $\sum_{h=1}^{H} \Delta^m_{h_d}$ represents the cumulative worst-case TVE increment due to the superimposition of H harmonics. The individual contributions associated with the second-order and the third-order harmonic (namely for $h = 2$, $h = 3$) when their relative amplitude is equal to 1% of the fundamental component are reported in Tab.3.2. As expected, the second-order harmonic has the largest influence due to its minimal spectral distance from the fundamental frequency. Observe that the TVE increments for $h = 3$ become negligible when the 6PM or the TWLS techniques are used. No precise $\Delta^m_{3_d}$ values are reported in this case because they are so small as to be comparable with the uncertainty due to the finite number of simulation runs. Similarly, the values of $\Delta^m_{h_d}$ for $h > 3$ are not reported in Tab.3.2, because they are negligible in all cases. In fact, when the off-nominal frequency offset δ changes between $[-10\%, 10\%]$, the harmonic frequencies do not fall any longer on the zero-crossings of the discrete-time window Fourier transform (e.g. rectangular in all cases except the TWLS) that multiplies the input data. As a result, the worst-case TVE influence of the second- and third-order harmonics depends on how the magnitude of the window spectrum side-lobes affect the considered estimator.

Fig. 3.5 shows also that the 6PM and TWLS techniques assure a maximum TVE value lower than 1% under the joint effect of AM, PM and harmonics when $|\delta| \geq 4\%$. However, when harmonics with a relative amplitude up to 10% are considered (as it is required for *M-class* compliance) the values of $\Delta^m_{h_d}$ (not reported here for the sake of brevity) become about 1 order of magnitude larger than those in Tab. 3.2. Accordingly, the overall 1% TVE limit specified in the Standard IEEE C37.118.1-2011 is exceeded and the *M-class* compliance cannot be achieved by anyone of the considered estimators.

3.3.4 Effect of wideband noise

In order to analyze the impact of wideband noise on phasor estimator accuracy, further Monte Carlo simulations have been performed assuming that $\eta[n]$ is a white, Gaussian noise sequence with a zero mean and a variable standard deviation. No harmonics and

off-nominal offsets have been included in this new set of simulations. Again, the AM and PM modulation parameters are equal to the maxima specified in the Standard C37.118.1-2011 (i.e., $k_a = 0.1$, $\delta_a = 0.1$, $k_p = 0.1$ rad and $\delta_p = 0.1$) and M=128 samples per cycle are acquired. However, the values of ϕ, α_a and α_p in (3.2), (3.23) and (3.24), respectively, in this case do not change randomly. In fact, they are chosen in such a way that the TVE values associated to the various estimators reach their respective maxima. Hence, during simulations, the TVE contribution due to amplitude and phase modulations is constant and equal to the maximum value reported in Fig. 3.2(c) for a certain value of δ. In every simulation run, 1000 noise sequences of given variance have been added to a waveform of known power. This procedure has been repeated for different signal-to-noise ratio (SNR) values.

The TVE mean values and standard deviations related to the DFT, 4PM, 6PM and TWLS techniques are plotted as a function of SNR for $\delta = 0\%$ in Fig. 3.6, respectively. Observe that when the SNR exceeds 40 dB, the effect of wideband noise is negligible. In fact, the mean value patterns converge to the same results reported in Fig. 3.2 when $\delta = 0\%$. In addition, the TVE standard deviations for $SNR \geq 40$ dB are in the order of 0.1% or below. Quite interestingly, the standard deviation curves are almost independent of the chosen estimation technique. Additional simulation results confirm that they are also quite independent of the off-nominal frequency offset. It is worth noticing that the mean values are significantly influenced by noise, only when the "native" TVE contribution caused by off-nominal offsets and/or modulations is smaller than the TVE fluctuations introduced by noise. Indeed, when the SNR is below a certain threshold, the additive noise affecting the numerator of (2.8) may change the sign of the quantity $\hat{\bar{X}}_r^m - \bar{X}_r$. In such cases, the TVE values are biased by the modulus operator in (2.8). When instead the magnitude of the noise-related TVE fluctuations is not large enough to change the sign of $\hat{\bar{X}}_r^m - \bar{X}_r$, the TVE bias due to noise is negligible.
In Fig. 3.6(a) this behavior is particularly evident for the DFT estimator. Indeed, the

Table 3.2: Maximum TVE increments of different synchrophasor estimators due to the second-order and the third-order harmonics alone. The amplitude of both harmonics is set equal to 1% of the fundamental component.

$\Delta_{h_h}^m$	**h=2**				**h=3**			
	DFT	**4PM**	**6PM**	**TWLS**	**DFT**	**4PM**	**6PM**	**TWLS**
AM	0.30%	0.20%	0.30%	0.20%	0.20%	0.10%	$< 0.1\%$	$< 0.1\%$
PM	0.30%	0.30%	0.30%	0.20%	0.20%	0.20%	$< 0.1\%$	$< 0.1\%$
AM+PM	0.30%	0.30%	0.30%	0.20%	0.20%	0.20%	$< 0.1\%$	$< 0.1\%$

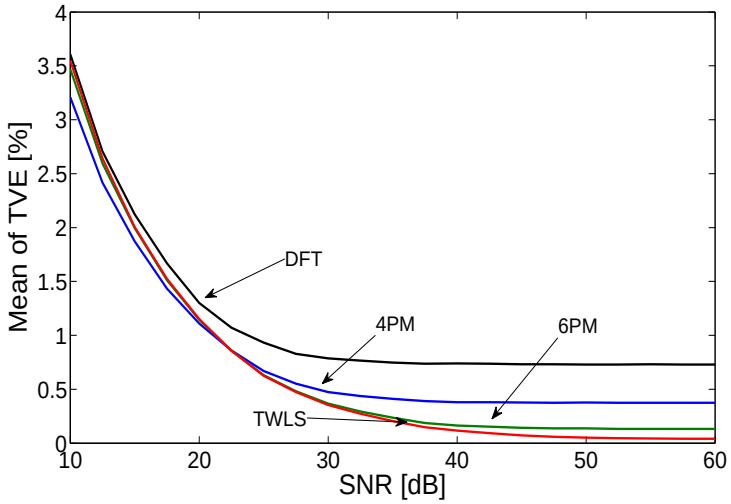

(a)

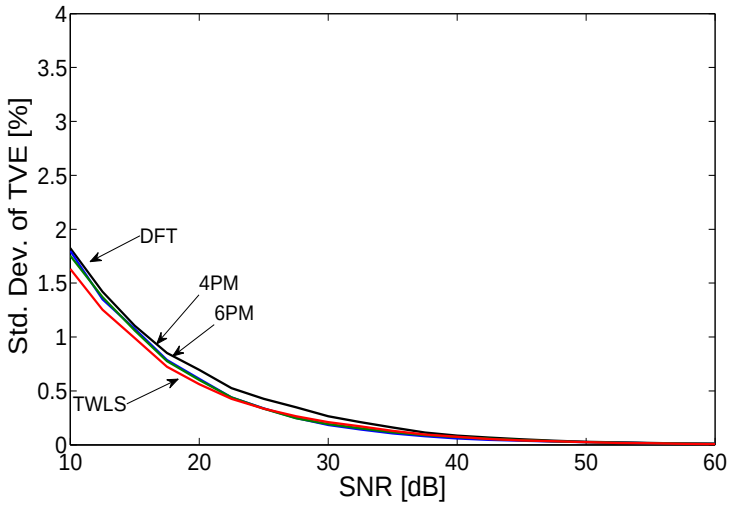

(b)

Figure 3.6: Mean (a) and standard deviation (b) values of the TVE associated with different phasor estimators as a function of the SNR for $\delta = 0\%$ and under the influence of sinusoidal amplitude and phase modulations with $k_a = 0.1$, $\delta_a = 0.1$, $k_p = 0.1$ rad and $\delta_p = 0.1$. In all cases the initial phases of both the fundamental component and the modulating signals are set so as to maximize the TVE.

TVE mean value curve tends to increase suddenly when the SNR is below 25 dB. The TVE mean value curves associated with the others estimators instead start growing for larger SNR values since their "native" TVE contribution due to modulations and/or off-nominal frequency offsets is smaller. Notice that the growth rate of the TVE mean value curves is larger than the growth rate of the respective standard deviation curves. Furthermore, if

we just focus our attention on the increment in TVE as a function of the noise power (or equivalently for decreasing SNR values) after removing the "native" TVE component, it can be observed that the noise sensitivity of the DFT estimator is slightly lower than the sensitivity of the 4PM, 6PM and TWLS techniques.

3.4 Transient performance analysis

In this section several simulations results are reported to compare the performance of DFT, 4PM, 6PM and TWLS phasor estimators under the effect of various transient disturbances. Specifically, the following cases are considered:

A. amplitude step changes both in nominal and off-nominal frequency conditions;
B. phase step changes both in nominal and off-nominal frequency conditions;
C. frequency linear ramps.

The values of all parameters modeling the transient phenomena described above are varied within the boundaries specified in the Standard, while $M = 64$ in all cases. For the sake of clarity, different types of disturbances will be analyzed in different subsections. Generally, the accuracy of phasor estimators is expressed in terms of TVE, which is defined as (2.8). However, in some applications (e.g., when the maximum tolerable timing-related phase error must be evaluated a priori [38]), the individual values of magnitude and phase estimation errors can be more useful. In particular, such quantities are defined as:

$$e_a = \frac{|\,\hat{\bar{X}}_r^m\,| - |\,\bar{X}_r\,|}{|\,\bar{X}_r\,|} \qquad e_b = \angle\hat{\bar{X}}_r^m - \angle\bar{X}_r \tag{3.28}$$

In the case of step variations the main performance parameters of interest are: the peak values of TVE and (3.28), and the *response time* defined in section 2.2.2. In the Standard the threshold to compute the response time is set equal to 1%. However, given that 1% represents a cumulative upper bound for the whole PMU, a smaller threshold (e.g., 0.3%) is advisable when just the estimation algorithm is considered. Thus, in the following, the response time values related to both $\mathrm{TVE}_r^m = 1\%$ and $\mathrm{TVE}_r^m = 0.3\%$ are reported. Further simulations performed to estimate the *delay time* show that the values are always in the order of 1-2 ms for all the considered estimators, i.e. negligible compared to the latencies introduced by the input transducers and the front-end PMU circuitry. In the case of linear frequency variations, the estimator performance is assessed in terms of TVE as a function of the frequency rate of change of the collected waveform. Again, the rate of change and the maximum frequency offset values are chosen in accordance with the Standard.

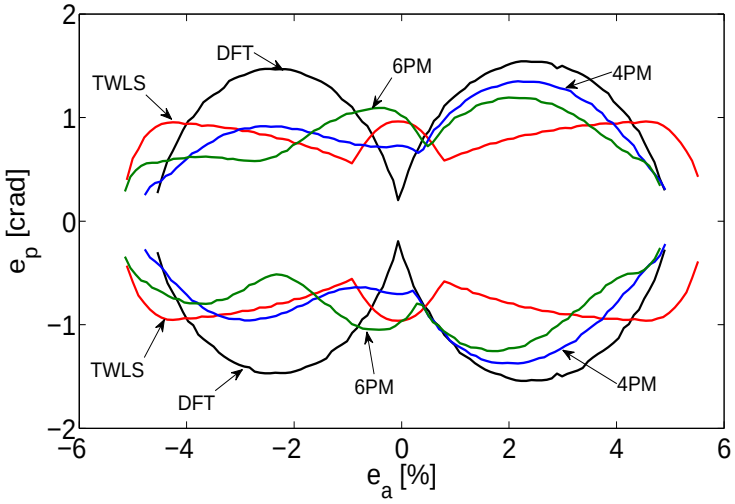

Figure 3.7: Maximum and minimum envelopes of the phase estimation errors as a function of the relative magnitude errors for 200 values of the waveform initial phase in $[0, 2\pi]$. In all cases, $\delta = 0\%$ and $k_a = 10\%$.

3.4.1 Amplitude Step Change

If both an amplitude step and a possible static frequency offset affect (3.2), the functions $\varepsilon_a(t)$ and $\varepsilon_p(t)$ are defined, respectively, as

$$\varepsilon_a(t) = k_a u(t - t_d) \qquad \varepsilon_p = 2\pi f_0 \delta t \tag{3.29}$$

where k_a is the relative size of the step with respect to amplitude A, $u(t)$ is the unit step function, t_d represents the time at which the step occurs and δ is the relative off-nominal frequency offset. It is quite clear that, for a given value of k_a, the effect of a step on the estimated synchrophasor depends on when it occurs within a waveform cycle.

The curves in Fig. 3.7 show the maximum and the minimum envelopes of $e_p(\cdot)$ (expressed in crad) as a function of $e_a(\cdot)$ (expressed in %) in nominal frequency conditions (i.e. for $\delta = 0$) and for $k_a = 10\%$. Such envelopes have been computed assuming that the step occurs always at the same time, with the waveform initial phase changing linearly by $\pi/100$ in $[0, 2\pi]$. Different line colors refer to different estimators, i.e. DFT (black line), 4PM (blue line), 6PM (green line) and TWLS (red line). Since the TVE is almost equal to the quadrature sum of phase and magnitude errors [38], it is evident that in this case the TVE values are dominated by the magnitude errors. Further simulation results (not reported here for the sake of brevity) confirm that the magnitude error increment due to an amplitude step of given size k_a is approximately the same regardless of the value of δ.

The curves in Fig. 3.8 show the worst-case TVE values returned by the four considered estimators as a function of k_a in the range $[-10\%, 10\%]$ and for $\delta = 0\%$, as suggested in [18]. Observe that two curves are plotted for each estimator. In fact, they refer to the

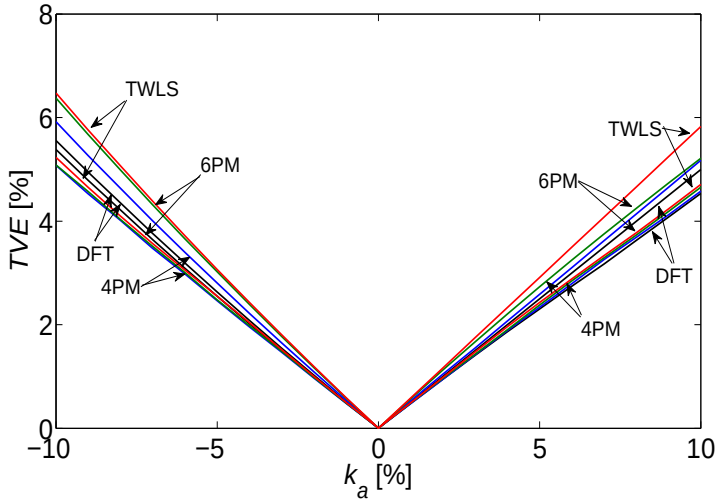

Figure 3.8: Maximum and minimum worst-case TVE patterns as a function of the relative step magnitude k_a. All patterns are obtained by changing the waveform initial phase values and the moment when the step occurs in a cycle.

minimum and maximum worst-case TVE values obtained by changing both t_d and ϕ . Note also that the TVE grows almost linearly with $|k_a|$ and that the behavior of the four estimators is very similar. Since the upper-bound to the TVE in the presence of both off-nominal frequency offsets and amplitude modulation is approximately given by the sum of both contributions [40], a similar behavior holds even when an amplitude step is considered. Indeed, by extrapolating the results of Fig. 3.8, it can be easily shown that

$$\mathrm{TVE}^{m}_{a_{peak}}(k_a,\delta) \approx \begin{cases} b_{a_1}k_a + \mathrm{TVE}^{m}_{off}\delta & k_a \geq 0 \\ b_{a_2}k_a + \mathrm{TVE}^{m}_{off}\delta & k_a < 0 \end{cases} \tag{3.30}$$

where $m \in$\{DFT, 4PM, 6PM,TWLS\} and $\mathrm{TVE}^{m}_{off}(\delta)$ is the maximum TVE contribution caused by the off-nominal frequency offset δ [40].
Coefficients $b_{a_1} = 0.51 \pm 0.06$ and $b_{a_2} = -0.58 \pm 0.07$ represent the TVE growth rates caused by the step in nominal frequency conditions (i.e., when $\delta = 0$). Consider that the uncertainty associated with both coefficients is due to both the chosen estimator and the phase of the signal when the step occurs.

Fig. 3.9 displays the worst-case response time values expressed in nominal waveform cycles, as a function of k_a in the range $[-10\%, 10\%]$ for $\delta = 0\%$ and $\delta = 4\%$ and for two different TVE thresholds, i.e. 1% and 0.3%, respectively. All curves have been obtained by changing the time at which the step occurs within a full waveform cycle and by computing the maximum response times for the same value of k_a. The evident curve asymmetry visible in Fig. 3.9(b) and 3.9(d) is due to the positive off-nominal frequency

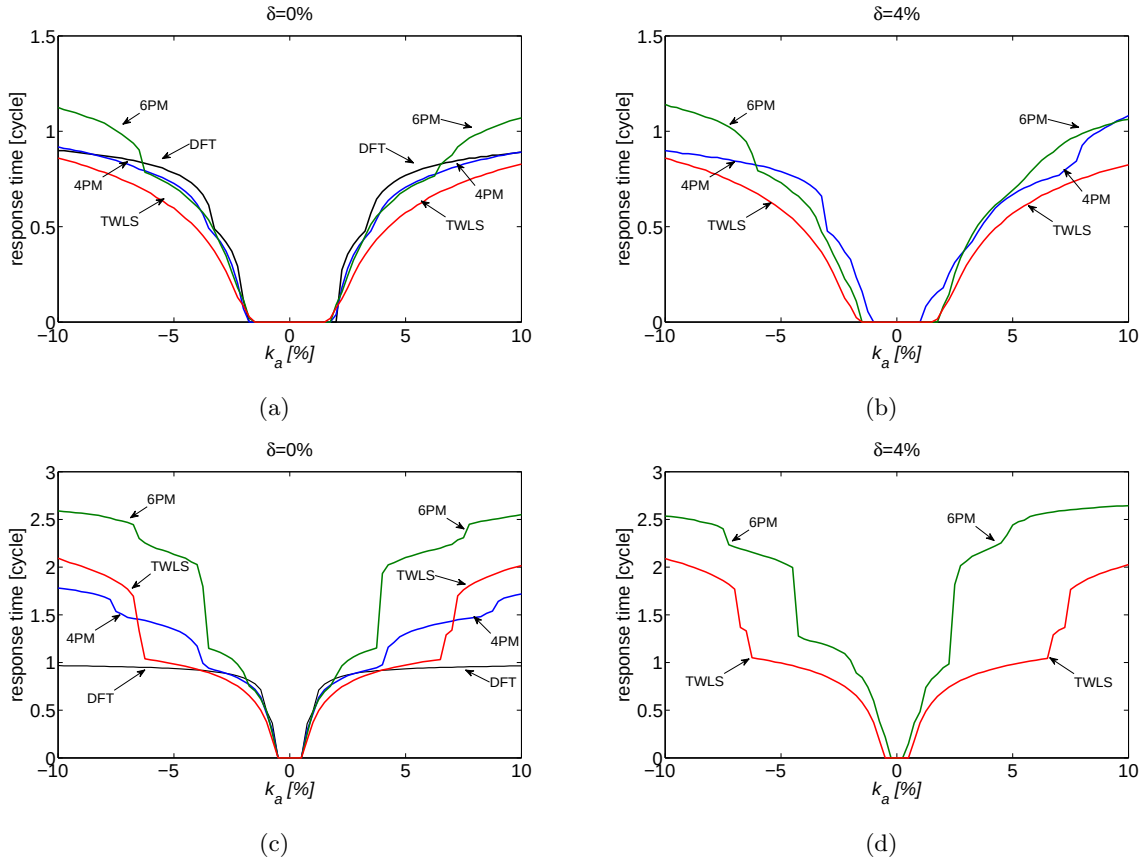

Figure 3.9: Worst-case response time values expressed in nominal waveform cycles as a function of the amplitude step size k_a for TVE=1% and $\delta = 0\%$ (a), TVE=1% and $\delta = 4\%$ (b), TVE=0.3% and $\delta = 0\%$ (c), TVE=0.3% and $\delta = 4\%$ (d). Curves are missing when the response time of the related estimator is undefined. This happens in (b) and (d) when the static off-nominal TVE is larger than the 1% or 0.3% threshold.

offset. The discontinuous behavior observable in some of the curves is due to the fact that the TVE patterns associated with some phasor estimators exhibit multiple and irregular ripples of decreasing amplitude in the time domain, as shown in Fig. 3.10. The reported TVE patterns have been obtained using a step of relative size $k_a = 5\%$ for $\delta = 0\%$ in (a) and $\delta = 4\%$ in (b), respectively. In both cases $\phi = 0$. Of course, when the step size increases, the ripple amplitude grows accordingly. As a consequence, the 1% or 0.3% TVE thresholds are suddenly and progressively crossed by multiple ripples, especially if the 6PM technique is used. An analytical expression describing the TVE pattern as a function of time when a one-cycle DFT phasor estimator is applied to a waveform of nominal frequency (i.e. with $\delta = 0\%$) is reported in the following.

Proof of expression of amplitude or phase steps effect on DFT estimators. Let us assume

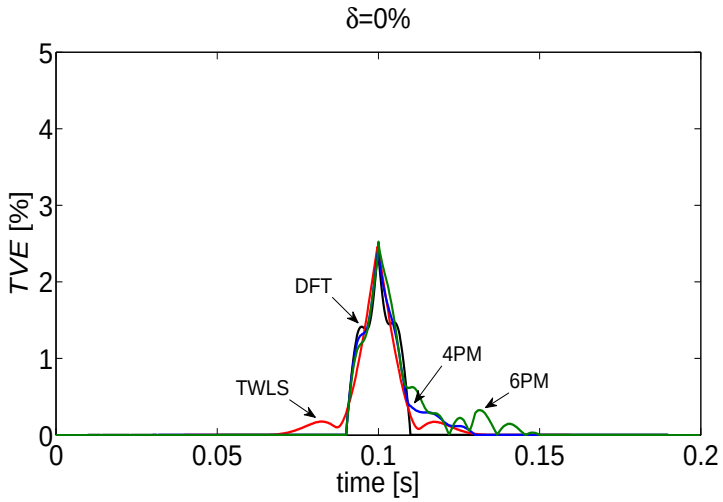

(a)

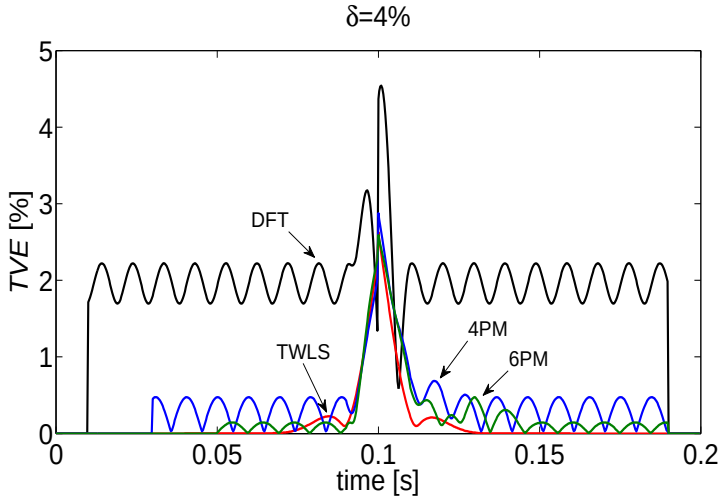

(b)

Figure 3.10: TVE patterns as a function of time for $\delta = 0\%$ (a) and $\delta = 4\%$ (b), assuming that a step of relative size $k_a = 5\%$ occurs after 0.1 s the time reference.

that an ideal electric sine wave of nominal frequency f_0 (i.e. with δ=0%) is affected by an amplitude or a phase step described by (3.29) or (3.35), respectively, at time $t_d = d/f_s$. Since steps do not change waveform frequency, when $t \geq t_d$ $x(t)$ can be easily rearranged as a sum of two sine waves of frequency f_0, i.e.

$$x(t) = X_1 \cos[2\pi f_0 t + \phi] + X_2 \cos[2\pi f_0 t + \gamma] \tag{3.31}$$

where $X_1 = A$, $X_2 = k_a \cdot A$, and $\gamma = \phi$ if an amplitude step occurs, or $X_1 = A \cdot \cos k_p$, $X_2 = A \cdot \sin k_p$, and $\gamma = \phi + \frac{\pi}{2}$ when a phase step is applied. As a result, the phasor at a

generic reference time $t_r = r/f_s$ with $r \in Z$ is given by

$$\bar{X}_r = \begin{cases} \frac{A}{\sqrt{2}} \cdot e^{j\varphi_r} & r < d \\ \frac{X_1}{\sqrt{2}} \cdot e^{j\varphi_r} + \frac{X_2}{\sqrt{2}} \cdot e^{j\gamma_r} & r > d \end{cases} \tag{3.32}$$

where φ_r is defined as in (2.4), while $\gamma_r = \varphi_r$ or $\gamma_r = \varphi_r + \frac{\pi}{2}$ depending on whether an amplitude or a phase step occurs. Suppose that the samples of (3.31) are collected by a PMU in ideal conditions (without considering noise or disturbances) and that (3.3), with $N = M$, is used to estimate (3.32). Since waveform sampling and acquisition is perfectly coherent (i.e., $f_0 = M \cdot f_s$), if the DFT observation interval does not include the step, no magnitude or phase errors affect the estimation result. On the contrary, when the step occurs within an observation interval, the estimation errors depend on how many samples are collected before d and r. From these simple considerations, it can be easily shown that

$$\mathrm{TVE}_r^{DFT} = \begin{cases} 0 & r < d - \frac{M-1}{2} + s \\ \frac{|\hat{\bar{X}}_r^{DFT} - \frac{A}{\sqrt{2}} \cdot e^{j\varphi_r}|}{|\frac{A}{\sqrt{2}} \cdot e^{j\varphi_r}|} & d - \frac{M-1}{2} + s \leqslant r < d \\ \frac{|\hat{\bar{X}}_r^{DFT} - \frac{X_1}{\sqrt{2}} \cdot e^{j\varphi_r} - \frac{X_2}{\sqrt{2}} \cdot e^{j\gamma_r}|}{|\frac{X_1}{\sqrt{2}} \cdot e^{j\varphi_r} \frac{X_2}{\sqrt{2}} \cdot e^{j\gamma_r}|} & d \leq r \leqslant d + \frac{M-1}{2} - s \\ 0 & r \geq d + \frac{M-1}{2} - s \end{cases} \tag{3.33}$$

where s=0 or 1/2 depending on whether M is an odd or an even number, respectively, and $\hat{\bar{X}}_r^{DFT}$ is the phasor estimated by (3.3). In particular after several algebraic steps, it can be proved that

$$\hat{\bar{X}}_r^{DFT} = \frac{1}{M\sqrt{2}}(A \cdot E_r + X_1 \cdot F_r + X_2 \cdot G_r) \tag{3.34}$$

where

$$\begin{aligned} E_r &= (d - r + \tfrac{M-1}{2})e^{j\varphi_r} + \frac{sin\left[\frac{2\pi}{M}\left(d - r + \frac{M-1}{2}\right)\right]}{sin\left(\frac{2\pi}{M}\right)} e^{-j\left[\frac{2\pi}{M}\left(\frac{M+1}{2} - d\right)\phi\right]} \\ F_r &= (r + \tfrac{M-1}{2} - d)e^{j\varphi_r} + \frac{sin\left[\frac{2\pi}{M}\left(r + \frac{M-1}{2} - d\right)\right]}{sin\left(\frac{2\pi}{M}\right)} e^{-j\left[\frac{2\pi}{M}\left(\frac{M+1}{2} + d\right) + \phi\right]} \\ G_r &= (r + \tfrac{M-1}{2} - d)e^{j\gamma_r} + \frac{sin\left[\frac{2\pi}{M}\left(r + \frac{M-1}{2} - d\right)\right]}{sin\left(\frac{2\pi}{M}\right)} e^{-j\left[\frac{2\pi}{M}\left(\frac{M+1}{2} + d\right) + \gamma\right]}. \end{aligned}$$

Observe that, in accordance with (3.32), the leftmost terms of E_r, F_r and G_r in (3.4.1) are responsible for the almost triangular TVE pattern behavior visible in Fig. 3.10(a). The rightmost terms in (3.4.1) instead cause TVE oscillations and ripples whose size depends on the relationship between ϕ and d. In the case of the DFT phasor estimator, such terms are very small, so they do not affect the response times significantly. However, in the other estimators (e.g. 6PM), they can be much larger. □

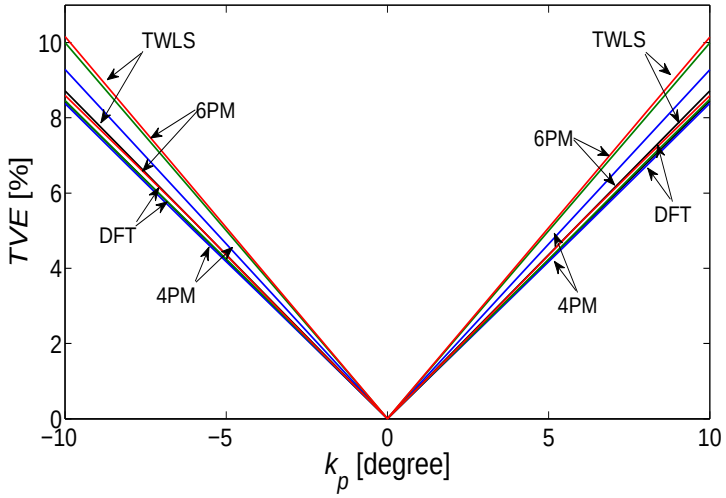

Figure 3.11: Maximum and minimum worst-case TVE patterns as a function of the relative step magnitude k_p. All patterns are obtained by changing the waveform initial phase values and the moment when the step occurs in a cycle.

The agreement between this expression and corresponding simulation results reported in Fig. 3.10(a) is excellent. Similar expressions could be also derived for the other analyzed estimators. Observe that some response time curves (namely those associated with the DFT phasor estimator in off-nominal conditions and the 4PM estimator for $\delta = 4\%$ and TVE= 0.3%) are missing. In such cases the TVE patterns are never steadily below the target threshold. Therefore, the response times are undefined. In all the other cases, the response time values are below the boundaries reported in [18] (i.e., $1.7/f_0 = 0.034$ s for *P-class* and *M-class* PMUs at the maximum reporting rate) when the TVE threshold is set to 1%. When the threshold is lowered to 0.3%, the response times generally tend to grow and become more sensitive to possible off-nominal frequency offsets. However, the TWLS technique is quite robust. Observe that, in all cases, when $|k_a|$ is small enough, the response times are zero, because the maximum TVE values are always smaller than the given threshold.

3.4.2 Phase Step Change

If a step affects the phase of waveform (3.2), but no significant amplitude variations occur, the functions $\varepsilon_a(t)$ and $\varepsilon_p(t)$ can be expressed as

$$\varepsilon_a(t) = 0 \qquad \text{and} \qquad \varepsilon_p(t) = 2\pi f_0 \delta t + k_p u(t - t_d). \tag{3.35}$$

The worst-case TVE curves related to the four considered estimators as a function of k_p in the range $[-10°, 10°]$ are shown in Fig. 3.11 for $\delta = 0\%$. Similarly to what is reported

in Fig. 3.8 all TVE patterns exhibit similar values and grow linearly with $|k_p|$. Therefore, also in this case the maximum TVE values caused by possible out-of-range phase steps can be easily extrapolated by means of the following expression

$$\mathrm{TVE}^m_{p_{peak}} = (k_p, \delta) \approx b_p|k_p| + \mathrm{TVE}^m_{off}(\delta), \tag{3.36}$$

where $m \in \{\text{DFT, 4PM, 6PM, TWLS}\}$, $b_p = 0.93 \pm 0.09$ is the TVE growth rate caused by the phase step when $\delta = 0\%$, and the meaning of $\mathrm{TVE}^m_{off}(\delta)$ is the same as in Section 3.3.1.Consider that if k_p is expressed in crad rather than in degrees, then $b_p = 0.53 \pm 0.05$. Therefore, the TVE sensitivity of all estimators to amplitude and phase steps is quite similar. Observe also that the uncertainty associated to the TVE growth rate depends on the phase of the waveform when the step occurs, as well as on the properties of the considered estimator. Nonetheless, the step-related TVE increments are quite similar for all techniques, regardless of the value of δ. Moreover, they are almost symmetric with respect to k_p and they are dominated by the phase error contribution. In Fig. 3.12 the worst-case response time curves are plotted as a function of k_p in the range $[-10°, 10°]$, for $\delta = 0\%$ and $\delta = 4\%$ and for two different TVE thresholds, i.e. 1% and 0.3%, respectively. Response time values have been obtained by changing linearly the time at which the step occurs within a full waveform cycle and are expressed in waveform cycles at the nominal frequency. Different line color refer to different estimators, in accordance with the notation already used. The considerations about the curves in Fig. 3.12 are the same as those in Fig. 3.9. However, in this case the maximum response time of the 6PM technique exceeds the $1.7/f_0$ limit reported in [18] when $|k_p| > 8°$. Again some DFT and 4PM curves are missing in Fig. 3.12(b)- 3.12(d) because the TVE is never steadily below the chosen threshold. Quite interestingly, the TWLS method exhibits excellent performance (smaller than 1 cycle) when the TVE threshold is set to 1%, even if the observation interval is about four cycles long. However, when the TVE threshold is set to 0.3%, the response time may become much longer. It is also worth noticing that the responsiveness of the TWLS method is very insensitive to δ. This is due to the very good performance of this estimator in tackling possible static frequency offsets.

3.4.3 Linear Frequency Ramp

If the frequency of the electrical waveform (3.2) is subjected to a linear variation and no amplitude changes occur, then ε_a and ε_p can be expressed as

$$\varepsilon_a(t) = 0 \qquad \text{and} \qquad \varepsilon_p = \pi R_f t^2 \tag{3.37}$$

where R_f represents the frequency rate expressed in Hz/s.

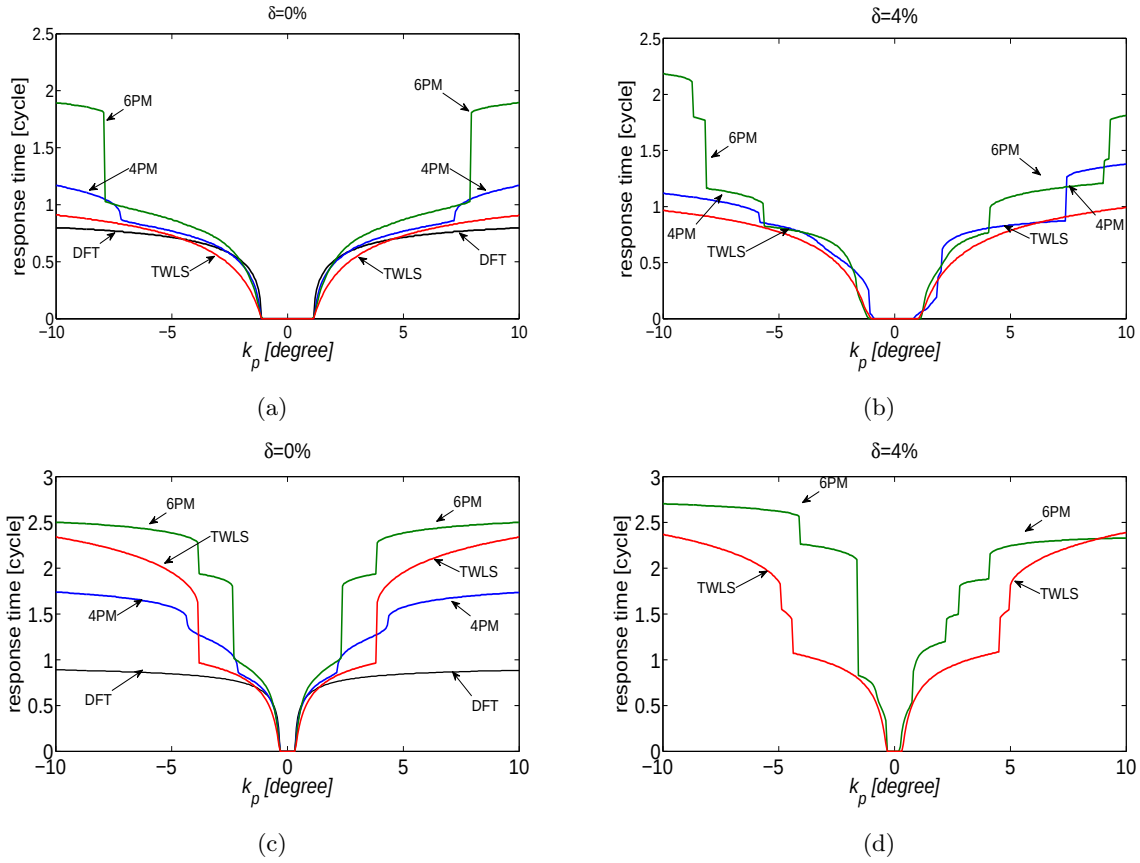

Figure 3.12: Worst-case response time values expressed in nominal cycles as a function of the phase step size kp for TVE= 1% and $\delta = 0\%$ (a), TVE= 1% and $\delta = 4\%$ (b), TVE= 0.3% and $\delta = 0\%$ (c), TVE= 0.3% and $\delta = 4\%$ (d). Curves are missing when the response time is undefined. This happens when the TVE is larger (or smaller) than 1% or 0.3%, for any value of k_p.

In Fig. 3.13 the upper TVE envelopes associated with the one-cycle DFT, the 4PM, the 6PM and the TWLS estimators, are plotted as a function of time over an interval of 5 s. In all cases the frequency rate is set equal to the upper bound specified in the Standard, namely 1 Hz/s [18]. Clearly, the TVE grows with time, as expected. However, while the TVE increment related to the TWLS estimator is basically negligible, one-cycle DFT, 4PM and 6PM violate the 1%. Clearly, the TVE grows with time, as expected. However, while the TVE increment related to the TWLS estimator is basically negligible, one-cycle DFT, 4PM and 6PM violate the 1% constraint recommended in the Standard after about 1 s, 3 s and 4 s, respectively. It is worth noticing that the relative frequency increment during a single waveform cycle is very small. In fact, the relative off-nominal frequency offset accumulated in a single waveform cycle when $R_f = 1$ Hz/s is just $4 \cdot 10^{-4}$. Therefore, the frequency changes can be regarded as quasi-static and the ramp can be reasonably

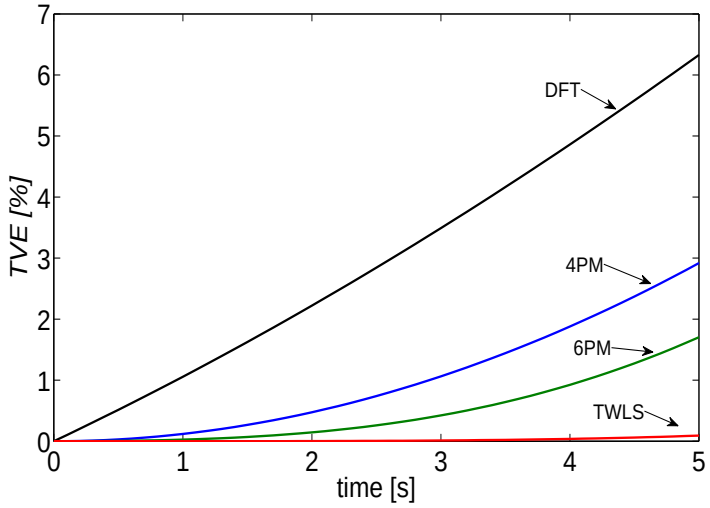

Figure 3.13: Maximum TVE envelopes in the presence of a linear frequency ramp growing with a rate of 1 Hz/s.

approximated by a staircase function built by accumulating small, frequency steps in successive observation intervals. This interpretation explains why the TVE envelopes shown in Fig. 3.13 are very close to the worst-case TVE curves reported as a function of δ in [40] and why the TWLS technique exhibits the best performance. Indeed, this estimator is excellent in static off-nominal conditions.

3.5 Conclusion

In this chapter after a presentation of state-of-art estimators, the performances of three selected synchrophasor estimators are analyzed and compared with the classic one-cycle DFT. The proposed analysis is divided in two parts.

In Section 3.3 the effect of static off-nominal frequency offsets, amplitude and phase oscillations, harmonics and noise is evaluated. We purposely took into account such phenomena in order to assess their impact on the estimator accuracy even in complex scenarios, i.e. when the electrical waveforms are affected by both quasi-stationary changes and fast fluctuations. The reported simulation results and the corresponding analytical or numerical upper bound expressions show that the 4PM and the 6PM techniques (which track the time-varying synchrophasor behavior by estimating its first- and second-order derivatives over subsequent non-overlapped observation intervals) have a moderate complexity and can be compliant with the *P-class* accuracy requirements of the Standard IEEE C37.118.1-2011, both under steady-steady and dynamic conditions, provided that the SNR is large enough. However, neither one can assure *M-class* accuracy compliance

at a reporting rate equal to or larger than 50 sample/s, since the TVE boundaries are violated in static conditions when the off-nominal frequency offset is about ±10%. The Taylor Weighted Least Squares (TWLS) phasor estimators generally assure better accuracy in all conditions, especially if a window is used to weigh the samples of the collected data records. However, also in this case the *M-class* accuracy compliance can be hardly achieved when four waveform cycles are used. Further analysis to evaluate the accuracy of these synchrophasor estimators in presence of out-of-band interferers show that all of them are sensitive and not compliant with the Standard limits.

In Section 3.4 the performances of the same estimators have been analyzed in some meaningful transient conditions described in the Standard IEEE C37.118.1-2011. The classic one-cycle DFT technique has been also included as a reference. The reported simulation results show that the TWLS approach is preferable in almost all conditions, in spite of a longer observation interval. In the presence of amplitude or phase steps, its response time is very insensitive to off-nominal frequency offsets and it is shorter than one nominal waveform cycle, when the TVE threshold is set to 1%. The peak TVE values of all estimators during step transients are generally comparable and can be so high as a few percent. Therefore, no significant differences exist between such techniques in terms of estimation accuracy. In the case of linear frequency ramps based on the parameters reported in the Standard, all estimators work in quasi-static conditions. Therefore, responsiveness is not an issue and accuracy is the same as under the effect of static frequency offsets. Again, the TWLS estimator outperforms the other techniques. Indeed, it is the only one to meet the 1% TVE limit during the transient in worst-case conditions.

Chapter 4

A Dynamic DFT-based Synchrophasor Estimator

In this chapter, a novel algorithm for synchrophasor, frequency and ROCOF estimation is defined and analyzed in depth. The proposed algorithm has been preliminary presented in [41]. At first the theoretical analysis underlying the new algorithm is presented. Afterwards, the estimation accuracy and the algorithm performances are thoroughly analyzed through simulations under different steady-state and transient testing conditions described in the Standard IEEE C37.118.1-2011. The simulation results are a subset of those reported in [41], since only the phasor estimation accuracy is considered in this dissertation. Moreover, the performances of the same algorithm for phasor angle estimation only are analyzed in depth. This could be particularly useful at the distribution level where angle measurement accuracy ha to be much higher than at the transmission level.

4.1 Interpolated Dynamic DFT IpD^{2}FT estimator

Let $x_r[n]$ be the real part of the electrical waveform acquired by a PMU as presented in (2.3),i.e.

$$\begin{aligned} x_r[n] &= Re\{A[1+\varepsilon_a(t_r+nT_s)]\cdot e^{j[2\pi f_x(t_r+nT_s)+\phi]}\} \\ &= Re\{\sqrt{2}p_r[n]e^{j\frac{2\pi}{M}(1+\delta)n}\} \end{aligned} \tag{4.1}$$

where the operator $Re\{\cdot\}$ extracts the real part of its argument, A is the waveform amplitude, $T_s = 1/f_s$ is the nominal sampling period, ϕ is the waveform initial phase

Part of this chapter was published in
G. Barchi, D. Fontanelli, D. Macii and D. Petri, "On the Accuracy of Phasor Angle Measurements in Power Networks", *on IEEE Trans. Instr. and Meas.*,vol.64, no., pp., 2015.

and $\varepsilon_a(\cdot)$ and $\varepsilon_p(\cdot)$ are the intrinsic amplitude and phase fluctuations, respectively. Note that in (4.1), the expression $p_r[n]$ denotes the waveform phasor referred to frequency $f_x = f_0(1+\delta)$ at a generic sampling time $t_r + n \cdot T_s$ already introduced in (2.4). This can be rewritten as:

$$\begin{aligned} p_r[n] &= \frac{A}{\sqrt{2}} \left[1 + \varepsilon_a(t_r + nT_s)\right] e^{j[2\pi f_0(1+\delta)t_r + \varepsilon_p(t_r+nT_s)+\phi]} \\ &= \frac{A}{\sqrt{2}} \left[1 + \varepsilon_{a_r}[n]\right] \cdot e^{j[2\pi f_0(1+\delta) + \varepsilon_{p_r}[n]+\phi]} \end{aligned} \tag{4.2}$$

As explained in Chapter 3, when a waveform phasor changes rapidly within the same observation interval, the static phasor model is no longer adequate for estimation purposes. In this situation, the waveform synchrophasor $p'_r[n]$ can be better described by its Taylor's series expansion around time t_r truncated to the kth order term. As a result, (4.1) can be rewritten as

$$x_r[n] \cong \frac{\sqrt{2}}{2} \sum_{k=0}^{K} \left(n^k p_{r,k} e^{j\frac{2\pi}{M}(1+\delta)n} + n^k p^*_{r,k} e^{-j\frac{2\pi}{M}(1+\delta)n} \right) \tag{4.3}$$

where $p_{r,k} = \frac{1}{K!} p_r^{(k)}(t_r) \cdot T_s^k$, and $p_r^{(k)}(t_r)$ is the kth order derivative of (4.2) computed at time t_r and the superscript " $*$ " denote the conjugate operator. It is worth noticing that a digitized waveform processed by a PMU includes various disturbances. Therefore, it is not expressed by (4.1), but rather by

$$s_r[n] = x_r[n] + \varepsilon_{h_r}[n] + \varepsilon_{n_r}[n] \tag{4.4}$$

where $\varepsilon_{h_r}[\cdot]$ includes all unwanted narrowband components (e.g. the first H harmonics along with other possible out-of-band interferers), and $\varepsilon_{n_r}[\cdot]$ is the additive wideband noise. Assuming that in (4.4) both narrowband and wideband disturbances are negligible (i.e. $\varepsilon_{h_r}[\cdot] \approx \varepsilon_{n_r}[\cdot] \approx 0$), if the windowed discrete-time Fourier transform is applied to (4.3), it follows that [42], [19]:

$$\begin{aligned} S_{w_r}(\lambda) \cong X_{w_r}(\lambda) &\cong \frac{\sqrt{2}}{N} \sum_{n=-\frac{N-1}{2}}^{\frac{N-1}{2}} x_r[n] w[n] e^{-j\frac{2\pi}{N}\lambda n} \\ &\cong \sum_{k=0}^{K} p_{r,k} W_k(\lambda - \nu) + p^*_{r,k} W_k(\lambda + \nu) \end{aligned} \tag{4.5}$$

where the real variable λ denotes the frequency expressed in bins, $\nu = f_x N T_s = (1+\delta) \cdot N/M$ is the fundamental frequency of (4.1) also expressed in bins,

$$W_0(\lambda) = \frac{1}{N} \sum_{n=-\frac{N-1}{2}}^{\frac{N-1}{2}} w[n] e^{-j\frac{2\pi}{N}\lambda n} \tag{4.6}$$

is the normalized discrete-time Fourier transform of the adopted window $w[\cdot]$ and

$$W_k(\lambda) = \frac{1}{N} \sum_{n=-\frac{N-1}{2}}^{\frac{N-1}{2}} n^k w[n] e^{-j\frac{2\pi}{N}\lambda n} = \left(j\frac{N}{2\pi}\right)^k \frac{d^k W(\lambda)}{d\lambda^k} \tag{4.7}$$

(with $k > 0$) is a continuous function proportional to its derivative of order k. Consider that in (4.5) ν can be also more conveniently expressed as $C + \xi$, where $C = [N/M]$ represent the nominal (integer) number of observed cycles,

$$\xi = \begin{cases} C \cdot \delta & \text{if} \quad C \cdot M \quad \text{is odd} \\ C \cdot \delta + \frac{1+\delta}{M} & \text{if} \quad C \cdot M \quad \text{is even} \end{cases} \tag{4.8}$$

Indeed, if $C \cdot M$ is an even number, an additional sample is required in order to process records consisting of an odd number of samples. If the phasor Taylor's series is truncated to the second order (i.e., $K = 2$) and the chosen window exhibits an even symmetry with respect to its central sample, the values of (4.5) for $\lambda = C + h$, $h = 1, 0, -1$, can be rearranged as follows [41]

$$S_{w_r} \cong W_P(\xi) \cdot P_r + W_I(\xi) \cdot P_r^* \tag{4.9}$$

where

$$S_{w_r} = \begin{bmatrix} S_{w_r}(C-1) \\ S_{w_r}(C) \\ S_{w_r}(C+1) \end{bmatrix} \quad P_r = \begin{bmatrix} p_{r_0} \\ p_{r_1} \\ p_{r_2} \end{bmatrix} \quad P_r^* = \begin{bmatrix} p_{r_0}^* \\ p_{r_1}^* \\ p_{r_2}^* \end{bmatrix} \tag{4.10}$$

and matrices

$$W_P(\xi) = \begin{bmatrix} W_0(-1-\xi) & W_1(-1-\xi) & W_2(-1-\xi) \\ W_0(-\xi) & W_1(-\xi) & W_2(-\xi) \\ W_0(1-\xi) & W_1(1-\xi) & W_2(1-\xi) \end{bmatrix} \tag{4.11}$$

$$W_I(\xi) = \begin{bmatrix} W_0(2C-1+\xi) & W_1(2C-1+\xi) & W_2(2C-1+\xi) \\ W_0(2C+\xi) & W_1(2C+\xi) & W_2(2C+\xi) \\ W_0(2C+1+\xi) & W_1(2C+1+\xi) & W_2(2C+1+\xi) \end{bmatrix} \tag{4.12}$$

consist just of real elements. If ξ is known, the real and the imaginary parts of vector P_r are given by

$$\begin{aligned} Re\{P_r\} &= [W_P(\xi) + W_I(\xi)]^{-1} \cdot Re\{S_{w_r}\} \\ Im\{P_r\} &= [W_P(\xi) - W_I(\xi)]^{-1} \cdot Im\{S_{w_r}\} \end{aligned} \tag{4.13}$$

In particular, by denoting the solution of (4.13) with $\hat{P}_r = [\hat{p}_{r_0}, \hat{p}_{r_1}, \hat{p}_{r_2}]^T$ the synchrophasor estimate at the reference time t_r is simply $\hat{p}_{r_0}$. If ξ is unknown instead (which is the most common case), the values of $\hat{P}_r$ can be obtained iteratively as follows. At first, ξ in (4.11) and (4.12) is assumed to be equal to 0. Then, (4.13) is computed and the value of ξ is obtained from (4.8), once the fractional frequency deviation δ is estimated from

$$\hat{\delta}(t_r) = \frac{M}{2\pi} \frac{Im\{\hat{p}_{r_1}\hat{p}^*_{r_0}\}}{|\hat{p}_{r_0}|^2} \tag{4.14}$$

The new value of ξ is then replaced into (4.13) and the same procedure is repeated till when the results of (4.14) do not change significantly. The algorithm flow chart is shown in Fig. 4.1. Indeed the convergence of the algorithm, which relies on a gradient-based approach (similarly to the classic Newton-Raphson method) is always guaranteed. In the following, the algorithm expressed by (4.5)-(4.14) will be referred to as Interpolated Dynamic DFT-based (IpD^{2}FT) synchrophasor estimator [41].

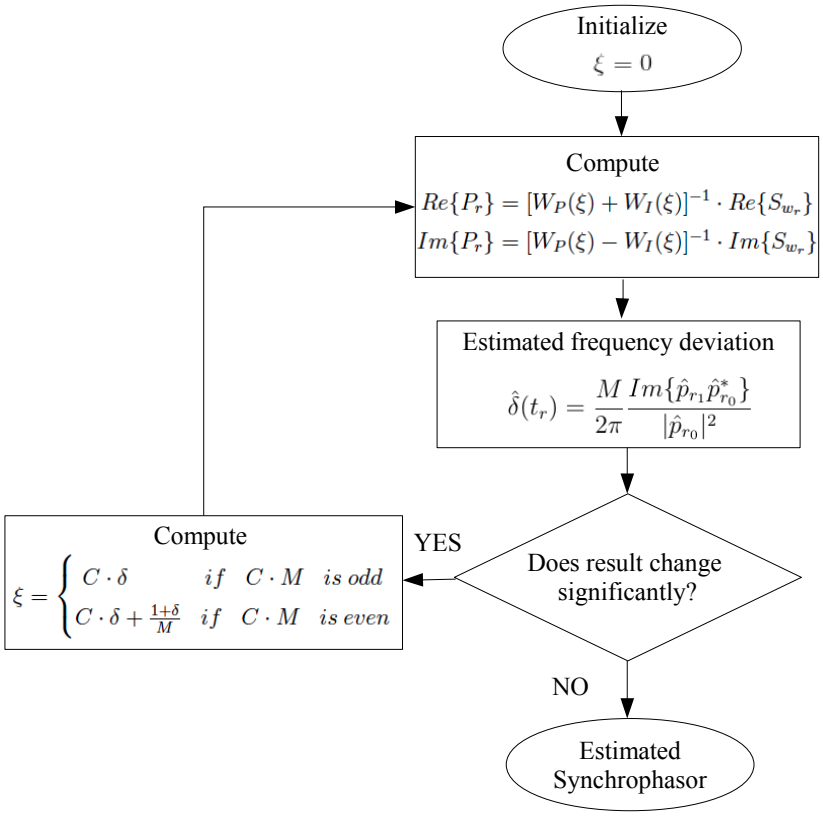

Figure 4.1: Flow chart of the Interpolated Dynamic Discrete Fourier Transform (IpD^{2}FT) algorithm.

4.2 Computational Complexity

As known, the evaluation of one DFT sample requires N complex products and N-1 complex additions. Therefore, complexity is $O(N)$, i.e. proportional to the number of collected samples. The complexity of the IpD^{2}FT algorithm is still linear with N, but it is larger than both DFT and TWLS estimators for various reasons, i.e.

- at least K+1 DFT samples of the transform of the acquired waveform have to be computed;
- $2(K+1)^2$ samples of the window spectrum have to be evaluated to build matrices (4.11) and (4.12) ;
- such matrices have to be inverted;
- the algorithm is repeated L times;
- finally at the end of each iteration a new value of ξ has to be estimated using (4.14) and (4.8).

Evidently, the computational cost of the last operations for obtaining ξ is negligible compared with the rest of the algorithm. Therefore, assuming that the number of iterations L is fixed, the order of complexity of the IpD^{2}FT estimator is approximately $O((K+1)\cdot N)+2L\cdot[O((K+1)^2\cdot N)+O((K+1)^3)]$, where the cubic rightmost term refers to the complexity of inverting a $(K+1)\times(K+1)$ matrix, using the Gauss–Jordan elimination technique. Even if the overall complexity of the IpD^{2}FT looks quite larger than the other solutions, in practice the values of both K and L are small (e.g. $K=2$ and $L=3$). Thus, the overall processing time to return a single phasor estimate is still dominated by the number of samples N, and it is just slightly higher than using a basic DFT estimator.

4.3 Simulation results

In order to analyze the performance of the proposed algorithm, multiple Monte Carlo simulations have been performed, considering f_s=6.45 kHz (i.e. $M = 129$) and different observation intervals, i.e. C=2, C=3, C=4 and C=6. The classic B-term cosine-class window functions given by [43]:

$$w[n] = \sum_{b=0}^{B-1} a_b \cos\left(\frac{2\pi}{N} bn\right) \qquad n = -\frac{(N-1)}{2}, \cdots, \frac{(N-1)}{2} \tag{4.15}$$

have been used. Of course the coefficients a_b, with b=0,...,B-1, depend on the specific window chosen since their spectra exhibit complementary performances. In particular two types of windows are considered in the following: the Minimum Side-Lobe Level (MSL) and the Maximum Side-Lobe level Decay (MSD) windows.

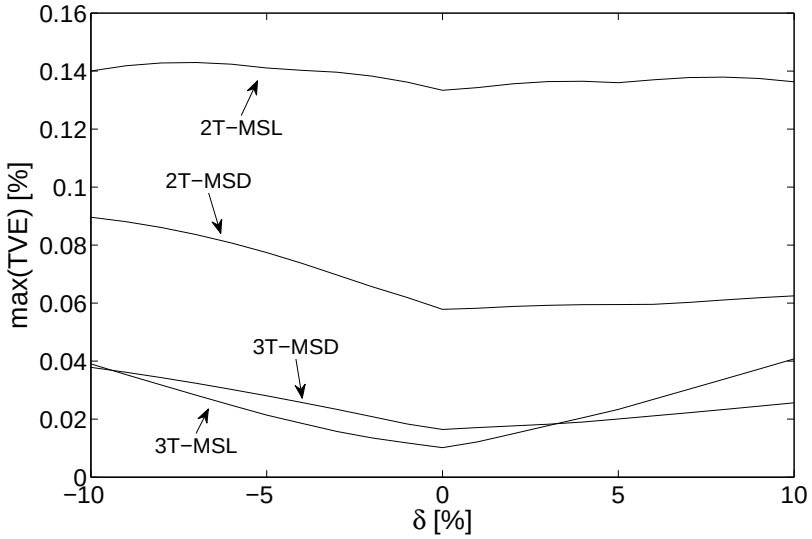

Figure 4.2: Maximum TVE values as a function of the off-nominal frequency deviations and joint effect of amplitude and phase modulations with C=3, K=2 and different windows, i.e. 2- and 3-term MSD, 2- and 3-term MSL [41].

4.3.1 Accuracy performance analysis

The accuracy performance of the IpD^{2}FT estimator has been evaluated in different scenarios recommended by the Standard.

Fig. 4.2 shows the maximum values of TVE obtained after three iterations using 2-term and 3-term MSL and MSD windows, respectively over a 3-cycle observation interval (namely with $C=3$ and $N=387$). The worst-case TVE values are plotted as a function of δ in the range $[-0.1, 0.1]$ under the effects of amplitude modulation (AM) and phase modulation (PM), but without any other disturbances (i.e. $\varepsilon_{h_r}[\cdot]$ and $\varepsilon_{n_r}[\cdot]$). Amplitude and phase of the modulating sine waves $\varepsilon_a(t)$ and $\varepsilon_p(t)$ are fixed and equal to the worst-case values reported in the Standard, i.e. $0.1{\cdot}A$ and $0.1{\cdot}f_0$ in the case of AM, and 0.1 rad and $0.1{\cdot}f_0$ for PM, respectively. The initial phases of both the fundamental component and the modulated signals are chosen randomly in $[0, 2\pi]$ and the maxima result from 300 runs.

Table 4.1 reports the maximum normalized values of TVE for four different observation interval length (i.e. $C=2$, $C=3$, $C=4$ and $C=6$) and for different types of windows. In order to better highlight the potential compliance with the requirements of the Standard, the values reported in the Table are normalized by the respective threshold values TVE$_{th}$. Such thresholds refer to the case of *M-class* PMUs with a reporting rate $RR/20$ fps. The values that exceed the Standard requirements are shadowed, in this way they are easily

identified in the Table.

In all cases the synchrophasor Taylor's series is truncated to the second-order term (i.e. $K = 2$). Some simulation have been performed assuming $K = 3$ and changing (4.10)–(4.13) accordingly. However even if the robustness of the algorithm increases in present of fluctuations, it becomes more sensitive to other disturbances (i.e. harmonics and wide-band noise). So $K=2$ guarantees globally better performance. The considered test conditions summarized below:

a) influence of a static relative frequency deviation δ alone, changing linearly in the range $|\delta| \leq 0.1$, in compliance with the worts-case requirements of the Standard IEEE C37.118.1-2011;

b) sine-wave with static frequency deviation δ, like in *case a*, affected by zero-mean additive wideband Gaussian noise with variance corresponding to a Signal-to-Noise Ratio (SNR) of 60 dB. Since this case is not considered in the Standard, the threshold is the same as in *case a*;

c) sine-wave affected by a static relative frequency deviation in the range $|\delta| \leq 0.1$ and by a second-order harmonic with magnitude equal to 10% of the fundamental tone;

d) similar to *case c*, but considering just the third-order harmonic with magnitude equal to 10% of the fundamental tone;

e) AM waveform with a carrier fundamental frequency affected by an off-nominal relative deviation $|\delta| \leq 0.1$ and with amplitude and frequency of the modulating signal equal to $0.1 \cdot A$ and $0.1 \cdot f_0$, respectively;

f) AM+PM waveform with the carrier fundamental frequency affected by an off-nominal relative deviation $|\delta| \leq 0.1$ and with AM and PM modulating frequencies and amplitude equal to $0.1 \cdot f_0$ and $0.1 \cdot A$ (for AM) and 0.1 rad (for PM), respectively;

g) sine-wave at nominal frequency perturbed by an out-of-band sinusoidal interferer with magnitude equal to 10% of the fundamental, phase chosen randomly in $[0, 2\pi)$ and frequency no smaller than 10 Hz, no larger than $2f_0$ and lying outside the interval $(f_0–RR/2,\ f_0 + RR/2)$ when $RR = 50$ fps.

The results reported in Tab. 4.1 lead to the following conclusions.

In *case a*, the estimation error, due mainly to the spectral leakage of the waveform image component and by the Taylor's series approximation error, is negligible compared with the threshold specified in the Standard.

In *case b* the combined effect of frequency deviation and wide-band Gaussian noise does not affect the TVE index.

In *case c*, the presence of 2nd-order harmonic when C=2 and C=3 may cause large TVE values, i.e. the well beyond compliance thresholds. Indeed, the discrete-time Fourier

Table 4.1: Maximum TVE normalized by threshold TVE_{th} (i.e. TVE/TVE_{th}) values obtained using the IpD^{2}FT-based estimator with the Taylor's series truncated to order K=2 and with different B-term MSL and MSD windows over 2- 3- 4- and 6-cycle intervals, respectively [41].

Case	**Test conditions**		***TVEth***	**C= 2– MSL**			**C=3 – MSL**			**C=4 – MSL**			**C=6 – MSD**		
				B=2	**B=3**	**B=4**	**B=2**	**B=3**	**B=4**	**B=2**	**B=3**	**B=4**	**B=2**	**B=3**	**B=4**
a	Freq. dev. only (±10%)		1	0	0	0.02	0	0	0	0	0	0	0	0	0
b	Freq. dev.+ noise (60 dB)	bias	1	0	0	0	0	0	0	0	0	0	0	0	0
		std.	1	0.02	0.02	0.02	0.01	0.01	0.01	0.01	0.01	0.01	0.01	0.01	0.01
c	Freq. dev.+ 2nd harm (10%)		1	6.6	8.2	11	1.3	3.3	4.7	0.12	0.5	1.4	0.06	0.02	0.04
d	Freq. dev.+ 3rd harm (10%)		1	0.13	0.21	1.2	0.13	0.01	0	0.1	0.01	0	0.01	0	0
e	Freq. dev.+ AM		3	0.03	0.03	0.14	0.04	0.01	0.01	0.06	0.03	0.02	0.16	0.08	0.05
f	Freq. dev.+ AM + PM		3	0.03	0.03	0.15	0.05	0.01	0.01	0.08	0.04	0.03	0.26	0.12	0.07
g	Out-of-band interference only		1.3	7.12	7.79	8.81	5.21	5.98	6.49	2.55	3.96	4.87	0.04	1.38	2.64

transform of a multi-frequency signal results from the superposition of the window spectrum replicas centered at different tones. If B is equal to or greater than C-1 (as it happens in Tab. 4.1), the vector X_{w_r} is heavily affected by the contribution of the second harmonic, which interferes through the window spectrum main-lobe, thus heavily perturbing the estimation result. Moreover, the amount of interference grows when B increases, because the window spectrum main-lobe becomes wider. On the other hand, when B is smaller than C-1, the interference caused by the harmonics is due to the spectrum side-lobes of the chosen window. Thus, as the difference between C and B grows, the estimation accuracy improves.

Similar considerations hold in *case d*, even though the third-order harmonics are less critical than the second-order ones, because the corresponding spectrum main-lobes are farther apart from the fundamental. Higher-order harmonics are not considered because they are filtered by the adopted windows.

The effect of amplitude and phase fluctuations, in *case e* and *f* is more relevant over longer observation intervals, regardless of the chosen window. This behavior, which is opposite to what happens in presence of off-nominal frequency deviations and harmonics, suggests that a trade-off is necessary in order to fulfill all the Standard requirements.

Finally, in *case g* the values in Tab.4.1 show that out-of-band interfering tones interharmonics generally cause large errors.. However, this effect can be mitigated by using windows with a smaller number of terms (e.g. 2) and/or by prolonging the observation interval length. Unfortunately, full *M-class* compliance in the presence of worst-case out-of-band interferers cannot be achieved using observation intervals up to six cycles.

A comparison analysis between the IpD^{2}FT-based algorithm and other techniques presented in the literature could provide some useful information. For example, considering the TWLS-based method analyzed in Chapter 3 (which is the best among those in Section 3.3 - 3.4) interesting considerations can be drawn. Obviously, due to the many parameters involved and to the dependence of TWLS algorithm on the window a full detailed one-to-one comparison is not feasible at this time. However, with reference to the results published [36] and reported in Chapter 3 when the TWLS estimator relies on a Kaiser window with $\beta = 8$ over four-cycle observation intervals, we can find that the values of TVE/TVE$_{th}$ in conditions very similar to those of cases *a*, *b*, *c*, *d*, of Tab. 4.1, are approximately in the range $[0.1, 0.3]$, i.e. well below the boundaries of the Standard, but larger than those of IpD^{2}FT . This is mainly due to the iterative frequency estimation approach, which is more effective than TWLS minimization Instead under the effect of modulations, (*cases e*, *f*) the accuracy of TWLS-based approach is about one order of magnitude better than IpD^{2}FT, because dynamic change tracking is more effective. However, both techniques largely meet the requirements of the Standard in the most cases.

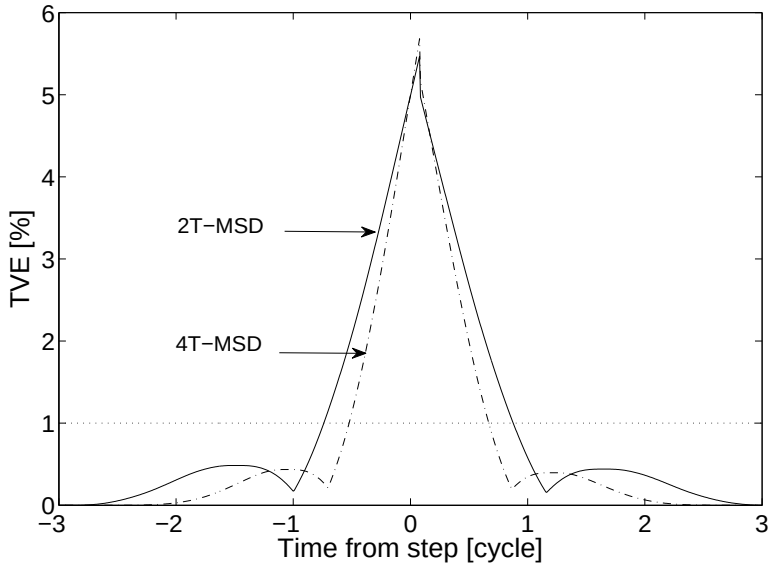

Figure 4.3: Envelopes of TVE patterns as a function of time when a 10% amplitude step occurs and the IpD^{2}FT algorithm is applied over 6-cycle observation intervals ($C = 6$) using 2-term or 4-term MSD windows. The dotted horizontal lines refer to the limits for response time estimation reported in the Standard IEEE C37.118.1-2011 [41].

Conversely in the presence of narrowband out-of-band interferers, (*case g*) the results over one and two cycles reported in [44] and in Tab.4.1 show that both synchrophasor estimators are not compliant.

4.3.2 Transient performance analysis

The behavior of the IpD^{2}FT-based estimation algorithm with K=2 in transient conditions has been analyzed through further simulations under the effect of amplitude or phase step changes and frequency linear variations. In both cases, it is assumed that δ=0, $\varepsilon_{h_r}[\cdot] = 0$ and $\varepsilon_{n_r}[\cdot] = 0$. Amplitude steps and phase steps of different size (i.e. $\varepsilon_a(t) \leq \pm 0.1A$ and $\varepsilon_p(t) \leq \pm 10^\circ$, respectively) are applied independently. The performances are evaluated in terms of response times.

Fig. 4.3 shows the worst-case envelopes of TVE as a function of time, when a 10% amplitude step occurs at time $t = 0$ and the IpD^{2}FT-based estimation algorithm is applied over six-cycle observation intervals (i.e. C=6) using 2-term or 4-term MSD windows. The envelopes are computed over multiple curves with the initial phase of the fundamental tone changing linearly in $[0, 2\pi]$. The Standard recommends a TVE limit equal to 1% for response time estimation. That limit is indicated in the plot with a dotted horizontal line. Observe that, in the worst-case, the estimation errors exhibit some ripples. In particular,

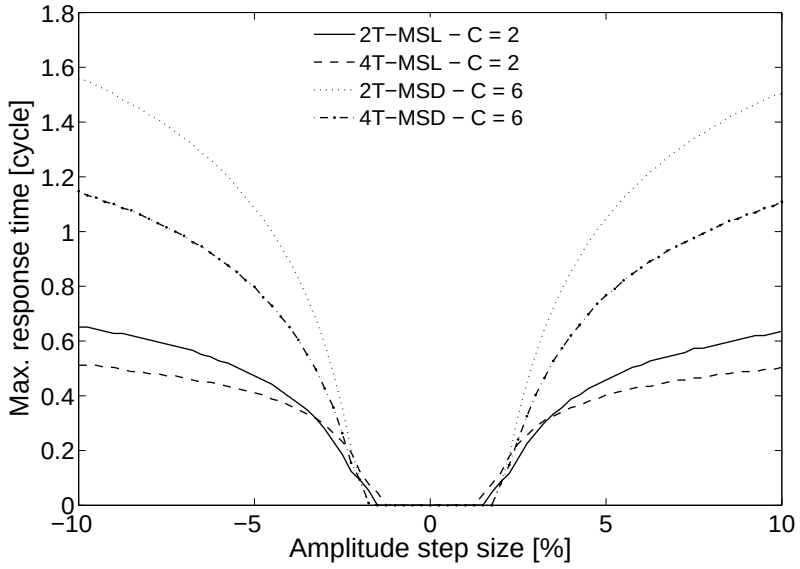

(a)

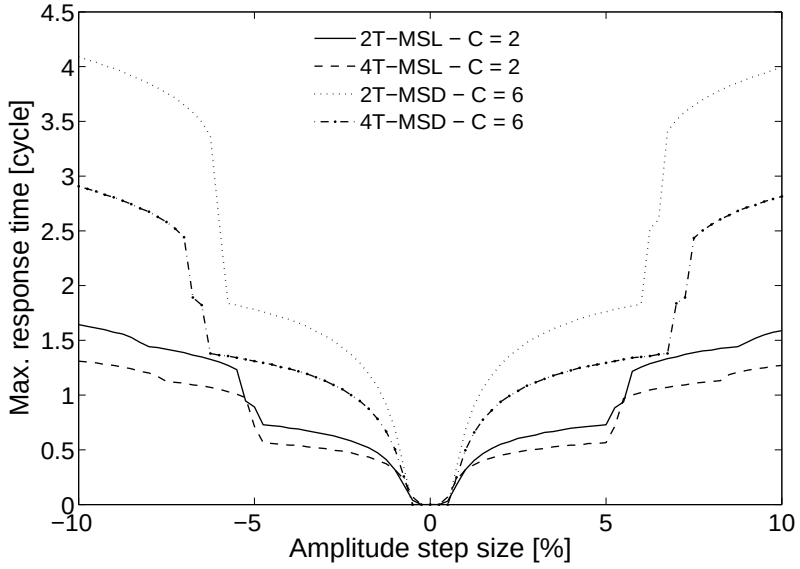

(b)

Figure 4.4: Maximum TVE response time values as a function of the amplitude step size for two different limits, i.e. 1% and 0.3% (b). Different line styles refer to observation intervals of a different duration (i.e. C=2 and C=6) using alternative windows (i.e. 2- and 4-term MSL windows, 2- and 4-term MSD windows, respectively)[41].

for a given observation interval length, the maximum absolute value of the errors during transients is larger when windows with a higher number of B terms are used. On the

contrary, the response times are shorter since the window function in the time domain decreases more quickly to zero when the number of terms grows [43]. This behavior is confirmed also in Fig. 4.4, which displays the maximum TVE response time values as a function of the amplitude step size for two different limits, i.e. 1% (a) (as recommended in [18] for the whole PMU) and 0.3% (b) (assuming that the estimation accuracy due to the algorithm only exceeds no more than 1/3 of the total PMU target accuracy). In the figure, different line styles refer to four different estimators, i.e. 2- and 4-term MSL windows over two-cycle observation intervals and 2- and 4-term MSD windows over six-cycle observation intervals respectively. As expected, the response times are lower when the observation intervals are shorter, but they grow when the limit decreases. In fact, the TVE patterns need more time to settle below a lower limit. The discontinuous behavior of the curves in Fig. 4.4(b) is due to the TVE ripples (like those shown in Fig. 4.4(a)), which cross the 0.3% limit not just once (like in the 1% case), but multiple times before lying steadily below 0.3%. The worst-case TVE response time curves resulting from phase steps in the range $[-10°, 10°]$ are quite similar to those shown in Fig. 4.4 and exhibit a similar dependence on both observation interval length and number of window terms (the corresponding curves are not reported for the sake of brevity). However, the maximum response time values due to phase steps are slightly larger than those due to amplitude steps. This behavior is confirmed in Tables 4.2 - 4.3, which reports a more compact and exhaustive comparison between the maximum TVE response times associated with different IpD^{2}FT-based estimators, when either $\pm 10\%$ amplitude steps or $\pm 10°$ phase steps occur. All numbers are expressed in terms of nominal waveform cycles. Again, the results in the Table refer to four iterations of the IpD^{2}FT algorithm with the Taylor's series truncated to order K=2 and in three different pairs of configurations, i.e.

- using a 2- or a 4-term MSL windows over two-cycle observation intervals (C=2);
- using a 2- or a 4-term MSL windows over four-cycle observation intervals (C=4);
- using a 2- or a 4-term MSD windows over six-cycle observation intervals (C=6).

Two sets of limits are considered in each case, i.e. those reported in the Standard [18] for the whole PMU and three smaller thresholds chosen arbitrarily under the assumption that the maximum estimation errors due to the algorithm only is at most a fraction of the total PMU accuracy limits reported in the Standard i.e. $TVE_{lim} = 0.3\%$. The values shadowed in Tables 4.2-4.3 refer to those conditions that do not meet the *P-Class* compliance boundaries, namely 1.7 nominal waveform cycles for TVE. Consider that the *M-class* response time boundaries in the Standard depend on the reporting rate, but in any case they are larger than the corresponding *P-class* values. Therefore, results in Tables 4.2-4.3 that are compliant with *P-class* requirements are also compliant with

Table 4.2: Maximum TVE response time of the IpD^{2}FT-based estimator with the Taylor's series truncated to order K=2, as a result of amplitude step changes. All values (expressed in nominal waveform cycles) are computed in nominal frequency conditions from the instant when TVE exceeds the respective limits (TVE_{lim}) to the time after which they permanently stay below such limits. The red values refer to the conditions that violate the *P Class* boundaries reporte in the Standard [41].

Test type		**Amplitude step** ($\pm$10%)					
Window length		**C=2**		**C=4**		**C=6**	
Window type		**MSL**		**MSL**		**MSD**	
		B=2	B=4	B=2	B=4	B=2	B=4
TVE_{lim} [%]	**1**	0.6	0.5	1.2	0.9	1.6	1.1
	0.3	1.6	1.3	3.0	2.2	4	2.9

Table 4.3: Maximum TVE response time of the IpD^{2}FT-based estimator with the Taylor's series truncated to order K=2, as a result of phase step changes. All values (expressed in nominal waveform cycles) are computed in nominal frequency conditions from the instant when TVE exceeds the respective limits (TVE_{lim}) to the time after which they permanently stay below such limits. The red values refer to the conditions that violate the *P Class* boundaries reporte in the Standard [41].

Test type		**Phase step** ($\pm 10^\circ$)					
Window length		**C=2**		**C=4**		**C=6**	
Window type		**MSL**		**MSL**		**MSD**	
		B=2	B=4	B=2	B=4	B=2	B=4
TVE_{lim} [%]	**1**	0.9	0.8	1.3	1.0	1.8	1.3
	0.3	1.8	1.4	3.4	2.6	4.5	3.3

M-class. In general, four-cycle observation intervals assure a good trade-off between accuracy and responsiveness. However, by increasing the observation interval length, responsiveness degrades. It is quite interesting to observe that when $TVE_{lim} = 1\%$ the maximum TVE response times over C=4 cycles are comparable with those obtained with a four-cycle TWLS estimator based on a Kaiser window with β=8 (i.e. about 1 cycle) as shown in Chapter 3. On the contrary, when $TVE_{lim} = 0.3\%$ the TWLS responsiveness is considerably better (i.e. slightly longer than 1 cycle against 2 to 3 cycles in the case of the proposed algorithm). Probably this is due to the smaller size of the TVE ripples resulting from the application of both the TWLS estimator and the adopted window [39]. The transient behavior of the IpD^{2}FT-based algorithm during ramps of system frequency has been also analyzed in the worst-case conditions described in [18], i.e. by choosing different random initial phases in $[0, 2\pi]$ and by changing linearly the fundamental frequency from $f_0 - 5$ Hz to f_0+5 Hz at a rate of 1 Hz/s. Again, the algorithm relies on the second order (K=2) and the same observation interval lengths and window types described previously,

i.e. 2- and 4-term MSL windows over C=2 cycles, 2- and 4-term MSL windows over C=4 cycles and 2- and 4-term MSD windows over C=6 cycles. The corresponding maximum values of TVE normalized by the respective worst-case thresholds reported in the Standard (i.e. $\text{TVE}_{ramp} = 1\%$ for *M-class* compliance) are reported in Table 4.4.

Table 4.4: Maximum TVE values obtained using the IpD^{2}FT-based estimator with the Taylor's series truncated to order K=2 for linear frequency ramp changes in $[f_0-5, f_0+5]$ Hz. All values are normalized by the worst-case threshold reported in the Standard [18], i.e. TVE_{ramp}=1%.

Test type		**Frequency ramp**					
Window length		**C=2**		**C=4**		**C=6**	
Window type		**MSL**		**MSL**		**MSD**	
		B=2	B=4	B=2	B=4	B=2	B=4
TVE_{lim}[%]	**1**	0	0.09	0.01	0	0.01	0

4.4 The problem of Phasor Angle Estimation

Various recent research works have emphasized the importance of measuring current or voltage phasor angle with high accuracy at the distribution level. Indeed, the phase offsets of the waveforms in different points of distribution networks are normally quite small, but, at the same time, they may vary considerably (both in terms of amplitude and speed), as a result of significant changes in generation or load profiles. In fact, active distribution networks are characterized by reduced line lengths, limited power flows and higher distortion levels than those of transmission networks [45]. Such features suggest that the PMU accuracy requirements at the distribution level are expected to be higher than those specified in the Standard C37.118.1-2011, although no phase measurement uncertainty limits are explicitly reported in [18] and [46]. In addition, at the distribution level the PMUs could be used to monitor electromechanical transients, which generally lead to non-negligible deviations from the nominal frequency. As a result, synchrophasors angles could be poorly estimated if waveform frequency changes within the chosen observation intervals are too relevant to be accurately measured. Moreover, both voltage magnitudes and phases greatly depend on the levels of demand and distributed generation at a given time [47]. Therefore, a PMU for distribution systems should not only track waveform phasors, frequency and ROCOF in real-time under dynamic conditions [34],[39], but it should be also able to measure phasor angles with uncertainty in the order a few mrad or less [48], as it is confirmed by the specifications of some novel instruments currently under development [49]. Generally, the phase errors result from three main contributions, i.e. unwanted phase shifts introduced by instrument transformers (which are in the order of a

few crad) [50], offsets caused by the estimation algorithm itself and deviations due to the limited time synchronization accuracy [51] or, sometimes, to the need to reconstruct the phasor values at times different from t_r [52]. The contribution of instrument transformers is not related to the PMU, so it is out the scope of this section. The uncertainty contributions due to the synchrophasor estimation algorithm is probably the most interesting, as it depends also on the features of the signals to be monitored. Since this issue is seldom considered in the literature, in this section the angle measurement accuracy of three algorithms, namely the classic DFT (3.3), the TWLS (3.6) and the IpD^{2}FT (4.5)–(4.14), is extensively analyzed. In all cases, the worst-case phasor angle measurement uncertainty of the three considered estimators has been evaluated, simply computing $Arg\{\hat{p}_r\}$.

4.4.1 Simulation and results

The accuracy of the considered phasor angle estimators has been evaluated through extensive Monte Carlo simulations in various conditions based on the Standards C37.118.1-2011 and EN 50160-2010 [18],[53]. In fact, the latter document is specifically focused on power quality requirements at the distribution level and it "*specifies the main characteristics of the voltage at a network user's supply terminals in low, medium and high voltage AC electricity networks under normal operative conditions*" [53]. Moreover, in order to test the accuracy of the phasor angle estimators in transient conditions closer to those of distribution networks, some additional simulations under the influence of decaying DC offsets are reported at the end of the tests. The choice of using two sets of testing conditions (and in some case their combination) is due to the fact that the Standard C37.118.1-2011 (along with its Amendment C37.118.1a-2014 [46]) deals with PMU performance regardless of how or where these instruments are used. On the contrary, the Standard EN 50160-2010 is specifically focused on the features of the voltage waveforms at the distribution level. All simulations rely on the same general assumption used in Section 4.3. The absolute values of the maximum phase errors associated with the DFT, IpD^{2}FT and TWLS estimation algorithms are shown in Tables 4.5, 4.6 and 4.7, respectively. All data are expressed in mrad. The tests taken into consideration comprise the same conditions already used to build Tab. 4.1, i.e. (*case a – g*), but includes a few additional ones, which are likely to better represent the operating conditions of active distribution networks, i.e.

h) the fundamental frequency is assumed to be nominal, but the collected waveform is affected by an amplitude step of magnitude equal to ±10% of the nominal value;

i) the fundamental frequency is assumed to be nominal, but the collected waveform is affected by a phase step of ±10° (i.e. $\pm\pi/18$), according with the worst-case conditions reported in [18];

j) the waveform exhibits a fundamental frequency deviation δ in the range $[-0.1, 0.1]$ and it is perturbed by all harmonics till the $25th$. Each harmonic amplitude is compliant with the worst-case specified in the Standard EN 50160-2010 [53];

k) finally, we consider the superposition of the harmonic disturbances described in *case j* with the AM and PM modulations described *case f*.

The results reported in Tables 4.5, 4.6 and 4.7 show the following considerations. In the case of static off-nominal frequency deviations only (*case a*) the IpD^{2}FT method is slightly better than the TWLS approach and both techniques outperform the DFT-based estimator. However, the maximum phase errors associated with any algorithm can be made negligible by increasing the observation interval length. Such results are basically the same as those obtained by changing linearly δ at a rate of 1 Hz/s, as described in the case of ramp testing in [18] and [46], since this rate of change of frequency causes very small frequency changes when considering short observation intervals.

In the presence of noise, *case b*, the DFT-based estimator provides the best accuracy, while the dynamic estimators exhibit similar performances. Also, the standard deviations of the estimation is reduced by using longer observation intervals.

The classic DFT-based approach is generally also less sensitive to harmonics than the IpD^{2}FT estimator, which in turn performs better than the TWLS algorithm in cases *c*), *d*) and *j*). The higher sensitivity of the dynamic approaches to harmonics is mainly due to the use of phasor derivatives. Again, in all cases considered the maximum phase errors can be reduced by increasing the observation interval length.

Under the effect of amplitude and/or phase modulation, in cases *e*) and *f*), both the TWLS technique and the IpD^{2}FT algorithm outperform the classic DFT-based estimator, as expected, since they take advantage of the dynamic phasor model. However, unlike the previous cases, the accuracy of all techniques degrades when C grows. This is quite intuitive because phasor changes are smoothed by longer intervals.

The considerations above suggest that, in the presence of both steady-state harmonic distortion and modulations (*case k*), for a given type of window, the best accuracy results from the trade-off between opposite trends. This is not clearly visible from Tables 4.5 - 4.7, since, with the chosen values of C, the effect of harmonics prevails over modulations. As a consequence, the maximum phase errors for a given number of window terms B, apparently decrease monotonically. However, further simulations confirm that, the phase error values exhibit a growing trend as soon as, by increasing C, the effect of modulations prevails over harmonic distortion.

When a large out-of-band interferer is close to the fundamental tone (*case g*) the phase errors associated with all estimators become quite large. However, the DFT estimator is much less sensitive to the out-of-band interferers than the IpD^{2}FT algorithm. In turn,

Table 4.5: Maximum absolute values of the phase estimation errors (expressed in mrad) obtained with the classic DFT-based phasor estimation algorithm in different testing conditions. 2-,3- or 4-term MSD windows over observation intervals with a duration between about 2 and 6 waveform cycles.

Case	**Test conditions**	**Max [mrad]**	**2-term MSD**			**3-term MSD**			**4-term MSD**		
			$C=2$	$C=3$	$C=4$	$C=3$	$C=4$	$C=5$	$C=4$	$C=5$	$C=6$
a	Freq. dev. only $[-10\%, 10\%]$[1]	|err.|	3.5	1.5	0.8	0.2	0.1	0.0	0.0	0.0	0.0
b	Freq. dev. $[-10\%, 10\%]$[1] + noise (SNR=40 dB)	|err. bias|	0.1	0.1	0.1	0.1	0.1	0.1	0.1	0.1	0.1
		err. std. dev.	1.3	1.1	0.7	0.7	0.7	0.6	0.7	0.6	0.6
c	Freq. dev.+2^{nd} harm. (10%)[1]	|err.|	15.6	4.3	1.5	6.4	0.5	0.1	3.0	0.1	0.0
d	Freq. dev.+3^{rd} harm. (10%)[1]	|err.|	4.3	1.5	0.8	0.2	0.1	0.0	0.0	0.0	0.0
e	Freq. dev.+AM[1]	|err.|	8.5	12.8	19.9	7.2	12.2	18.5	8.8	13.5	19.0
f	Freq. dev.+AM[1]+PM[1]	|err.|	10.4	16.8	28.2	10.3	17.8	26.5	13.0	19.4	26.6
g	10% out-of-band interferers[1]	|err.|	50.0	17.3	0.8	38.9	16.5	4.3	29.9	14.1	5.0
h	10% magnitude step[1]	|err.|	8.1	5.2	3.9	6.9	5.1	4.1	6.2	4.9	4.1
i	10° phase step[1]	|err.|	102	96.4	94.0	99.4	96.2	94.4	98.1	95.9	94.4
j	Freq. dev.+25 harm. (10%)[2]	|err.|	5.8	2.0	0.9	1.4	0.1	0.0	0.6	0.0	0.0
k	Freq. dev.+AM[1]+PM[1]+25 harm.[2]	|err.|	13.6	17.8	28.8	11.4	17.7	26.6	13.3	19.1	27.1

[1] Conditions compliant with the requirements of the Standard IEEE C37.118.1-2011

[2] Conditions compliant with the requirements of the Standard EN 50160-2010

Table 4.6: Maximum absolute values of the phase estimation errors (expressed in mrad) obtained with the classic IpD^{2}FT phasor estimation algorithm for K=2 in different testing conditions. 2-,3- or 4-term MSD windows over observation intervals with a duration between about 2 and 6 waveform cycles

Case	**Test conditions**	**Max [mrad]**	**2-term MSD**			**3-term MSD**			**4-term MSD**		
			$C=2$	$C=3$	$C=4$	$C=3$	$C=4$	$C=5$	$C=4$	$C=5$	$C=6$
a	Freq. dev. only $[-10\%, 10\%]$[1]	|err.|	0.0	0.0	0.0	0.0	0.0	0.0	0.0	0.0	0.0
b	Freq. dev. $[-10\%, 10\%]$[1] + noise (SNR=40 dB)	|err. bias|	0.1	0.1	0.1	0.1	0.1	0.1	0.1	0.1	0.1
		err. std. dev.	1.1	0.9	0.8	1.0	0.9	0.8	0.9	0.9	0.8
c	Freq. dev.+2^{nd} harm. (10%)[1]	|err.|	71.9	21.9	2.8	46.9	12.6	0.6	28.7	7.6	0.4
d	Freq. dev.+3^{rd} harm. (10%)[1]	|err.|	2.8	0.4	0.2	0.1	0.0	0.0	0.0	0.0	0.0
e	Freq. dev.+AM[1]	|err.|	2.1	0.8	1.0	0.3	0.5	1.1	0.3	0.7	1.4
f	Freq. dev.+AM[1]+PM[1]	|err.|	2.1	0.8	1.2	0.3	0.6	1.4	0.4	0.8	1.7
g	10% out-of-band interferers[1]	|err.|	98.3	73.9	43.3	85.4	64.3	39.2	75.6	55.2	34.4
h	10% magnitude step[1]	|err.|	14.9	9.5	7.2	12.6	9.1	7.1	10.6	8.3	6.9
i	10° phase step[1]	|err.|	117	105	100	109	103	100	106	102	99.2
j	Freq. dev.+25 harm. (10%)[2]	|err.|	15.7	4.4	0.6	9.4	2.5	0.1	5.7	1.5	0.1
k	Freq. dev.+AM[1]+PM[1]+25 harm.[2]	|err.|	16.4	5.2	1.6	10.4	3.1	1.4	6.3	2.3	1.7

[1] Conditions compliant with the requirements of the Standard IEEE C37.118.1-2011

[2] Conditions compliant with the requirements of the Standard EN 50160-2010

Table 4.7: Maximum absolute values of the phase estimation errors (expressed in mrad) obtained with the classic TWLS phasor estimation algorithm for K=2 in different testing conditions. 2-,3- or 4-term MSD windows over observation intervals with a duration between about 2 and 6 waveform cycles

Case	**Test conditions**	**Max [mrad]**	**2-term MSD**			**3-term MSD**			**4-term MSD**		
			$C=2$	$C=3$	$C=4$	$C=3$	$C=4$	$C=5$	$C=4$	$C=5$	$C=6$
a	Freq. dev. only $[-10\%, 10\%]$[1]	|err.|	0.6	0.0	0.0	0.2	0.0	0.0	0.0	0.0	0.0
b	Freq. dev. $[-10\%, 10\%]$[1] + noise (SNR=40 dB)	|err. bias|	0.1	0.1	0.1	0.1	0.1	0.1	0.1	0.1	0.1
		err. std. dev.	1.2	1.0	0.8	1.1	0.9	0.8	1.0	0.9	0.8
c	Freq. dev.+2^{nd} harm. (10%)[1]	|err.|	84.9	38.2	6.3	67.3	35.6	12.4	55.4	30.6	12.6
d	Freq. dev.+3^{rd} harm. (10%)[1]	|err.|	3.1	0.3	0.0	1.0	0.0	0.0	0.2	0.0	0.0
e	Freq. dev.+AM[1]	|err.|	0.8	0.4	1.0	0.3	0.4	0.9	0.2	0.5	0.9
f	Freq. dev.+AM[1]+PM[1]	|err.|	1.1	0.6	1.8	0.5	0.7	1.7	0.4	0.9	1.8
g	10% out-of-band interferers[1]	|err.|	107	83.6	59.1	96.8	80.4	63.0	89.9	77.1	61.9
h	10% magnitude step[1]	|err.|	20.7	11.6	8.4	16.6	11.5	9.0	14.3	11.0	9.0
i	10° phase step[1]	|err.|	122	107	102	116	107	103	112	107	103
j	Freq. dev.+25 harm. (10%)[2]	|err.|	17.4	7.7	1.3	13.6	7.1	2.5	11.2	6.1	2.5
k	Freq. dev.+AM[1]+PM[1]+25 harm.[2]	|err.|	18.4	8.7	3.0	14.9	8.2	3.3	12.3	7.2	3.6

[1] Conditions compliant with the requirements of the Standard IEEE C37.118.1-2011

[2] Conditions compliant with the requirements of the Standard EN 50160-2010

this is less sensitive than the TWLS estimator. Also, accuracy improves as the observation interval length increases since the frequency distance between the fundamental component and the interfering tone increases.

The maximum phase errors associated with the three estimators in transient conditions, i.e. under the effect of amplitude steps (*case h*) or phase steps (*case i*), respectively are also reported in the Tables. The DFT estimator is less sensitive to transients than the IpD^{2}FT algorithm. This, however, performs clearly better than the TWLS. As expected, the maximum error due to a phase step is much larger than the maximum error related to a magnitude step, as the former impacts directly on the phase of the waveform. Observe that in all the considered cases the errors tend to decrease, even if slowly, as the observation interval length grows. When the IpD^{2}FT algorithm is considered, the number of terms of the Taylor's series deserves a special attention. Indeed, if K increases (e.g. K=3), the observation interval length has to increase as well to avoid significant spectral interferences due to other spectral components such as harmonics or the image tone. As a result, the IpD^{2}FT algorithm responsiveness degrades, but accuracy tends to slightly improve by using K=3 rather than K=2. However, by increasing K the algorithm becomes more sensitive to wideband noise (i.e. in *case b*). Ultimately, K=2 provides a good trade-off between overall accuracy and responsiveness.

In Fig. 4.5 the maximum absolute values of the phase estimation errors associated with the DFT-based technique (a), the IpD^{2}FT algorithm (b), and the TWLS estimator (c), respectively, are compared in the testing conditions related to *case j*. The error curves are plotted as a function of δ for $C = B + 2$ cycles when a $B - term$ MSD window is used (with B = 2, 3 or 4). The plots confirm that the DFT-based solution is slightly more robust to harmonics than the others. However, the TWLS estimator can be significantly affected by harmonics when δ is negative.

Fig. 4.6 shows the maximum absolute values of the phase estimation errors associated with the DFT-based technique (a), the IpD^{2}FT algorithm (b), and the TWLS estimator (c), under the testing conditions related to the (*case f*). The adopted windows and the observation interval lengths are the same as those used in Fig. 4.5. However, in this case the IpD^{2}FT algorithm and the TWLS estimator clearly outperform the classic DFT–based approach.

Fig 4.7(a)-(b) provides an example of the transient behavior of all the analyzed estimators under the testing conditions related to the cases *h*) and *i*), respectively. In Fig. 4.7(a)-(b) the maximum phase error envelopes associated with the three estimators are plotted as a function of time expressed in nominal waveform cycles, when the observation interval is about C = 4 cycles long and a 2-term MSD window is used. The curves confirm that when an amplitude step occurs the maximum error introduced by the

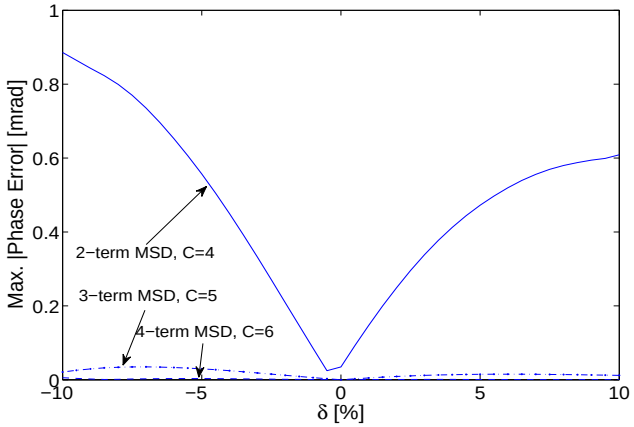

(a)

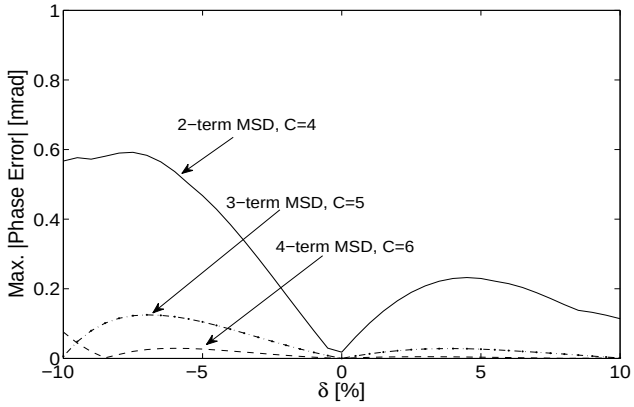

(b)

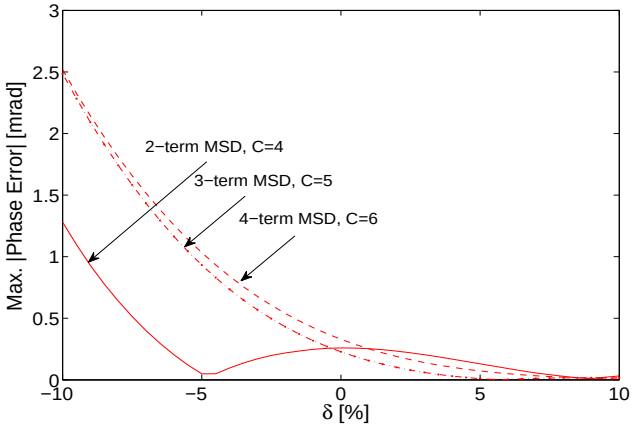

(c)

Figure 4.5: Maximum absolute values of the phase estimation errors associated with the classic DFT-based technique (a), the IpD^{2}FT algorithm (b), and the TWLS estimator (c), as a function of the static off-nominal frequency deviation δ and under the effect of a worst-case total harmonic distortion compliant with the Standard EN 50160:2010.

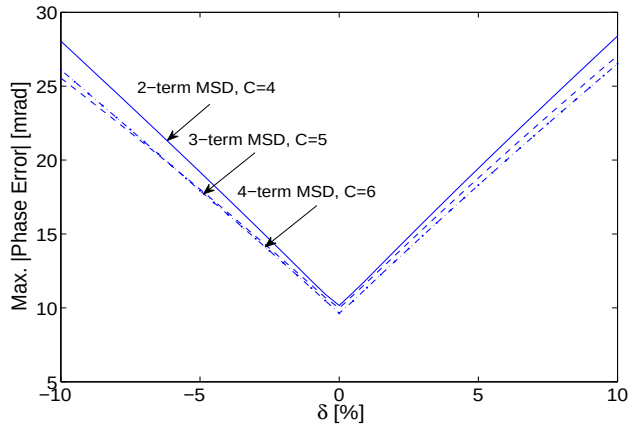

(a)

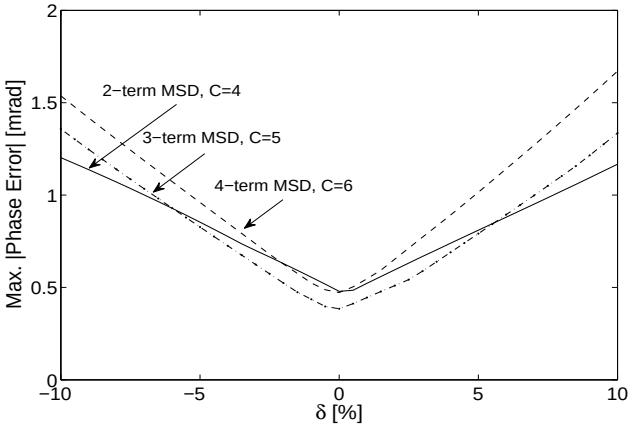

(b)

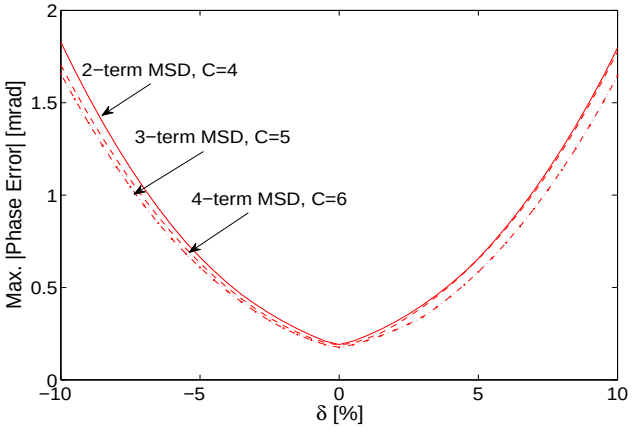

(c)

Figure 4.6: Maximum absolute values of the phase estimation errors associated with the DFT-based technique (a), the IpD2FT algorithm (b), and the TWLS estimator (c), under the joint effect of: static off-nominal frequency deviations $\delta \neq 0$, amplitude modulation (AM) and phase modulation (PM). The modulating signals are two sine-waves of amplitude equal to 10% of the fundamental and 0.1 rad for AM and PM, respectively, and frequencies equal to $0.1 \cdot f_0$.

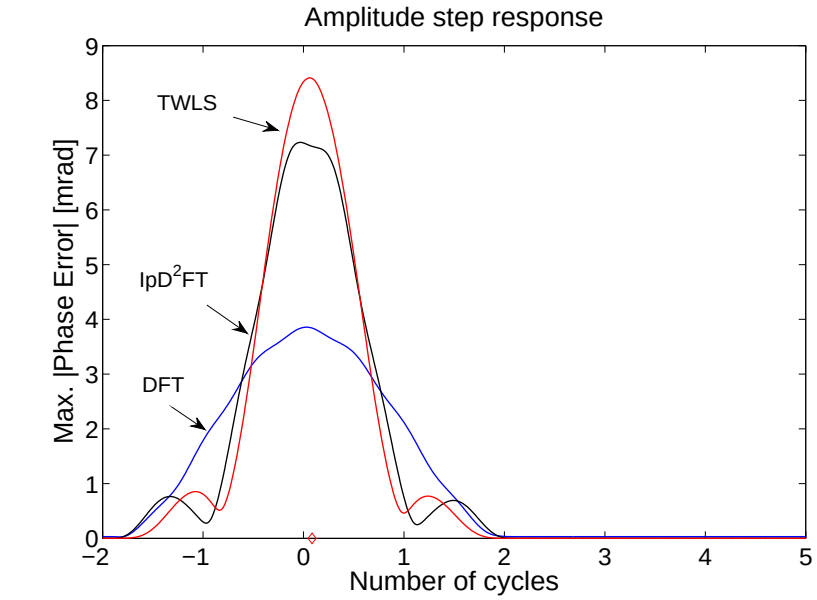

(a)

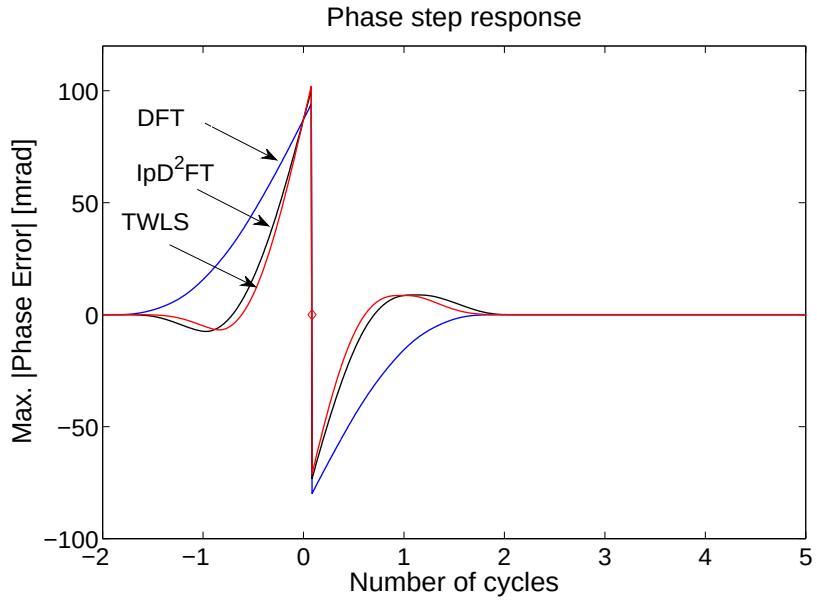

(b)

Figure 4.7: Phase errors envelopes as a function of time (expressed in nominal waveform cycles) when either a 10% magnitude step (a) or a 10° phase step occurs (b). Different line color refer to the DFT-based technique, the IpD^{2}FT algorithm and the TWLS estimator, when a 2-term MSD window is used over a four-cycle observation interval. The small diamonds highlight when the step occurs.

DFT-based estimator is generally smaller than the maximum error associated with the IpD^{2}FT algorithm or by the TWLS technique. Conversely, in the presence of phase steps, errors are much larger and quite similar. Quite interestingly, the duration of transients is almost the same for all estimators in both case *h*) and case *i*). Additional simulation results, not reported for the sake of brevity, show that the error peaks during transients are almost proportional to the step size, both in magnitude or in phase.

Since the effect of transients is particularly interesting in the case of distribution networks, some additional results under the influence of decaying DC offsets are reported in Fig. 4.8. The three curves displayed on Fig.4.8 with different line styles represent the maximum phase errors associated with the three considered estimators, when the observation interval is C=5 cycles and a 3-term MSD window is used. In all cases, exponentially decreasing DC offsets with initial amplitude equal to 70% of the fundamental and time constant τ in the range between 0.1 and 10 s are added to a sinusoidal voltage waveform of frequency f_0 [54]. Each point of the curves is the maximum phase error resulting from 200 initial phase values chosen at random in $[0, 2\pi)$. The decaying DC offset always start at the beginning of the observation intervals. The reported results show that the DFT approach is the least sensitive to the influence of such disturbances. Accuracy is about one order of magnitude worse for the IpD^{2}FT algorithm and at least two orders of magnitude

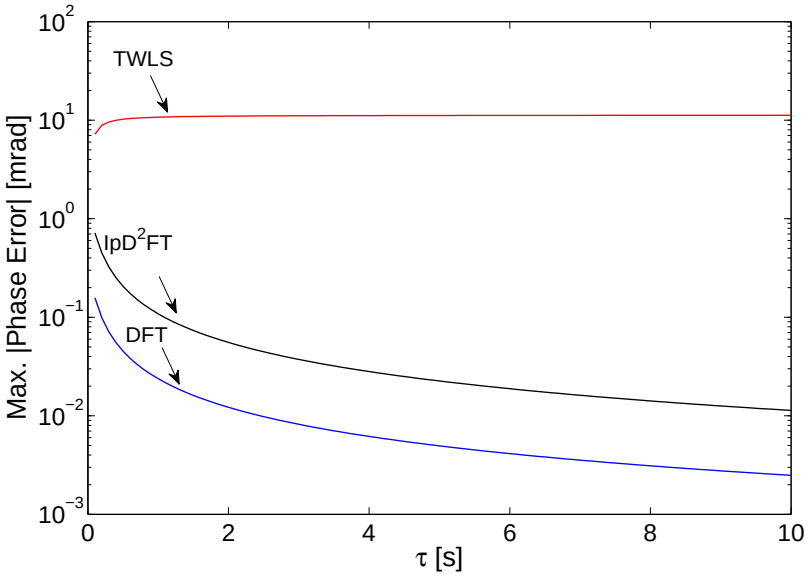

Figure 4.8: Maximum phase errors as a function of the time constant of an additive decaying DC offset of initial amplitude equal to 70% of the nominal waveform amplitude. Different line color refer to the DFT-based technique, the IpD^{2}FT algorithm and the TWLS estimator, respectively, when a 3-term MSD window is used over a five-cycle-long observation interval.

worse than the TWLS estimator. By changing the observation interval length or the type of window, similar patterns are obtained. Observe that the phase errors associated with the DFT and IpD^{2}FT estimators exhibit a monotonically decreasing trend. This is due to the fact that when τ grows, the spectral content of the decaying DC offsets is increasingly concentrated around zero, i.e. faraway from the spectral samples used by the algorithms. On the contrary, the sensitivity of the TWLS estimator to decaying DC offsets is not only larger, but it is also almost independent of the values of τ. This is due to the fact that the TWLS estimator relies on the weighted least square fitting in the time domain of a dynamic (i.e. oscillating) phasor model, which does not include any decaying DC offset. Therefore, such terms cannot be tracked with good accuracy regardless of the value of τ.

4.5 Jitter and time alignment uncertainty

The analysis performed in the previous sections was focused on the effect of phasor estimation algorithms only. However, as stated in the Section 4.4, additional uncertainty contributions arise from: sampling jitter, limited synchronization accuracy, and the need to estimate the phase of a waveform at times different from the center of the considered observation interval. The sampling jitter depends on the fact that even if the sampling clock is disciplined by a GPS receiver or by some other synchronization technique (e.g. the IEEE 1588 Precision Time Protocol [55]), the input waveform within the rth observation interval is actually sampled at times which slightly differ from $t_r + nT_s$. If we denote with δ_T the random time fluctuations of the sampling period T_s, the equivalent effect of this term on phasor estimation algorithms is to inject an additional phase modulation term in the signal model. This means that $\varepsilon_{p_r}[n]$ in (4.1) should be rather replaced by $\varepsilon'_{p_r}[n] = \varepsilon_{p_r}[n] + 2\pi \sum_{i=0}^{n} \delta_{T_s}[i]$. In addition, because of the limited synchronization accuracy, even if the delays due to the acquisition stage are properly estimated and compensated, the phase in the center of the considered observation interval is affected by some uncertainty. In particular, if t_j models the synchronization uncertainty, then the corresponding phase uncertainty at reference time t_r can be approximated by a first-order Taylor series expansion as follows:

$$\Delta\varphi_{j_r} \approx \left(2\pi f_0(1+\delta) + \frac{d\varepsilon_p}{dt}|_{t=t_r} \right) t_j. \tag{4.16}$$

In practice, the values of t_j usually range from some hundreds of ns to a few μs. For instance, if the worst-case synchronization uncertainty is 1 μs, the absolute value of the maximum phase error $\Delta\varphi_{j_{max}}$ is about 0.4 mrad, i.e. smaller than (or at most comparable to) the algorithm-related phasor estimation errors in most of the conditions considered.

A further uncertainty contribution affecting phasor angle measurements arises from the need to reconstruct the phasor data at times different from the reported ones. In fact, the PMU reporting rate depends on various factors, such as the performance class of the instrument (i.e. *P-class* or *M-class* [18]), the specific features of the PMU employed and the chosen instrument settings. When multiple streams of data are collected by (PDC) at different rates, all measurements results need to be aligned in time. In such cases, the phasor angle φ'_r at a generic time $t'_r = t_r + \Delta t$ results approximately from [52]

$$\varphi'_r \cong \varphi_r + 2\pi \left[(f_r - f_0)\Delta t + \frac{\Delta t^2}{2} ROCOF_r \right], \tag{4.17}$$

where φ_r, f_r and $ROCOF_r$ are the phase, the frequency and the $ROCOF$ values at time t_r. In practice, both f_r and $ROCOF_r$ are affected by some uncertainty that propagates to the phase estimate. If we denote with FE_r and RFE_r as the frequency and $ROCOF$ measurement errors in the rth observation interval, it results immediately from (4.17) that the phase error due to time alignment is:

$$\Delta\varphi_{a_r} = 2\pi \left(FE_r \cdot \Delta t + \frac{\Delta^2 t}{2} \cdot RFE_r \right). \tag{4.18}$$

In [52] it is noticed that the maximum FE and RFE values in the steady-state conditions reported in the Standard IEEE C37.118.1-2011 are too strict for *P-class* instruments and too loose for *M-class* PMUs. In fact, new and more sensible limits have been recently published in an Amendment to the same Standard [46]. In steady-state conditions (namely in the presence of off-nominal frequency deviations, harmonics and/or out-of-band interferers) the new FE and RFE upper bounds for *P-class* PMUs are 0.005 Hz and 0.4 Hz/s, respectively. In the case of *M-class* instruments instead, the scenario is more complex as the maximum FE values are 0.0025 Hz, 0.005 Hz, or 0.01 Hz depending on the considered testing condition, while the RFE limit is specified only in the off-nominal case (0.1 Hz/s). In dynamic conditions (particularly, when significant amplitude or phase modulations occur), depending on the PMU reporting rate, the FE and RFE limits lie in the following intervals: $[0.03, 0.06]$ Hz and $[0.6, 2.3]$ Hz/s, respectively, for a *P-class* PMU and $[0.12, 0.30]$ Hz and $[2.3, 14]$ Hz/s for an *M-class* PMU. By replacing the maximum values reported above in to (4.18) and noticing that the time misalignment Δt could be up to 70 ms for a *P-class* PMU, or up to 300 ms for an *M-class* PMU [52], it follows immediately that the worst-case phase errors $\varphi_{a_{max}}$ are:

- up to about 8 mrad in steady-state conditions and up to about 62 mrad in dynamic conditions when considering *P-class* PMUs;
- up to about 47 mrad in steady-state conditions and between about 350 mrad (fast reporting rates) to about 876 mrad (slow reporting rates) under the effect of modulations for *P-class* PMUs.

Thus, the time alignment uncertainty may quickly become the main contributor to the overall phase error.

4.6 Conclusion

In this chapter, a novel synchrophasor estimation algorithm based on a dynamic model is presented and analyzed in various steady-state and transient conditions. Several simulation results suggest that using a proper MSL window most of the *M-class* requirements of the Standard IEEE C37.118.1-2011 can be met using four-cycle observation intervals. The main uncertainty contribution affecting synchrophasor estimation accuracy are harmonics, wideband noise and out-of-band interferers. By increasing the observation interval duration, their impact decrease. However, the responsiveness in presence of amplitude or phase step changes and the estimation accuracy under the effect of amplitude or phase fluctuations degrade.

The second part of this chapter is focused on the phasor angle estimation accuracy of three different algorithms (i.e. the classic DFT-based algorithm, the Interpolated Dynamic DFT algorithm (IpD^{2}FT) and Taylor Weighted Least Square (TWLS)), with a special attention to the disturbances at the distribution level. Using a common set of window functions and observation intervals, it turns out that the classic DFT-based estimator is less sensitive to harmonics, out-of-band interferers, amplitude or phase steps. The IpD^{2}FT and TWLS estimators instead are particularly accurate in the presence of waveform amplitude and/or phase fluctuations. While the TWLS technique is globally slightly better in dynamic conditions, the IpD^{2}FT algorithm exhibits a lower sensitivity to steady-state disturbances, step-like changes and decaying DC offsets. Apparently, no estimator is able to provide best results in all situations. In addition, the accuracy of all the considered methods can be strongly affected by quick frequency or phase variations, as it may happen during transients. Finally, it is worth emphasizing that even though sampling and synchronization jitter have usually a minor impact on the overall phase error, possible time misalignments between the results returned by different PMUs (e.g. due to frequency and *ROCOF* limited measurement accuracy) could lead to intolerably large phase errors.

Chapter 5

State Estimation and Measurement Uncertainty Sensitivity

As known, electrical quantities, such as voltages, currents as well as active and reactive powers, have to be continuously monitored by system operators in order to use them for grid state estimation (SE). Currently, the SE requirements in terms of accuracy and responsiveness are changing as a result of smart grid evolution. In this context, the accurate measurement data coming from PMUs can substantially enhance SE and the corresponding applications. The purpose of this chapter is to review the definition, the properties and the sensitivity to measurement uncertainty of one of the most commonly used algorithms for SE, i.e. the Weighted Least Squares (WLS) technique. Even though the SE problem has been traditionally focused on transmission networks, currently and, even more in the future, distribution system state estimation (DSSE) is envisioned to become of primary importance for correct grid operation. In fact, the traditional sharp distinction between transmission and distribution networks (whose features were clearly different in the past) is expected to blur in grids where widespread micro-generation and dynamic load changes will bring about significant and time-varying bidirectional power flows [56]. Since the definition and the properties of WLS-based SE are basically the same in both contexts, a proper and general mathematical analysis of the sensitivity of this technique to different kinds of measurements is important to minimize their number, regardless of technology- or budget-related constraints. This problem is not totally new as it was already investigated some years ago [57]. For instance, [58] includes various analytical expressions that can be used to evaluate how measurement schemes, transmission line modeling, and other

---

Part of this chapter was published in

D. Macii, G. Barchi, D. Petri, "Uncertainty sensitivity analysis of WLS-based grid state estimators," *IEEE International Workshop on Applied Measurements for Power Systems Proceedings (AMPS), 2014*,vol., no., pp.1,6, 24-26 Sept.2014.

network parameters affect the goodness of a state estimate. However, this chapter will be specifically focused on the sensitivity analysis to measurement uncertainty, assuming that just a minimum amount of measurements is used to assure full state observability.

5.1 Introduction on SE

In the field of power systems, state estimation (SE) refers to the set of algorithms and techniques that combine measurement results, network topology, and network parameter values to determine the state of a grid at a given time [59]. Many management tasks like voltage regulation, stability monitoring, contingency analysis and dispatching, depend on knowledge of the state of the network. In the past, SE was mainly used at the transmission level, where the measurement data are collected through the network and provided by the SCADA system at a certain time. A typical SCADA system relies on quasi-steady state operative condition and it is unable to monitor fast transient phenomena. In the presence of dynamic events, such as load variations or topology changes, the measurements provided by SCADA can be affected by time skew due to the lack of synchronization, which can lead inaccurate estimates of the system state [7].

Various SE techniques exist and they can be roughly classified as static or dynamic [7]. The main difference between them is that in the dynamic case, the evolution of state variables over time is described by a dynamic system model based on a set of differential or finite difference equations. In particular, the definition of an internal model relaxes the need for measuring all the outputs of the system. In fact, a dynamic estimator, such as a Kalman Filter, relies partially on the internal system model to achieve observability and to track possible changes over time [60]. If no internal model are available, then just a static estimator can be used. In this case, the state of the networks can be observed only through *at least* so many independent measurements as the number of state variables. The main drawback of dynamic estimators is that they are more difficult to apply because they require good knowledge of the underlying model parameters. Moreover, the model has to be robust enough to be usable in a variety of conditions.

In this chapter and in the following only static state estimators will be considered. The most common used algorithm for SE is based on the Weighted Least Square (WLS) method. Various formulation of the WLS-based SE approach exist. In the most classic case the state variables are the magnitude and the angles of the nodal voltages; with the network being described by a single-phase model. The three-phase formulation of the same estimator is described in [61]. A dual SE approach where the state variables are the branch currents expressed in Cartesian coordinates is instead formalized in [62]. Two alternative formulations based on the same idea are reported in [63] and [64], respectively.

5.2 Measurement model and observability condition

Let us consider a network composed by N buses and B lines. Generally, the state of the network is modeled by $\boldsymbol{x} = [\boldsymbol{\theta}^T, \boldsymbol{V}^T]^T$ where $\boldsymbol{\theta}^T = [\theta_2, \theta_3, ..., \theta_N]^T$ is the vector of the voltage phasor angles at buses $2, ..., N$ (the phase of bus number 1 is usually taken as a reference, i.e. $\theta_1 = 0$) and $\boldsymbol{V}^T = [V_1, V_2, ..., V_N]^T$ is the vector of the N bus voltage magnitudes. In general, the state of the network can be observed through the well-known measurement model [59], i.e.

$$\tilde{\boldsymbol{z}} = \boldsymbol{h}(\boldsymbol{x}) + \boldsymbol{\varepsilon}_z = \begin{bmatrix} \boldsymbol{P}_{flow}(\boldsymbol{x}) \\ \boldsymbol{P}_{inj}(\boldsymbol{x}) \\ \boldsymbol{Q}_{flow}(\boldsymbol{x}) \\ \boldsymbol{Q}_{inj}(\boldsymbol{x}) \\ \boldsymbol{V}(\boldsymbol{x}) \\ \boldsymbol{\theta}(\boldsymbol{x}) \\ \boldsymbol{I}(\boldsymbol{x}) \\ \boldsymbol{\beta}(\boldsymbol{x}) \end{bmatrix} + \boldsymbol{\varepsilon}_z \tag{5.1}$$

where:

- $\boldsymbol{h}(\boldsymbol{x})$ is a nonlinear vector function of the state variables;
- $\boldsymbol{P}_{flow} = [P_{flow_1}, P_{flow_2}, \ldots, P_{flow_B}]^T$ and $\boldsymbol{Q}_{flow} = [Q_{flow_1}, Q_{flow_2}, \ldots, Q_{flow_B}]^T$ are the vectors of real and reactive power, respectively, flowing through network lines;
- $\boldsymbol{P}_{inj} = [P_{inj_1}, P_{inj_2}, \ldots, P_{inj_N}]^T$ and $\boldsymbol{Q}_{inj} = [Q_{inj_1}, Q_{inj_2}, \ldots, Q_{inj_N}]^T$ are the vectors of real and reactive power injected at bus $n = 1, \ldots, N$;
- $\boldsymbol{V} = [V_1, V_2, \ldots, V_N]^T$ and $\boldsymbol{\theta} = [\theta_2, \theta_3, \ldots, \theta_N]^T$ are identity functions of the state, i.e. $\boldsymbol{V}(\boldsymbol{x}) = \boldsymbol{V}$ and $\boldsymbol{\theta}(\boldsymbol{x}) = \boldsymbol{\theta}$;
- $\boldsymbol{I} = [I_1, I_2, \ldots, I_B]^T$ and $\boldsymbol{\beta} = [\beta_1, \beta_2, \ldots, \beta_B]^T$ are the magnitudes and the phases of the line currents;

Note that $\boldsymbol{\varepsilon}_z$ is a column vector including all measurement uncertainty contributions. In the following, we will refer to σ_i^2 as the variance associated with the ith measurement. It is worth emphasizing that $\boldsymbol{x}$ is a function of time, although the time variable is generally omitted to keep notation simpler.

The explicit expression of $\boldsymbol{P}_{flow}(\boldsymbol{x})$, $\boldsymbol{P}_{inj}(\boldsymbol{x})$, $\boldsymbol{Q}_{flow}(\boldsymbol{x})$, $\boldsymbol{Q}_{inj}(\boldsymbol{x})$, $\boldsymbol{I}(\boldsymbol{x})$, $\boldsymbol{\beta}(\boldsymbol{x})$ are widely available in the literature, e.g. in [59]. If we assume that each network branch is described

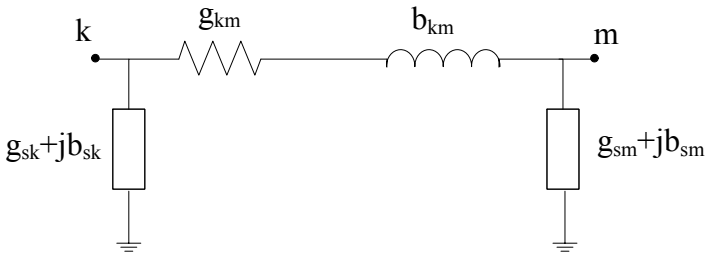

Figure 5.1: Two-port π-model of a network branch [59].

by the two-port π model shown in Fig. 5.1 and that $Y_{km} = G_{km} + B_{km}$ is the element (k, m) of the network bus admittance matrix, the following expressions hold [59]:

- the real and reactive power injection at bus k are

$$P_{inj_k} = V_k \sum_{m \in \mathcal{N}_k} V_m (G_{km} \cos\theta_{km} + B_{km} \sin\theta_{km}) \tag{5.2}$$

$$Q_{inj_k} = V_k \sum_{m \in \mathcal{N}_k} V_m (G_{km} \sin\theta_{km} - B_{km} \cos\theta_{km}); \tag{5.3}$$

- the real and reactive power flow from bus k to bus m are given by

$$P_{flow_{km}} = V_{km}^2 (g_{sk} + g_{km}) - V_k V_m (g_{km} \cos\theta_{km} + b_{km} \sin\theta_{km}) \tag{5.4}$$

$$Q_{flow_{km}} = -V_{km}^2 (b_{sk} + b_{km}) - V_k V_m (g_{km} \sin\theta_{km} - b_{km} \cos\theta_{km}); \tag{5.5}$$

- the real and imaginary part of the line current flow magnitude from bus k to bus m are defined as

$$\begin{aligned} I_{RE_{km}} &= V_k (g_{sk} + g_{km}) \cos\theta_k - V_k (b_{sk} + b_{km}) \sin\theta_k \\ &- V(m) g_{km} \cos\theta_m + V_m b_{km} \sin\theta_m; \end{aligned} \tag{5.6}$$

$$\begin{aligned} I_{IM_{km}} &= V_k (b_{sk} + b_{km}) \cos\theta_k + V_k (g_{sk} + g_{km}) \sin\theta_k \\ &- V_m b_{km} \cos\theta_m - V_m g_{km} \sin\theta_m; \end{aligned} \tag{5.7}$$

  Thus the magnitude and the angle of the corresponding branch current is simply given by:

$$I_{km} = \sqrt{I_{RE_{km}}^2 + I_{IM_{km}}^2} \tag{5.8}$$

$$\beta_{km} = \arctan\left(\frac{I_{IM_{km}}}{I_{RE_{km}}}\right); \tag{5.9}$$

In expression (5.2)-(5.9)
– V_k, θ_k are the voltage magnitude and phase angle at bus k, respectively;

– $\theta_{km} = \theta_k - \theta_m$;
– $g_{km} + jb_{km}$ is the admittance of the series branch connecting buses k and m;
– $g_{sk} + jb_{sk}$ is the admittance of the shunt branch connected at bus k;
– $\mathcal{N}_k$ is the set of bus numbers that are directly connected to bus k.

Note that (5.1) may consists of up to $M = 4N + 4B - 1$ equations, but in practice just a subset $M' \leq M$ of them is typically used to estimate the $2N - 1$ state variables. If the network internal dynamic is generally supposed to be negligible (i.e. the linearized system state matrix is a $2N-1 \times 2N-1$ identity matrix), then it can be easily proved from basic systems theory that the state of the network is observable if and only if the observability matrix associated with the linearized system around its state $\bar{\boldsymbol{x}} = \boldsymbol{x}(\bar{t})$ at a given time $\bar{t}$ has a full column rank. This is indeed possible if and only if $\text{rank}\{H(\bar{\boldsymbol{x}})\} = 2N-1$ where

$$H(\boldsymbol{x}) = \begin{bmatrix} \frac{\partial \boldsymbol{P}_{flow}}{\partial \boldsymbol{\theta}} & \frac{\partial \boldsymbol{P}_{flow}}{\partial \boldsymbol{V}} \\ \frac{\partial \boldsymbol{P}_{inj}}{\partial \boldsymbol{\theta}} & \frac{\partial \boldsymbol{P}_{inj}}{\partial \boldsymbol{V}} \\ \frac{\partial \boldsymbol{Q}_{flow}}{\partial \boldsymbol{\theta}} & \frac{\partial \boldsymbol{Q}_{flow}}{\partial \boldsymbol{V}} \\ \frac{\partial \boldsymbol{Q}_{inj}}{\partial \boldsymbol{\theta}} & \frac{\partial \boldsymbol{Q}_{inj}}{\partial \boldsymbol{V}} \\ \frac{\partial \boldsymbol{V}}{\partial \boldsymbol{\theta}} & \frac{\partial \boldsymbol{V}}{\partial \boldsymbol{V}} \\ \frac{\partial \boldsymbol{\theta}}{\partial \boldsymbol{\theta}} & \frac{\partial \boldsymbol{\theta}}{\partial \boldsymbol{V}} \\ \frac{\partial \boldsymbol{I}}{\partial \boldsymbol{\theta}} & \frac{\partial \boldsymbol{I}}{\partial \boldsymbol{V}} \\ \frac{\partial \boldsymbol{\beta}}{\partial \boldsymbol{\theta}} & \frac{\partial \boldsymbol{\beta}}{\partial \boldsymbol{V}} \end{bmatrix} \tag{5.10}$$

is the Jacobian of $\boldsymbol{h}(\boldsymbol{x})$. Therefore, at least $M' = 2N-1$ measurement equations of (5.1) with linearly independent coefficients in $H(\bar{\boldsymbol{x}})$ are needed to estimate $\bar{\boldsymbol{x}}$.

5.3 The WLS state estimator

The well-known WLS state estimator relies on the minimization of the cost function

$$J(\boldsymbol{x}) = [\tilde{\boldsymbol{z}} - \boldsymbol{h}(\boldsymbol{x})]^T R^{-1} [\tilde{\boldsymbol{z}} - \boldsymbol{h}(\boldsymbol{x})], \tag{5.11}$$

where R is the covariance matrix associated with the selected measurements. Usually, such contributions are assumed to be uncorrelated (i.e. $\mathbb{E}\{\varepsilon_{z_i}\varepsilon_{z_j}\} = 0$, $\forall i \neq j = 1, \ldots, M'$, where $\mathbb{E}\{\cdot\}$ denotes the expectation operator). Therefore, $R = \text{diag}(\sigma_1^2, \ldots, \sigma_{M'}^2)$. By computing the gradient of $J(x)$ and its Taylor series truncated to the first order around $\boldsymbol{x}_k$ for $k \geq 0$, the state at iteration $k+1$ can be obtained using the Gauss-Newton method, i.e. [59]

$$\boldsymbol{x}_{k+1} = \boldsymbol{x}_k + [H^T(\boldsymbol{x}_k) R^{-1} H(\boldsymbol{x}_k)]^{-1} H^T(\boldsymbol{x}_k) R^{-1} (\tilde{\boldsymbol{z}} - \boldsymbol{h}(\boldsymbol{x}_k)). \tag{5.12}$$

Observe that (5.12) converges to a solution if and only if $[H^T(\boldsymbol{x}_k)R^{-1}H(\boldsymbol{x}_k)]^{-1}$ is nonsingular, or, equivalently, if and only if $\text{rank}\{H(\boldsymbol{x}_k)\} = 2N - 1\ \forall k$, in accordance with the observability condition expressed in Section 5.2. Since, normally, at time t the iterative Gauss-Newton method is supposed to converge to the actual state $\boldsymbol{x}$, the WLS returns meaningful results if and only if $H(\boldsymbol{x})$ exhibits full column rank in a reasonably large neighborhood of $\boldsymbol{x}$. The flow chart of WLS algorithm is shown in Fig.5.2. However, it is well known that WLS method suffers from possible of convergence problems due to numerical instabilities, which may occur when R^{-1} is ill-conditioned or when virtual measurements (e.g. zero-power injection) exist. In such cases, the standard WLS methods can be modified by using the QR Chorlesky decomposition or the Lagrange multiplier techniques.

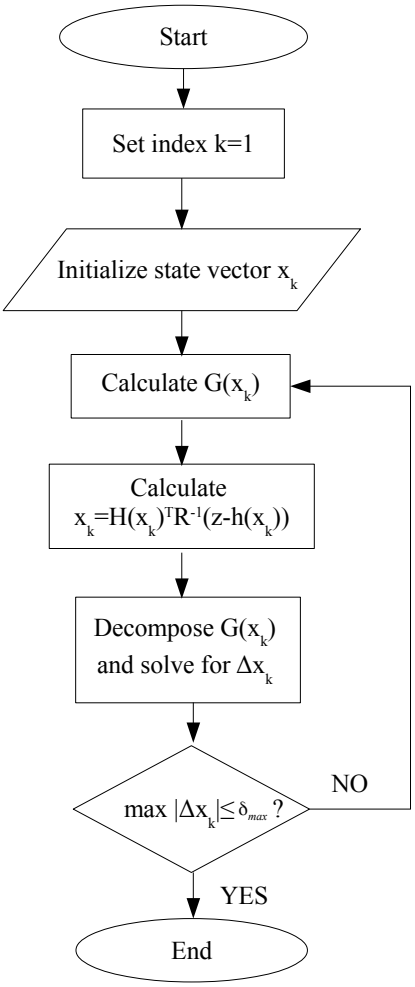

Figure 5.2: Flow chart of weighted least square method.

5.4 Uncertainty Sensitivity Analysis

If $\boldsymbol{\varepsilon}_z$ is the vector of uncertainty contributions related to the available $M' \geq 2N-1$ measurements, it follows immediately from (5.12) that the vector $\boldsymbol{\varepsilon}_x$ of the estimation errors associated to a generic state $\boldsymbol{x}$ results from

$$\boldsymbol{\varepsilon}_x = F(\boldsymbol{x})\boldsymbol{\varepsilon}_z \tag{5.13}$$

where $F(\boldsymbol{x}) = [H^T(\boldsymbol{x})R^{-1}H(\boldsymbol{x})]^{-1}H^T(\boldsymbol{x})R^{-1}$ can be referred to as *sensitivity matrix*, as it provides information about the effect of different measurements on the estimates of each state variable. The covariance matrix of the state estimates is simply given by:

$$\Phi_x = \mathbb{E}\{\boldsymbol{\varepsilon}_x \cdot \boldsymbol{\varepsilon}_x^T\} = F(\boldsymbol{x})\mathbb{E}\{\boldsymbol{\varepsilon}_z \cdot \boldsymbol{\varepsilon}_z^T\}F^T(\boldsymbol{x}) = F(\boldsymbol{x})RF^T(\boldsymbol{x}). \tag{5.14}$$

Observe that if just a minimum set of measurements $M' = 2N-1$ is used and if $\text{rank}\{H(\boldsymbol{x})\} = 2N-1$, then $F(\boldsymbol{x}) = H^{-1}(\boldsymbol{x})$, which is independent of R. Since R is a diagonal matrix comprising the absolute variances of the individual measured quantities, this can be rewritten as

$$R = ZR_r, \tag{5.15}$$

where:

- $Z = \text{diag}(z_1^2, z_2^2, \ldots, z_{M'}^2)$ is a diagonal matrix including the squared values of the electrical quantities that should be ideally observed if measurement uncertainty were negligible (i.e. when $\boldsymbol{\varepsilon}_z \approx 0$);
- $R_r = \text{diag}(\sigma_{r_1}^2, \sigma_{r_2}^2, \ldots, \sigma_{r_{M'}}^2)$ is the diagonal matrix built using the respective relative measurement uncertainties (except in the case of phase measurement, where the absolute uncertainty values are considered).

Thus, if $M' = 2N-1$, expression (5.14) can be also rewritten as

$$\Phi_x = H^{-1}(\boldsymbol{x})ZW_i{H^{-1}}^T(\boldsymbol{x})\sigma_{r_i}^2 = U_{F_i}\sigma_{r_i}^2 \tag{5.16}$$

where the weights of matrix $W_i = \text{diag}(\frac{\sigma_{r_1}^2}{\sigma_{r_i}^2}, \ldots, 1, \ldots, \frac{\sigma_{r_{M'}}^2}{\sigma_{r_i}^2})$ are the relative measurement uncertainties with respect to the ith one chosen as a reference. In essence, (5.16) highlights how the estimation uncertainty of each state variable depends on the uncertainty of the ith measurement.

If no a-priori information about measurement uncertainty is available, a reasonable approach to perform a global sensitivity analysis is to assume that $\sigma_{r_1} = \ldots = \sigma_{r_{2N-1}} = \sigma_r$. In this case, W_i is a $(2N-1)\times(2N-1)$ identity matrix and $U_{F_i} = U_F$ contains the increment rates of the elements of the covariance matrix Φ_x with respect to σ_r^2. Even if assuming

that all measurements are affected by the same uncertainty is not realistic in practice, this approach provides a fair indication of the sensitivity of state estimation to different kinds of measurements. As a result, some measurements could be included (or excluded) a priori in (from) a possible experimental setup.

Unfortunately, U_F consists of $(2N-1)\times(2N-1)$ values. Thus, even if it can be useful to analyze the uncertainty sensitivity of individual state variables, it does not provide a global overview of the sensitivity of the whole WLS state estimator to a generic set of $2N-1$ measurements. To this purpose, a scalar function combining all state estimation errors should be defined.

The individual estimator errors can be potentially expressed in terms of vectorial error, to take into account the joint effect of magnitude and phase estimation errors. With reference to bus $i = 1, \ldots, N$, the vector error associated to the ith bus voltage phasor is defined as

$$\begin{aligned} \varepsilon_{\mathrm{VE}_i} &= |(V_i + \varepsilon_{V_i})e^{j(\theta_i+\varepsilon_{\theta_i})} - V_i e^{j\theta_i}| \\ &= \sqrt{\varepsilon_{V_i}^2 + 2\,(V_i + \varepsilon_{V_i} V_i)\,(1 - \cos\varepsilon_{\theta_i})}, \end{aligned} \tag{5.17}$$

where ε_{θ_i} and ε_{V_i} are the phase and magnitude estimation errors. If the mean values of the estimation errors $\boldsymbol{\varepsilon}_\theta = [\varepsilon_{\theta_1}, \ldots, \varepsilon_{\theta_N}]^T$ and $\boldsymbol{\varepsilon}_V = [\varepsilon_{V_1}, \ldots, \varepsilon_{V_N}]^T$ are negligible, from a first-order Taylor series approximation of the square of (5.17) it can be easily shown that

$$\mathbb{E}\{\varepsilon_{\mathrm{VE}_i}^2\} \approx \mathbb{E}\{\varepsilon_{V_i}^2\} + V_i \mathbb{E}\{\varepsilon_{\theta_i}^2\} \quad i = 1, \ldots, N. \tag{5.18}$$

If the sensitivity matrix $F(\boldsymbol{x})$ is split into two $N \times M'$ matrices $[F_\theta^T(\boldsymbol{x}), F_V^T(\boldsymbol{x})]^T$ related to vectors $\boldsymbol{\theta}$ and $\boldsymbol{V}$, respectively, (with an all-zeros row added on top of $F_\theta(\boldsymbol{x})$ to take into account the state variable $\theta_1 = 0$) and if $\sigma_{r_1}{=}\ldots{=}\sigma_{r_{2N-1}}{=}\sigma_r$, it follows from (5.14) that

$$\begin{aligned} \mathbb{E}\{\boldsymbol{\varepsilon}_\theta \cdot \boldsymbol{\varepsilon}_\theta^T\} &= F_\theta(\boldsymbol{x}) Z F_\theta^T(\boldsymbol{x}) \sigma_r^2 {=} G_{\theta\theta}(\boldsymbol{x}) \sigma_r^2 \\ \mathbb{E}\{\boldsymbol{\varepsilon}_V \cdot \boldsymbol{\varepsilon}_V^T\} &= F_V(\boldsymbol{x}) Z F_V^T(\boldsymbol{x}) \sigma_r^2 {=} G_{VV}(\boldsymbol{x}) \sigma_r^2 \end{aligned} \tag{5.19}$$

Thus, we can define the following two global scalar performance parameters based on (5.18), i.e. the *root average mean square error*

$$RAMSE = \sqrt{\frac{1}{N}\sum_{i=1}^{N} \mathbb{E}\{\varepsilon_{\mathrm{VE}_i}^2\}} = S_A \sigma_r, \tag{5.20}$$

and the *root maximum mean square error*

$$RMMS = \sqrt{\max_{i=1,\ldots,N} \mathbb{E}\{\varepsilon_{\mathrm{VE}_i}^2\}} = S_M \sigma_r. \tag{5.21}$$

If $G_{VV_{ii}}(\boldsymbol{x})$ and $G_{\theta\theta_{ii}}(\boldsymbol{x})$ are the ith elements of the main diagonal of $G_{VV}(\boldsymbol{x})$ and $G_{\theta\theta}(\boldsymbol{x})$, respectively, it follows from (5.19) that

$$S_A = \sqrt{\frac{1}{N}\sum_{i=1}^{N}\left(G_{VV_{ii}}(\boldsymbol{x}) + V_i^2 G_{\theta\theta_{ii}}(\boldsymbol{x})\right)} \tag{5.22}$$

and

$$S_M = \sqrt{\max_{i=1,\ldots,N}\left(G_{VV_{ii}}(\boldsymbol{x}) + V_i^2 G_{\theta\theta_{ii}}(\boldsymbol{x})\right)}. \tag{5.23}$$

Expressions (5.22) and (5.23) provide the average and maximum measurement uncertainty sensitivity of the WLS state estimator to a given set of $2N-1$ measurements. In the following, we will refer to a measurement configuration or simply a configuration as any set of $M' = 2N-1$ measurements extracted from (5.1).

5.5 Uncertainty Sensitivity Optimization

In theory, the configuration characterized by i) a minimum amount of measurement points, ii) full state observability and iii) minimum worst-case sensitivity to measurement uncertainty, can be found by solving a constrained, nonlinear and combinatorial optimization problem. Let $\boldsymbol{\xi} = [\xi_1, \xi_2, \ldots, \xi_M]^T$ be a binary vector, whose ith element is set equal to 1 if the ith measurement is used for state estimation or 0 otherwise. As it is explained in Section 5.4, if $M' = 2N-1$ measurements are considered, then $F(\boldsymbol{x}) = H^{-1}(\boldsymbol{x})$. This condition can be equivalently expressed by defining the expanded matrix

$$F_e(\boldsymbol{\xi}, \boldsymbol{x}) = [H_e^T(\boldsymbol{x})\Xi H_e(\boldsymbol{x})]^{-1} H_e^T(\boldsymbol{x})\Xi \tag{5.24}$$

where $H_e(\boldsymbol{x})$ is the maximum-size Jacobian of (5.1), when all measurement equations are considered (i.e. when $M' = M$), and $\Xi = \mathrm{diag}(\boldsymbol{\xi})$ with $\mathbf{1}^T\boldsymbol{\xi} = 2N-1$. Notice that, as a result of the constraint $\mathbf{1}^T\boldsymbol{\xi} = 2N-1$, $F_e(\boldsymbol{\xi}, \boldsymbol{x})$ consists just of $2N-1$ nonzero columns. By splitting $F_e(\boldsymbol{\xi}, \boldsymbol{x})$ into $F_{e_\theta}(\boldsymbol{\xi}, \boldsymbol{x})$ and $F_{e_V}(\boldsymbol{\xi}, \boldsymbol{x})$, and by replacing such matrices and Z_e (i.e. Z for $M' = M$) into (5.19), then also (5.22) and (5.23) depend on $\boldsymbol{\xi}$ and can be regarded as possible cost functions that could be minimized to find the minimum average or maximum sensitivity to measurement uncertainty. Assuming for instance, that S_A chosen as a cost function (since it is continuous and generally differentiable), the general

optimization problem described above can be formalized as follows:

$$\begin{aligned} &\min_{\boldsymbol{\xi}} \mathrm{S}_A(\boldsymbol{\xi}) \\ &\\ &\text{(a) } \xi_i = \{0,1\} \quad i = 1,\ldots,M \\ &\text{(b) } \operatorname{rank}(H_e(\boldsymbol{x})\Xi) = 2N-1 \\ &\text{(c) } \mathbf{1}^T\boldsymbol{\xi} = 2N-1 \\ &\text{(d) } A\boldsymbol{\xi} \leq \mathbf{0} \\ &\text{(e) } D\boldsymbol{\xi} = \mathbf{0} \end{aligned} \tag{5.25}$$

where A is an $N \times M$ sparse matrix, whose element (n, j) is defined as follows:

$$A_{nj} = \begin{cases} -1 & (j{=}n{+}2B{+}2N{+}1 \text{ for } 1 \leq n \leq N{-}1) \ \vee \\ & (j = n{+}2B{+}3N \text{ for } N \leq n \leq N{+}B-1) \\ 1 & (j = n{+}2B{+}3N \text{ for } 1 \leq n \leq N{-}1) \ \vee \\ & (j = n{+}3B{+}3N \text{ for } N \leq n \leq N{+}B-1) \\ 0 & \text{otherwise} \end{cases} \tag{5.26}$$

$\mathbf{0}$ is an all-zero vector, and D is a sparse $(2B + N) \times M$ matrix whose element (n, j) is defined as follows

$$D_{nj} = \begin{cases} 1 & j{=}n \\ -1 & j{=}\, n{+}B{+}N \\ 0 & \text{otherwise.} \end{cases} \tag{5.27}$$

The rationale of the constraints (a)-(e) is shortly explained below. Constraint (a) is binary because we can just include (1) or not include (0) the ith measurement for $i = 1,\ldots,M$. However, we are interested in a minimum number of measurements assuring observability, i.e. $2N{-}1$. This leads to constraint (b). Unfortunately, not all combinations of $2N-1$ measurement equations may assure a full-rank Jacobian $H(\bar{\boldsymbol{x}})$. Thus, constraint (c) is needed to avoid incurring singular matrices when (5.18) is computed. The inequality linear constraint (d) is due to the fact that, when bus voltages or branch currents are considered, generally either just magnitude or both magnitude and phase (i.e. voltage or current phasors) are measured. Finally, the linear equality constraint (e) implies that the real and reactive power injected at a generic bus (or dually the real and reactive power flows in a branch) are always taken in pairs, since, in practice, these quantities are typically measured together by the same instrument.

It is worth emphasizing that a solution to (5.25) certainly exists because the number of

possible combinations is finite, but in general this solution could not be unique. Moreover, (5.25) is a NP-hard problem, because it is somehow related to the problem of finding the set of all $2N-1$ linearly independent rows of $H_e(\boldsymbol{x})$, whose cardinality is certainly smaller than $\binom{M}{2N-1}$, but, nonetheless, it grows exponentially with N.
In this involved scenario, a suboptimal solution to (5.25) can be found in a stochastic sense by applying the following algorithm, i.e.

- the constraint (a) can be initially relaxed (i.e. $\xi_i \in [0,1]$ for $i = (1,\ldots,M)$ to exploit the continuity and general differentiability of (5.22). Also, using fractional values of ξ_i has the equivalent effect of perturbing the elements of $H_e(\boldsymbol{x})$ around $\boldsymbol{x}$, which is beneficial to evaluate the numerical robustness of the ongoing optimization result. In fact, since the WLS estimation algorithm is iterative and relies on Jacobian values that generally fluctuate as the estimated state converges, by slightly changing the values of (5.24), possible configurations that could make $H_e^T(\cdot)\Xi H_e(\cdot)$ singular are more likely to be detected and removed from the optimization procedure.
- As a consequence of the relaxation of constraint (a), constraints (b) and (c) change as follows:

$$\begin{aligned} &\text{(b')}\ \operatorname{rank}(H_e(\boldsymbol{x})[\Xi]) = 2N-1 \\ &\text{(c')}\ \mathbf{1}^T[\boldsymbol{\xi}] = 2N-1 \end{aligned} \tag{5.28}$$

  where in (5.28) $[\cdot]$ denotes the rounding operator.
- Optimization is performed by combining a random search (RS) and a pattern search (PS) heuristic approaches. Both RS and PS can be used even when the gradient of the problem to be optimized is not available or when the cost function is not differentiable. Unfortunately, the PS approach may also easily lead to local optimal results [65], while pure RS solutions could suffer from long convergence times. Therefore, the PS is repeated each time starting from different randomly chosen feasible solutions (i.e. binary configurations meeting the given constrains). To improve the space exploration at every iteration $l \leq L$ of the PS based algorithm, the initial configuration is randomly chosen external to the hyperspheres that have been potentially explored during previous PS iterations. Such hyperspheres are centered in one of the previously used initial points and have a radius equal to the euclidean distance between such center points and the respective PS solution vector $\boldsymbol{\xi}_l$.
- After L iterations all optimal candidate solutions are compared and the best one is selected.

The values of L can be chosen with a trial-and-error approach so as to ensure a reasonable trade-off between level of confidence and convergence time.

5.6 Simulation results

The theoretical analysis Section 5.4 has been validated through simulations and has been used to investigate the uncertainty sensitivity of the WLS-based state estimator in a variety of conditions. All simulations have been performed in Matlab. The small grid chosen as a case study is the rural distribution network described in [66] and further analyzed in [67]. Fig. 5.3 shows the network that consists of 15 buses, 14 branches and a 11-kV feeder (node 1).

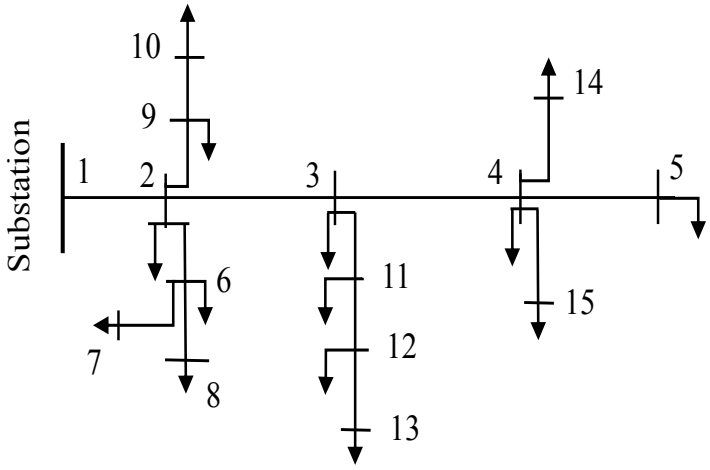

Figure 5.3: Small 15-node rural network [66].

The single-line network data and the nominal values of real and reactive power are summarized in Appendix A (Tab. A.1 and Tab. A.2 respectively). All loads are supposed to be affected by zero-mean random changes up to about $\pm 50\%$ of the nominal value, in accordance with the assumption reported in [67]. The power flow analysis of the network has been performed using the Matpower toolbox [68]. In particular, 500 values of bus voltage magnitude and phases (with respect to node 1) have been computed for real and reactive loads changing randomly as a function of time. In nominal load conditions such values simply coincide with those reported in [67]. More in general, every set of bus voltage magnitudes and angles resulting from the power flow analysis can be regarded as a snapshot of the actual state of the network at different time. In the case study considered, the maximum number M of measurement equations is 115, but just $M' = 2N - 1 = 29$ of them are needed in principle for state estimation.

In the first set of tests, the measurement configurations have been generated randomly, but with the same constraints described in Section 5.5, have been imposed to avoid situations that are manifestly meaningless.

For the sake of clarity these constraints are shortly recalled below:

1. real and reactive power injection measurements on a given bus are always included in pairs. In other words, if P_{inj_i} belongs to a configuration, then Q_{inj_i} must be also included in the same configuration, and vice versa;
2. real and reactive power flow measurements related to the same line are always included in pairs;
3. no voltage or current phase measurements alone can be included in a configuration. If a phase measurement belongs to a configuration, also the corresponding magnitude measurement is included in the same configuration (this is the case when PMUs are supposed to be used);
4. the chosen set of measurements must assure full state observability. This means that the rank of $H(\boldsymbol{x})$ in the neighborhood of the actual state $\bar{\boldsymbol{x}}$ at time $\bar{t}$ must be equal to $2N-1$, as explained in Section 5.2.

Using the constraints described above, 150 random configurations have been generated to estimate the state of the network. To assess the overall uncertainty sensitivity, in each simulation run the uncertainty of all measurements is constant and has been chosen between 0.1% and 10% for true measurements and between 10% and 50% for pseudo measurements. It is worth emphasizing that the purpose of these Monte Carlo simulations is just to validate the theoretical analysis described in Section 5.4 in multiple conditions. Once the differences between the state values resulting from the power flow analysis and the state estimates associated with each configuration are computed, at first the $RAMSE$ and $RMMSE$ values are calculated as a function of σ_r. Then, the average slope coefficients of such functions (namely the simulated values of S_A and S_M) are compared with the theoretical results based on (5.22) and (5.23). Fig.5.4(a)-(b) shows the simulated (solid lines) and theoretical (dotted lines) values of S_A and S_M, respectively. To improve visualization, data are sorted in ascending order and a few outliers (whose sensitivity was particularly large) have been removed. Clearly, in both plots the theoretical and simulated sensitivity coefficients are very close, regardless of the configuration considered. This confirms the correctness of the proposed analysis. The practical usefulness of (5.20)-(5.23) is threefold.

First of all,(5.20) and (5.21) can be used to predict the overall state estimation uncertainty, once the nominal values of loads, network parameters and σ_r are given. If the individual measurement uncertainties σ_{r_i} for $i = 1, \ldots, 2N-1$ differ significantly from one another, then $RAMSE$ and $RMMSE$ can be estimated numerically from (5.18), provided that the elements of W_i in (5.16) are known. If such coefficients are not available, the worst-case $RAMSE$ or $RMMSE$ values can be obtained by setting

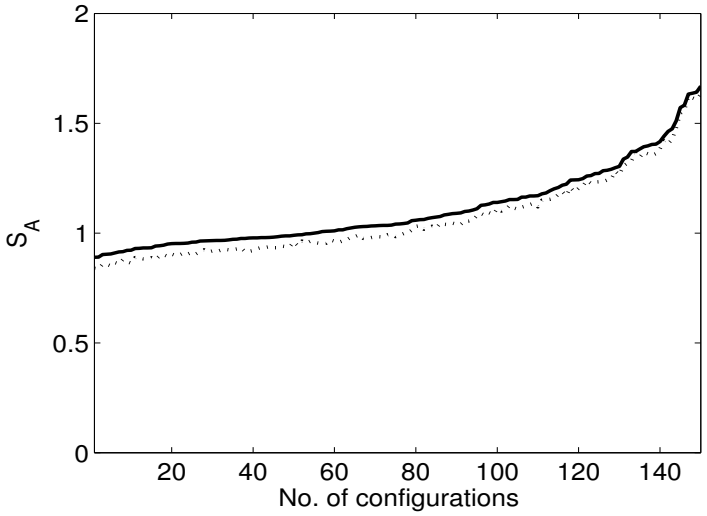

(a)

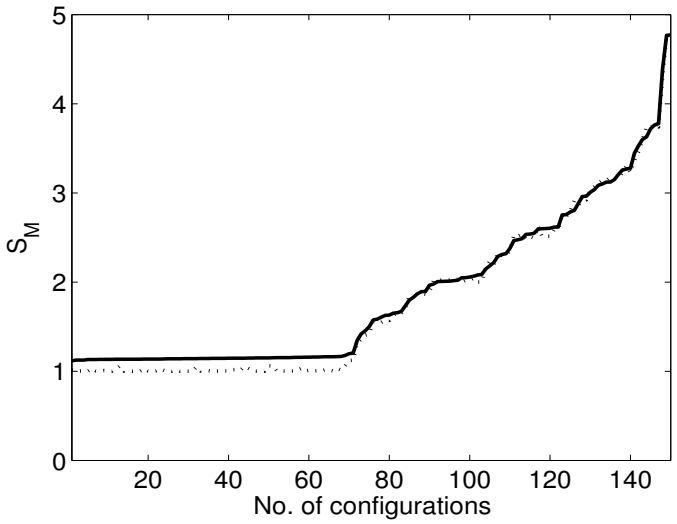

(b)

Figure 5.4: Comparison between simulated (solid lines) and theoretical (dotted lines) average (a) and maximum (b) global sensitivity coefficients for 150 random configurations consisting of $2N-1$ measurements assuring full state observability. To improve readability the sensitivity coefficients have been sorted in ascending order.

$\sigma_r = \max_{i=1,\ldots,2N-1}\{\sigma_{r_i}\}$. Another potential use of (5.22) and (5.23) is related to the possibility to infer quickly (i.e. without running long simulations) the values of σ_r that can assure given estimation accuracy requirements. An example of this type of application is reported in Fig. 5.5, which shows the values of $RMMSE$ of three different configurations as a function of σ_r. *Configuration A* (solid line) refers to the case of real and

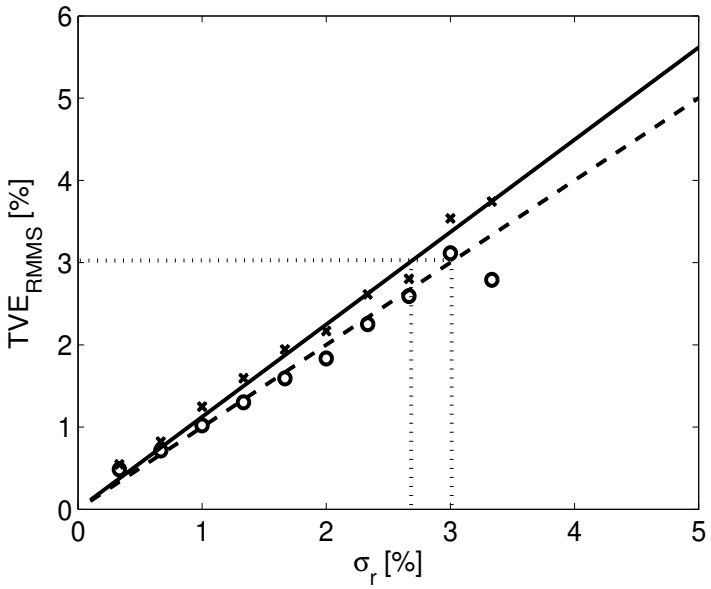

Figure 5.5: Theoretical root maximum mean square error values as a function of σ_r in 3 cases, i.e. using 14 real and reactive power injection measurements plus one voltage magnitude measurement (*Configuration A* - solid line); using voltage phasor measurements only (*Configuration B* - dashed line) and, finally, using 5 real and reactive power flow measurements, 1 voltage magnitude, 2 voltage phasors and 6 current phasor measurements (*Configuration C* - dash-dotted line). Cross-, circle- and plus-shaped markers refer to the respective results of classic WLS-based estimation.

reactive power injection measurements at buses $i = 2, \ldots, 15$, plus an additional voltage magnitude measurement at bus 1. *Configuration B* (dashed line) is obtained assuming to measure nodal voltage phasors only. *Configuration C* (dash-dotted line) consists of a variety of measurements, i.e. real and reactive power flows over lines 2, 4, 8, 10, 11, voltage magnitude at bus 7, phasors of voltages at nodes 13 and 14 and, finally, phasors of currents over lines 5, 6, 7, 9, 13 and 14. In all cases, the theoretical lines approximate (and extrapolate) very well the values of $RMMSE$ obtained numerically with the WLS estimator (highlighted by cross-, circle- and plus-shaped markers for *configuration A*, *B* and *C*, respectively). Observe that if, for instance, the worst-case error boundary is set equal to 0.02 p.u. (dotted horizontal line), the relative uncertainty of different groups of measurements should not exceed 1.8% for *configuration A*, 2% for *configuration B* and 0.65% for *configuration C*. Obviously, when sensitivity is higher, relative measurement uncertainty has to be decreased accordingly to keep the estimation error within the wanted boundaries.

Finally, either (5.22) or (5.23) can be used as cost functions of the constrained and nonlinear optimization problem formalized in Section 5.5. The stems in Fig. 5.6 represent the frequencies of occurrence of the various types of measurements over $L = 200$ solutions

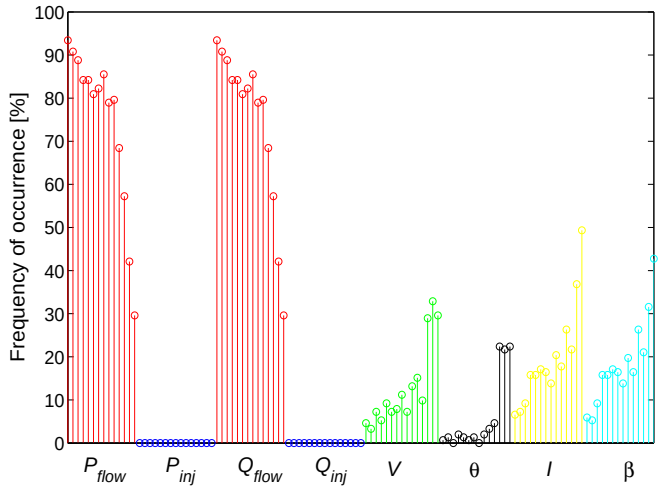

Figure 5.6: Frequency of occurrence of different kinds of measurements over $L = 200$ results of the random search algorithm minimizing S_A in the considered case study.

of the PS-based heuristic optimization algorithm described in Section 5.5 when it is applied to the network in Fig. 5.3. Observe that different kinds of measurements are grouped into homogeneous categories highlighted by different colors. Within each group the ith stem refers either to the ith bus (with $i = 1, ..., 15$ of nodal measurements) or to the ith line (with $i = 1, ..., 14$ for line measurements). Notice that in the specific case under analysis, there are some measurements that have never been included in any potential solution (e.g. $\boldsymbol{P}_{inj}$ and $\boldsymbol{Q}_{inj}$). Clearly, this means that such measurements are unlikely to minimize S_A. On the contrary in the current example the measurements with the highest probabilities to minimize S_A refer to: the real and reactive power flows over lines $1-12$ in Tab.A1. By adding also the voltage magnitude measurement at bus 13 and the current phasors (i.e. magnitude and phase) of lines 13 and 14, the best configurations is finally determined. This is characterized by $S_A = 0.94$. It is worth noticing that many other configurations with comparable uncertainty sensitivity (i.e. with S_A ranging between 0.9 and 1.2) exist. So we cannot ensure that the solutions obtained with the proposed algorithm is the global optimum. However, it is certainly slightly suboptimal with a level of confidence that increases as the number of iterations L grows.

5.7 Conclusion

State estimation is a well-known problem that is particularly and increasingly critical for future energy grids. Besides the traditional issues concerning with accuracy and numerical robustness, fine-grained network observability and scalability are difficult to address as

the number of measurements and the amount of data to be processed grows.

In this chapter, the classic Weighted Least Square (WLS) state estimator has been reviewed to point out to what extent results are affected by measurement uncertainty when a minimum number of measurements able to assure full observability is used. The proposed theoretical analysis provides a straightforward criterion to predict the overall worst-case state estimation accuracy or, dually, to establish the maximum measurement uncertainty able to keep the average or worst-case estimation accuracy within given boundaries. The sensitivity coefficients could be also used as cost functions of an optimization problem to determine what types of measurements are most likely to minimize the overall average or maximum growth rate of the mean square estimation errors.

The results of the optimization procedure in a simple case study show quite interestingly, that the use of PMUs, even if generally recommended to improve accuracy and observability does not necessarily minimize the sensitivity to measurement uncertainty. Indeed, if measurement uncertainty values are comparable, a suitable mixture of PMU-based and other measurements can further improve estimation accuracy. Some additional research efforts are currently ongoing to analyze the uncertainty sensitivity when measurements with different levels of accuracy and precision (e.g. true and pseudo-measurements) are combined together.

Chapter 6

Role of PMU in Distribution System State Estimation

The purpose of this chapter is to analyze the role and the impact of PMUs in Distribution System State Estimation (DSSE) under the assumption that network observability is guaranteed. At first the classic Weighted Least Square (WLS) algorithm is considered and a simple algorithm based on a greedy approach is used to evaluate the impact of a growing number of PMUs on state estimation accuracy. Afterwards, a Bayesian linear state estimator (BLSE) based on a fully linear approximation of the power flow equations is proposed and its performances are analyzed and compared with those of WLS estimator. In both cases the simulation results show that deploying few, but accurate, PMUs generally provide better performance than using a larger number of less accurate instruments, thus shedding some light on possible trade-offs between number, accuracy and cost of PMUs.

6.1 PMUs and State Estimation: an overview

As shown in Chapter 5, SE generally relies on the solution of a non-linear optimization problem that has multiple local minima, is computationally expensive and may suffer from numeral problems. Although there is a well-established tradition and an extensive literature on SE for transmission networks, only recently the SE problem has been taken into

Parts of this Chapter were published in

D. Macii, G. Barchi, L. Schenato, "On the Role of Phasor Measurement Units for Distribution System State Estimation," *IEEE Workshop on Environmental Energy and Structural Monitoring Systems (EESMS) 2014* , vol., no., pp.1,6, 17-18 Sept. 2014.

L. Schenato, G. Barchi, D. Macii, R. Arghandeh, K. Poolla, A. Von Meier; "Bayesian Linear State Estimation using Smart Meters and PMUs Measurements in Distribution Grids" *Proceeding of IEEE International Conference on Smart Grid Communications (SmartGirdComm14)* Nov. 2014.

consideration at the distribution level [61]. Primarily, this is because measurement data in distribution networks tend to be very scarce and often nonexistent beyond the substations. Moreover, transmission and distribution networks generally have different features. The former ones transfer large amounts of power and are characterized by mesh topologies, high line reactance-resistance (X/R) ratios and a quite limited number of lines and buses. On the contrary, distribution systems typically transfer limited amounts of power, exhibit a radial topology consisting of many nodes with low X/R values and unbalanced loads. These circumstances have changed in recent years, due to the increasing penetration of distributed energy resources, which may introduce variability, uncertainty and even instabilities. Consequently, there is a growing interest in Distribution System State Estimation methods based on the joint use of pseudo-measurements and measurements from PMUs possibly using cheaper instrument than those available nowadays [49, 73]. Currently, one of the main state estimation methods also for DSSE is the same WLS-based algorithm, described in Chapter 5. However, to correctly capture the dynamic phenomena that characterize the distribution level some SE solutions rely explicitly on three-phase branch currents [74, 63], linearized models for pseudo-measurements [75], or unsynchronised phasor measurements [76]. The introduction of PMUs has increased the accuracy of SE algorithms, by measuring not only magnitudes, but also phase angle differences between voltages phasors at different nodes [69]. As explained in Chapter 5, a system is observable if at least so many independent measurements as the number of state variables are used. This suggests that a PMU should be used in each node of the network. Unfortunately, for economic and technical constraints, this is not feasible. Thus, the best solution is to combine traditional and PMU measurements. The inclusion of PMUs in state estimation creates two critical problems [7]:

- how to combine traditional and PMU measurements;
- how to place the PMUs in the network in order to maximize observability and performances.

The first issue can be tackled in two possible ways, as discussed in [70]. In the first one, the PMU data can be combined with those resulting from traditional measurements in a single stage (it is also the method used in current and in the previous chapter). Alternatively, a two-stage scheme can be used to improve the state estimated from traditional measurement equipment, e.g. by applying a post-processing step based on PMU phasor data. Both approaches can reach the same accuracy, and the best practice depends on the particular scenario.

The optimal PMU Placement (OPP) problem is a constrained optimization problem that aims at minimizing the number of devices while ensuring observability and given uncertainty boundaries. Alternatively, we can maximize the estimation accuracy when

a maximum number of PMUs is available. The literature proposes several algorithms to solve this problem and a comprehensive review is presented in [71].This problem can been tackled in several different ways, e.g. using genetic algorithms, particle swarm optimization (PSO), integer programming or binary search. For instance, in [72] a genetic algorithm for joint PMUs and smart meters optimal placement is described in the specific context of distribution networks.

6.2 Impact of PMUs on WLS-based State Estimators

In the specific context of distribution networks, the most commonly used instruments are: smart meters and PMUs [72]. Assuming that only active and reactive power injection data are available and that the PMUs are used to measure either nodal voltage phasors or branch current phasors, it follows that the general measurement model described by equation (5.1) can be simplified as follows:

$$\tilde{\boldsymbol{z}} = \boldsymbol{h}(\boldsymbol{x}) = \begin{bmatrix} \boldsymbol{P}(\boldsymbol{x}) \\ \boldsymbol{Q}(\boldsymbol{x}) \\ \boldsymbol{V}(\boldsymbol{x}) \\ \boldsymbol{\theta}(\boldsymbol{x}) \end{bmatrix} + \varepsilon_z \quad \text{or} \quad \tilde{\boldsymbol{z}} = \boldsymbol{h}(\boldsymbol{x}) = \begin{bmatrix} \boldsymbol{P}(\boldsymbol{x}) \\ \boldsymbol{Q}(\boldsymbol{x}) \\ \boldsymbol{I}(\boldsymbol{x}) \\ \boldsymbol{\beta}(\boldsymbol{x}) \end{bmatrix} + \varepsilon_z \tag{6.1}$$

where the meaning of the various quantities is the same as described in Section 5.2. Consider that, for the sake of simplicity, in (6.1) $\boldsymbol{P}(\boldsymbol{x})$ and $\boldsymbol{Q}(\boldsymbol{x})$ refer just to $\boldsymbol{P}_{inj}(\boldsymbol{x})$ and $\boldsymbol{Q}_{inj}(\boldsymbol{x})$ respectively, since no power flow measurements will be considered in the following. Again, a necessary condition to leave full system observability is that the total number of available measurements is larger than $2N - 1$.

6.2.1 A PMU placement strategy

If P PMUs are available for state estimation, a relevant problem is where to place them to achieve best accuracy. If the cost function is the $RAMSE$ defined in (5.20), then the placement problem can be formalized as follows:

$$\begin{aligned} \mathcal{M}^{op}(P) &:= \arg\min_{\mathcal{M}} RAMSE(\mathcal{M}) \qquad (6.2) \\ s.t. \quad & |\mathcal{M}| = K \\ RAMSE^{op}(P) &:= RAMSE(\mathcal{M}^{op}(P)) \qquad (6.3) \end{aligned}$$

where $RAMSE^{op}(P)$ is the minimum value of (5.20), which is achieved when the optimal set $\mathcal{M}^{op}(P)$ of P PMUs is used. Obviously, $RAMSE^{op}(P)$ is a monotonically non-increasing function of the number of PMUs, i.e. $RAMSE^{op}(P) \geq RAMSE^{op}(P+1)$.

Observe that (6.2) is a combinatorial problem; so its solution is NP-hard and maybe unfeasible when large grids are considered. This is the reason why heuristic approaches based on genetic algorithms or PSO are frequently used for placement [77].

However, in this chapter our main purpose is just to analyze the impact of a growing number of PMUs on state estimation accuracy. Therefore, a simple greedy PMU placement procedure, based on the addition of one PMU at a time, is sufficient to evaluate the best local performance improvement. The algorithm (formally described in the following inset) is computationally more tractable than the original problem, as it requires at most $\frac{N(N-1)}{2}$ iterations to find a set of PMU positions. However, if we denote with $\mathcal{M}^{gr}(P)$ as the set of K locations resulting from the application of the greedy algorithm, the optimality of this solution is guaranteed only when $P = 0, 1$ or N, whereas in general $RAMSE^{gr}(P) = RAMSE(\mathcal{M}^{gr}(P)) \geq RAMSE^{op}(P)$, $\forall P = 2, \ldots, N-1$.

Algorithm 1 The greedy PMU placement algorithm

Require: Φ_x

1: $\mathcal{M}^{gr}(0) := \emptyset, \overline{\mathcal{M}}(0) := \{2, \ldots, N\}$
2: **for** $\tau = 1$ to N **do**
3: $\quad k(\tau) = \arg\min_{k \in \overline{\mathcal{M}}(\tau-1)} RAMSE(\mathcal{M}^{gr}(\tau-1) \cup k)$
4: $\quad \mathcal{M}^{gr}(\tau) = \mathcal{M}^{gr}(\tau-1) \cup k(\tau)$
5: $\quad \overline{\mathcal{M}}(\tau) = \overline{\mathcal{M}}(\tau-1) \setminus k(\tau)$
6: $\quad RAMSE^{gr}(\tau) = RAMSE(\mathcal{M}^{gr}(\tau))$
7: **end for**

6.2.2 Simulation Results

The impact of PMUs on state estimation has been analyzed in a simple case study based on the IEEE 33-bus distribution radial network [78].

The feeder of the network is at bus 1. This is also the reference node for phasor angle estimation (i.e. $\theta_1 = 0$). The topology of the network is shown in Fig. 6.1. The line parameters and its nominal load values, expressed in terms of active and reactive powers are reported in Tab. A.3 and Tab. A.4 respectively.

In real scenarios, the actual load profiles may change significantly over time. To a first approximation, the statistical distribution of such profiles over reasonably long time intervals is generally regarded as normal. However, recent studies showed that a Gaussian mixture model (GMM) better fits experimental data [79]. In the developed simulator, the load profiles can be generated randomly as a function of time on the basis of different stochastic models (i.e. uniform, Gaussian or GMM with different variance and mean values on each node). For any given power profile, at first the active and reactive power

produced by the generator(s) is computed. Then, a full power flow analysis is performed using the Matpower toolbox [68]. In this way, the actual phasors of nodal voltages and branch currents at a given time are obtained. The magnitude and the phase of such nodal voltages are then compared with the results of the WLS algorithm based on different sets of measurements to evaluate estimation accuracy in various conditions. Two inputs common to all simulations are:

- the nominal values of all active and reactive loads (i.e. pseudo-measurements with uncertainty in the order of 30%-50%), which provide the full grid observability,
- the magnitude of bus 1 voltage measured with 0.3% standard relative uncertainty.

The PMU accuracy, expressed in terms of TVE, is assumed to lie in the interval $[0.1\%, 1\%]$. The lower end of this interval is compatible with the specifications of several high-performance instruments available on the market (e.g., the 1133A PMU by Arbiter Systems). The upper end instead is the worst-case limit in most of the operating conditions reported in the Standard C37.118.1-2011 [18].

Fig. 6.2 shows the $RAMSE$ values as a function of the number of deployed PMUs. Such values result from 300 state estimates for each set of measurements. The load profiles are generated using GMM distributions resulting from the superimposition of up to 4 Gaussian curves. The mean values of each active or reactive load are within $\pm 10\%$ of the nominal data reported in Appendix A Tab. A.4. The corresponding standard deviations are equal to 33% of the nominal values. The respective variances are used as

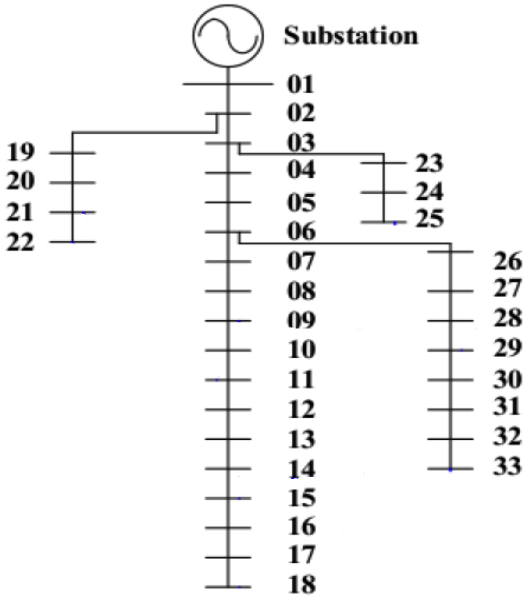

Figure 6.1: IEEE 33 node distribution network

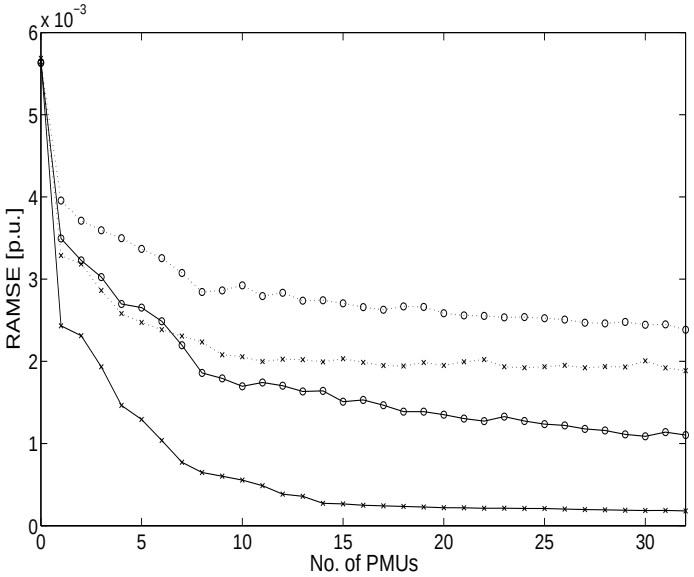

Figure 6.2: $RAMSE$ values as a function of the number of PMU measurements. The solid lines refer to the results achieved when both nodal voltage magnitudes and phases are measured, the dashed lines are obtained assuming that only the respective voltage magnitudes are available. The worst-case PMU TVE is assumed to be either 0.1% (cross markers) or 1% (circle markers).

weights of the pseudo-measurements in (5.11).

In Fig. 6.2, the PMUs are supposed to measure voltage magnitudes and phases directly with two different accuracies, i.e. 0.1% (solid lines with cross markers) and 1% (solid lines with circle markers). The PMUs are placed sequentially (one by one) in the order provided by the greedy algorithm described in Section 6.2.1. Generally, this order may change as a function of measurement uncertainty. The results of PMU-based state estimation are also compared with those obtained using voltage magnitudes only (dotted lines with cross and circle markers for 0.1% and 1% markers, respectively).
The curves in Fig. 6.3 represent the $RAMSE$ values as a function of the number of PMUs when they measure the currents of branch phasors instead of the state variables directly (solid lines). Load profiles, instrumental accuracy and placement strategy are the same as those used to plot Fig.6.2. Again, the results of PMU-based state estimation are compared with those obtained using current magnitudes only (dotted lines). The results shown in Figs. 6.2 and 6.3 (as well as other similar results based on other distribution networks and not reported here for the sake of brevity) suggest the following interesting remarks.

1. As expected, measuring voltage or current phasors can considerably improve state estimation accuracy compared to the case when magnitudes only are measured. This emphasizes the importance of phase data, especially at the distribution level [48],

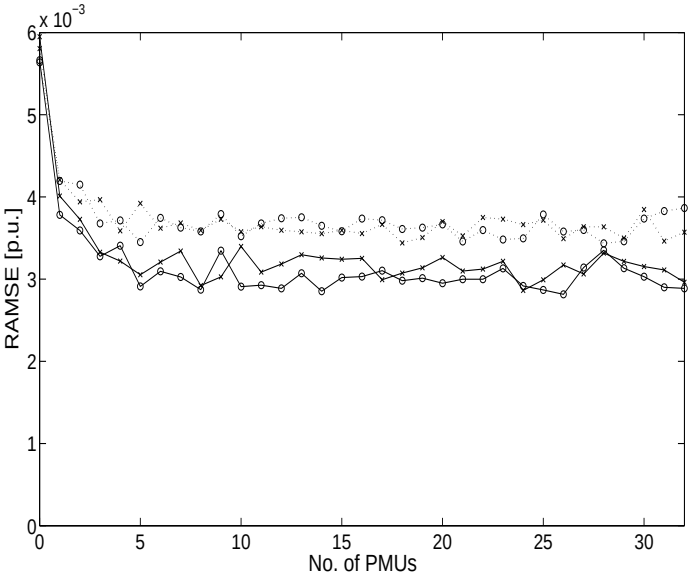

Figure 6.3: $RAMSE$ values as a function of the number of PMU measurements.The solid lines refer to the results achieved when both branch current magnitudes and phases are measured, the dashed lines are obtained assuming that only the respective current magnitudes are available. The worst-case PMU TVE is assumed to be 0.1% either (cross markers) or 1% (circle markers).

even when angle differences are very small.

2. The impact of PMU uncertainty on estimation accuracy is relevant when the state variables (i.e. voltage magnitudes and angles) are measured directly. However, when they are derived indirectly from current phasors, the influence of instrumental uncertainty is less noticeable. This is maybe due to the approximation errors in linearizing functions $I(x)$ and $\beta(x)$ in (6.1). In fact, linearization errors can be comparable or even larger than measurement uncertainty.
3. While a few PMUs can considerably improve estimation accuracy, the law of diminishing returns clearly holds in the considered scenarios. As a rule of thumb, installing PMUs with the same accuracy in more than about 1/3 of nodes or branches is unnecessarily expensive, as no significant performance improvements are achieved. This behavior is independent of the PMU placement sequence, although the $RAMSE$ values change as a function of the placement strategy.
4. Further simulations confirm that the qualitative behavior described above is independent of both the load profile stochastic model and the variance of loads, although numerical results and placement sequence generally change from case to case.

Fig. 6.4 shows more clearly the relationship between root average mean square estimation error and PMU accuracy (also expressed in terms of maximum TVE) when voltage

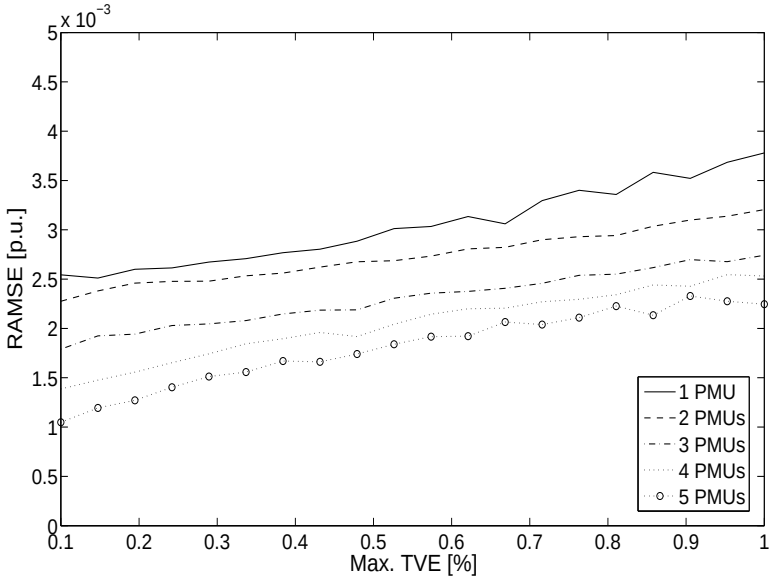

Figure 6.4: $RAMSE$ values as a function of PMU accuracy (also expressed in terms of TVE), when 1, 2, 3, 4 or 5 PMUs are used to measure voltage phasors.

phasors are measured. Every $RAMSE$ value results from 500 estimates. Observe that the overall estimation accuracy depends almost linearly on PMU worst-case instrumental uncertainty, but the growth rate is quite independent of the number of PMUs. It is worth emphasizing that a given target estimation accuracy could be reached using either a few high-performance PMUs or a larger number of less accurate instruments. Thus, the best solution essentially depends on the relationship between cost and accuracy of different classes of PMUs. In the present example, the slowly growing trend intuitively suggests that using a minimal number of high-performance instruments is probably the best choice. However, further analyses and a proper cost quantification are needed to draw ultimate conclusions. The robustness of state estimation to possible changes of loads and line parameters as a function of the number of PMUs has been also evaluated. Similar analyses, but in different conditions and with different performance metrics, are already available in the literature, e.g. in [80]. In our case, several Monte Carlo simulations have been performed assuming that line resistances and reactances are affected by uniformly distributed tolerances within $\pm 5\%$, $\pm 10\%$, $\pm 15\%$ and $\pm 20\%$ of the respective nominal values shown in Tab. A.3. In particular, 100 realizations of network parameters have been generated in each case. For every realization two different power flow analyses have been performed: the first one in nominal conditions (i.e. assuming that loads are constant and equal to those reported in Tab. A.4) and the second one using the same GMM load profiles adopted in previous simulations. In each scenario the state of the network has

been estimated using pseudo-measurements and PMUs with 1% max TVE. No more than 15 PMUs have been used because, as explained above, results do not change significantly when the number of PMUs grows further.

Fig. 6.5(a)-(b) shows the box-and-whisker plots of the $RAMSE$ values as a function of the number of PMUs when the tolerance of the line parameters is 20% (the values obtained with tolerances of 5%, 10%, 15% exhibit slightly smaller variances; so they are not reported because they are not particularly meaningful). Fig. 6.5(a) refers to the nominal load case. Fig. 6.5(b) reports the results of the GMM load model. The plots show that the effect of different load profiles is noticeable only when no PMUs are used. In all the other cases, the estimation results when the GMM load model is used are just slightly worse than those in nominal load conditions. Observe that the impact of line parameters variations on state estimation is not particularly relevant and it is approximately the same in both Fig. 6.5(a) and 6.5(b). In fact, the maximum dispersion of the $RAMSE$ values is always smaller than $\pm 0.1\%$ and it tends to decrease further when the number of PMUs grows. Therefore, if enough PMUs are deployed, the impact of line parameter tolerances is negligible regardless of the load profile.

6.3 An alternative approach for power flow analysis and state estimation

The contribution of the rest of this chapter is twofold. First, a Bayesian linear state estimator (BLSE) based on a fully linear approximation of the power flow equations is presented. Secondly an evaluation of the performances of this estimator with respect to the classic WLS techniques are presented. In particular, it is shown, via numerical Monte Carlo simulations on the same IEEE 33-node distribution grid that, under some assumption, the BLSE offers the same performance as the WLS state estimator, but with the benefit of being numerically faster and more robust.

6.3.1 Grid model description

Starting from the notation used in [81, 82], a grid can be modelled as a graph $\mathcal{G} = \{\mathcal{V}, \mathcal{E}\}$ where $\mathcal{V} = \{1, \ldots, N\}$ is the set of nodes or buses and $\mathcal{E} = \{1, 2, \ldots, B\}$ is the ordered set of the lines of the grid. Each edge ℓ is represented by the ℓ-th row of the incidence matrix $A \in \{-1, 0, 1\}^{B \times N}$ where all elements are zeros except for one entry set to -1 (source node) and another entry set to 1 (terminal node). The impedance matrix $Z \in \mathbb{C}^{B \times B}$ is a diagonal complex matrix given by $Z = \text{diag}\{z_1, \ldots, z_B\}$, where z_ℓ is the impedance of the ℓ-th line. Without loss of generality we will assume that the node 1 correspond

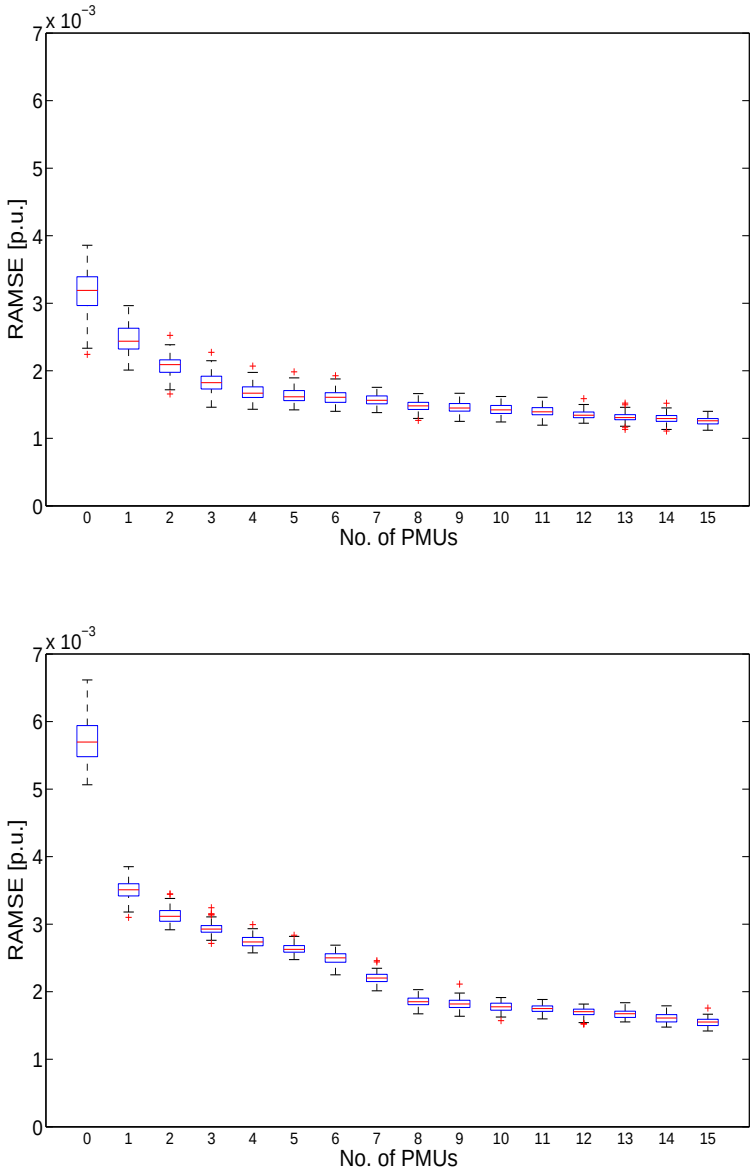

Figure 6.5: Box-and-whisker plots of the root average mean square error (RAMSE) as a function of the number PMUs, in (a) nominal load conditions and (b) in the case of GMM loads with a standard deviation equal to 33% of the nominal value. In all cases the worst-case PMU accuracy is 1%.

to the substation or point where the distribution network under analysis is connected to the main grid. Let $v_1, v_2, \ldots, v_N \in \mathbb{C}$ and $i_1, \ldots, i_N \in \mathbb{C}$ be the vectors representing the phasors of bus voltages and of the injected current, respectively. The symbol i_k represents the phasor of the current injected into the k-th node. We also denote with $c_1, \ldots, c_B \in \mathbb{C}$ the phasors of the currents flowing across the ℓ-th line from the source node to the sink node defined by the ℓ-th row of the incidence matrix A. Let us define the complex column vectors $v^+ = [v_1 \ \ldots \ v_N]^T \in \mathbb{C}^N$, $i^+ = [i \ \ldots \ i_N]^T \in \mathbb{C}^N$, and $c = [c_1 \ \ldots \ c_B]^T \in \mathbb{C}^B$. The Kirchhoff's laws at all nodes and lines of the grid can be compactly written as:

$$A^T c + i^+ = 0 \ (KCL), \tag{6.4}$$

$$Av^+ + Zc = 0 \ (KVL) \tag{6.5}$$

Since Z is invertible we can combine the previous two equations into a single matrix expression that relates voltage and current phasors at each node of the grid:

$$L^+ v^+ = i^+, \quad L^+ := A^T Z^{-1} A \tag{6.6}$$

where $L^+ \in \mathbb{C}^{N \times N}$ is referred to as the admittance matrix of the grid. We assume that the node representing the feeder acts as an ideal voltage source generator, i.e.

$$v_1 = V_1 \tag{6.7}$$

where $V_1 \in \mathbb{R}$ is the nominal voltage at the PCC. The previous expression implies that $|v_1| = V_1$ and $\angle v_1 = \theta_1 = 0$. We also assume that all the power loads (also referred to as PQ loads) are constant i.e.

$$S_k = v_k i_k^* = P_k + jQ_k, \quad k = 1, \ldots, N \tag{6.8}$$

where $S_k \in \mathbb{C}$ is the (complex) power. Note that when $P_k > 0$ then the active power is injected into the node according to the current direction defined above. If no load is attached to a specific node k, as, for example, in the case of nodes connecting a lateral line with the main line, we can simply assume $S_k = 0$, which indirectly implies $i_k = 0$ since under normal grid operating conditions $v_k \neq 0$.

6.3.2 Linear power flow computation

The previous section defines the set of equations that voltage and current phasors need to satisfy in each node of the network. Let us define the complex column vectors $v = [v_2 \ \ldots \ v_N]^T \in \mathbb{C}^{N-1}$, $i = [i_2 \ \ldots \ i_N]^T \in \mathbb{C}^{N-1}$. Under assumption (6.7), then the

constraints given by Eqn. (6.6) can be equivalently rewritten as:

$$\underbrace{\begin{bmatrix} L_{11} & L_{12} \\ L_{21} & L \end{bmatrix}}_{L^+} \underbrace{\begin{bmatrix} v_1 \\ v \end{bmatrix}}_{v^+} = \underbrace{\begin{bmatrix} i_1 \\ i \end{bmatrix}}_{i^+} \Leftrightarrow \begin{array}{l} L_{21}V_1 + Lv = i \\ i_1 = -\sum_{k=2}^{N} i_k \end{array}$$

If the grid is connected, then $L \in \mathbb{C}$ is invertible, therefore we have $v = L^{-1}(i - L_{21}V_1)$. Since $L\mathbf{1}_N = \mathbf{1}_N$ and $v_1 = V_1$, then $L^{-1}L_{21} = -\mathbf{1}_N$, therefore the previous equation can be written as

$$v = V_1\mathbf{1}_N + L^{-1}i \tag{6.9}$$

If we define the complex column vector $S = [S_2 \ \dots \ S_N]^T \in \mathbb{C}^{N-1}$, then equations (6.7), (6.8) and (6.9) can be equivalently written as:

$$v_1 = V_1 \tag{6.10}$$

$$v \circ i^* = S \tag{6.11}$$

$$v - L^{-1}i = V_1\mathbf{1}_N \tag{6.12}$$

$$i_1 + \sum_{k=2}^{N} i_k = 0 \tag{6.13}$$

where the symbol "$\circ$" denotes the component-wise product and i^* is the component-wise complex conjugate of the current vector i. If the PCC voltage V_1 and the load vector S are known, then the previous equations represent a set of $2N$ (complex) nonlinear equations in $2N$ (complex) unknown variables $v_1, \dots, v_N, i_1, \dots, i_N$. The previous set of nonlinear equations may have no solutions or multiple solutions. Under the assumption that at least one feasible solution exists, the solution of the previous set of equations reduces to the problem of solving Eqn. (6.12) and Eqn. (6.11). One possible numerical procedure to compute a feasible solution (which is also the most efficient in terms of power loss over the lines) is expressed by Algorithm 2. This algorithm coincides with the forward-backward sweep method used to solve power flow equations [83] when the grid is radial, but it is somewhat more general since it can also be used for mesh networks. Alternative approaches for power flow analysis are the well-known Gauss-Seidel and Newton-Raphson methods. In the following, we adopted the proposed algorithm, since it also provides a link with the linear model approximation described below.

The power flow equations (6.10)-(6.13) are highly non-linear and this makes the problem of state estimation in the presence of noisy measurements and uncertainty very difficult and numerically intensive. Recently, a linear approximation has been proposed for modeling the power flow equations [81, 82]. This approximation can be obtained by

Algorithm 2 Power Flow computation

Require: $S \in \mathbb{C}^N, V_1 \in \mathbb{R}, r \in (0,1), T \in \mathbb{N}$

$v[0] = V_1 \mathbf{1}_N$

$\tau = 0$

repeat

  $\tau = \tau + 1$

  $i[\tau] = \frac{S^*}{v[\tau-1]}$ ▷ Component-wise division

  $v[\tau] = V_1 \mathbf{1}_N + L^{-1} i[\tau]$

  $S[\tau] = v[\tau] \circ i^*[\tau]$

until $\|S[\tau] - S\| < r\|s\|$ or $\tau > T$

if $\tau > T$ **then**

  No solution found

end if

stopping the power flow computation in Algorithm 2 after the first iteration, i.e.

$$i[1] \;=\; \frac{1}{V_1} S^*, \quad v[1] = V_1 \mathbf{1}_N + \frac{1}{V_1} L^{-1} S^*. \tag{6.14}$$

The previous two equations show that the current and the voltage phasors are approximately linear in the power loads S. Obviously, the linearization error is not zero, i.e. $e[1] := v - v[1] \neq 0$, v being the actual voltage vector of the grid nodes. However, it has been shown that if the term $\frac{\|L^{-1}\|\|S\|}{V_1^2}$ is sufficiently smaller than unity, then the linearization error is small. This assumption is acceptable whenever the voltage magnitude drop and the phase angle difference between the PCC and any node in the network are smaller that $5 - 10\%$ and $2 - 5^o$, respectively [84]. This approximation shares some similarities with the DC power flow model approximation [85]. However, the main difference is that in the DC power flow model, the resistance of the lines is assumed to be negligible, while in the linear model above the matrix L includes the resistive terms. While neglecting the resistive component in high-voltage transmission networks is a fair first order assumption, in low-voltage distribution networks this is not the case. Therefore, the linear model presented here may be more suitable for the distribution setting.

6.3.3 The Bayesian linear state estimator (BLSE)

In this section, the linear approximation of the power flow equations described in (6.14) is used to derive the best estimator in a Bayesian framework. More specifically, the prediction of active and reactive loads can be used to derive a-priori information about the statistical distributions of voltage phasors. Such distributions can be computed off-line and, once PMU measurements are available, they can be used to improve the estimates

of the true voltage phasors and to reduce the uncertainty given by the a-posteriori statistical distributions of the state estimation errors. By using a notation similar to that introduced in previous sections, we can denote with symbol $\sim$ the quantities that are actually measured to estimate the state. For instance, $\tilde{S}_k = \tilde{P}_k + j\tilde{Q}_k$, with $\tilde{P}_k = P_k + \varepsilon_{p_k}$ and $\tilde{Q}_k = Q_k + \varepsilon_{q_k}$ are the complex power injection measured at bus k. In the following, we will refer to σ_L as the relative standard deviation of load variations (that can be regarded also as standard uncertainty for the pseudo-measurements $\tilde{P}_k$ and $\tilde{Q}_k$). On the basis of the a-priori information about loads we obtain that:

$$v^0 := \mathbb{E}[v] = V_1 \mathbf{1}_N + \frac{1}{V_1} L^{-1} S^* \tag{6.15}$$

$$\Sigma_0 : = \mathbb{E}[(v - v^0)(v - v^0)^H] = \sigma_L^2 \frac{1}{V_1^2} L^{-1} \Sigma_s (L^{-1})^* \tag{6.16}$$

$$\Sigma_s = diag\{|\tilde{S}_1|^2, \ldots, |\tilde{S}_N|^2\} \tag{6.17}$$

where the symbol $()^H$ indicates the transpose and conjugate (i.e. Hermitian) operator. The previous estimator is the optimal estimator among all possible linear estimators based on pseudo-measurements. The vector v^0 corresponds to the nominal voltage phasors according to the load prediction and Σ_0 is the corresponding error covariance matrix. Note that, because pseudo-measurements are assumed to be available at all nodes, then the state of the grid is observable even without any PMU measurement. Adding PMU measurements will simply improve estimation performance. If a PMU measurement is available at node k, we define the complex measurement voltage phasor as

$$\tilde{v}_k = (V_k + \varepsilon_{v_k}) e^{j(\theta_k + \varepsilon_{\theta_k})} = v_k + \varepsilon_k^{rl} + \varepsilon_k^{im} \tag{6.18}$$

where ε^{rl} and ε^{im} are approximately independent and zero-mean uncertainty contributions. If, for the sake of simplicity, the uncertainties contributions of the real and the imaginary part of phasor measurement are supposed to be the same, we have that

$$\mathbb{E}[(\varepsilon_k^{rl})^2] = \mathbb{E}[(\varepsilon_k^{im})^2] = \sigma_{PMU}^2 V_1^2 \tag{6.19}$$

and

$$\mathbb{E}[\tilde{v}_k] = v_k, \mathbb{E}[|\tilde{v}_k - v_k^2|] = 2V_1^2 \sigma_{PMU}^2 \tag{6.20}$$

where σ_{PMU} is the standard relative uncertainty deviation. Thus, the PMU measurement provides an unbiased estimate of the true voltage phasor with variance twice as large as $V_1^2 \sigma_{PMU}^2$. If we finally define $\tilde{v}_{\mathcal{M}} := [\tilde{v}_{m_1} \cdots \tilde{v}_{m_P}] \in \mathbb{C}^P$, where P is the number of PMU, then we can write

$$\tilde{v}_{\mathcal{M}} = C_{\mathcal{M}} v + V_1 \varepsilon_{\mathcal{M}}^{rl} + j V_1 \varepsilon_{\mathcal{M}}^{im}, \tag{6.21}$$

$$\mathbb{E}[\varepsilon_{\mathcal{M}}^{rl} (\varepsilon_{\mathcal{M}}^{rl})^H] = \sigma_{PMU}^2 I_P \tag{6.22}$$

where $\varepsilon_{\mathcal{M}}^{rl}$ and $\varepsilon_{\mathcal{M}}^{im}$ are the measurement uncertainty terms associated with the PMUs belonging to set $\mathcal{M}$, I_P is the $P \times P$ identity matrix, and $C_{\mathcal{M}} \in \mathbb{R}^{P \times N}$ is a matrix whose ℓ-th row has all zeros except for the p_ℓ-th entry which is set to one. In practice $C_{\mathcal{M}}$ is a selection matrix that associates the PMU measurement $\tilde{v}_{m_\ell}$ with the corresponding voltage v_{m_ℓ}. In the context of Bayesian estimation, the optimal voltage estimate based on $\tilde{v}_{\mathcal{M}}$ and on the prior distribution v^0, is given by

$$\widehat{v} := E[v \,|\, \tilde{v}_{\mathcal{M}}] = v^0 + G(\tilde{v}_{\mathcal{M}} - C_{\mathcal{M}} v^0) \tag{6.23}$$

$$\Sigma_{\mathcal{M}} = \Sigma_0 - \underbrace{\Sigma_0 C_{\mathcal{M}}^T (C_{\mathcal{M}} \Sigma_0 C_{\mathcal{M}}^T + 2V_1^2 \sigma_{PMU}^2 I_K)^{-1}}_{G} C_{\mathcal{M}} \Sigma_0 \tag{6.24}$$

where $\Sigma_0 = E[(v - \widehat{v})(v - \widehat{v})^H]$. Note that the matrices G and $\Sigma_{\mathcal{M}}$ can be computed off-line, i.e. they do not depend on the actual PMU measurement vector $\tilde{v}_{\mathcal{M}}$. Therefore, the computation of (6.23) can be performed very rapidly on-line even for very large networks.

6.3.4 Simulation Results

In this section the proposed BLSE state estimator is compared with the classic WLS-based approach, whose behavior has been extensively analyzed before. The IEEE 33-node distribution network is the same as in the previous section, always shown in Fig. 6.1. The performance of BLSE and WLS estimators has been analyzed in Matlab by computing the parameter $RAMSE(\mathcal{M})$ defined in (A.2) over $MC = 1000$ Monte Carlo runs.

In the first test case the accuracy of BLSE and WLS is evaluated as a function of the relative uncertainty σ_L of the pseudo-measurements of active and reactive injected power, assuming that no PMUs are used. Fig. 6.6 reports the $RAMSE$ for both BLSE and WLS methods. At the beginning, the BSLE estimation accuracy is worse than WLS. However, the difference between the results of such techniques tends to decrease as σ_L increase. The figure also reports the theoretical $RAMSE$ curve of the BSLE estimator as it results from $RAMSE^{th} = \sqrt{\frac{1}{N} trace(\Sigma_0)}$. This looks slightly optimistic compared to the Monte-Carlo performance, probably because of the linearization error. The second test case, reported in Fig. 6.7, compares the accuracy of theoretical $RAMSE_{th}$ and the simulation results of BSLE and WLS using active and reactive power measurements with $\sigma_L = 0.5$ (50%) and an increasing number of PMUs with TVE=0.1 % placed using Algorithm 1. In all cases the σ_{PMU} values are computed starting from the maximum TVE ones, assuming that the uncertainty contributions on the real and imaginary parts are the same. The figure shows that the theoretical performance of $RMSE$ matches almost exactly the simulation results of both BSLE and WLS. The final test case, reported in Fig. 6.8, compares the accuracy of BSLE and WLS using active and reactive power measurements with $\sigma_L = 0.5$ (50%)

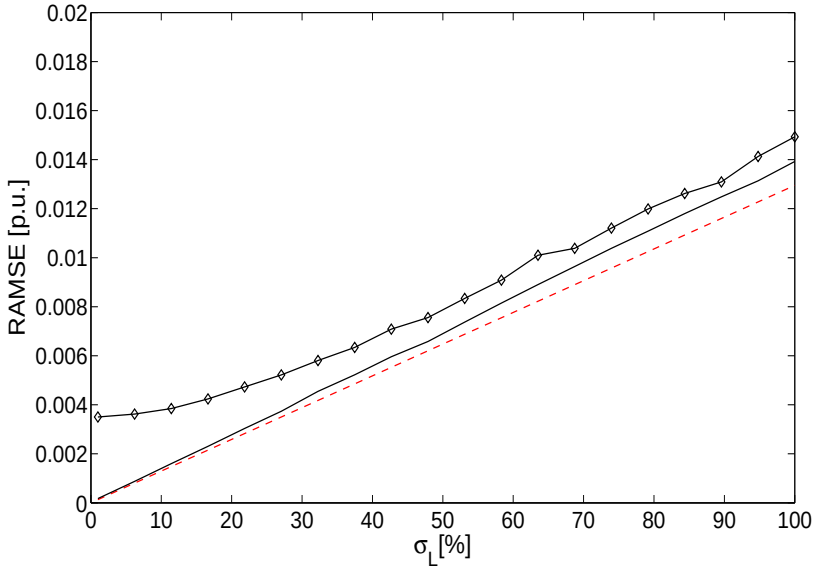

Figure 6.6: RAMSE voltage curves corresponding to different values of load standard deviation, σ_L, for theoretical RAMSE (red dashed line), BLSE (black solid line with markers) WLS (black solid line).

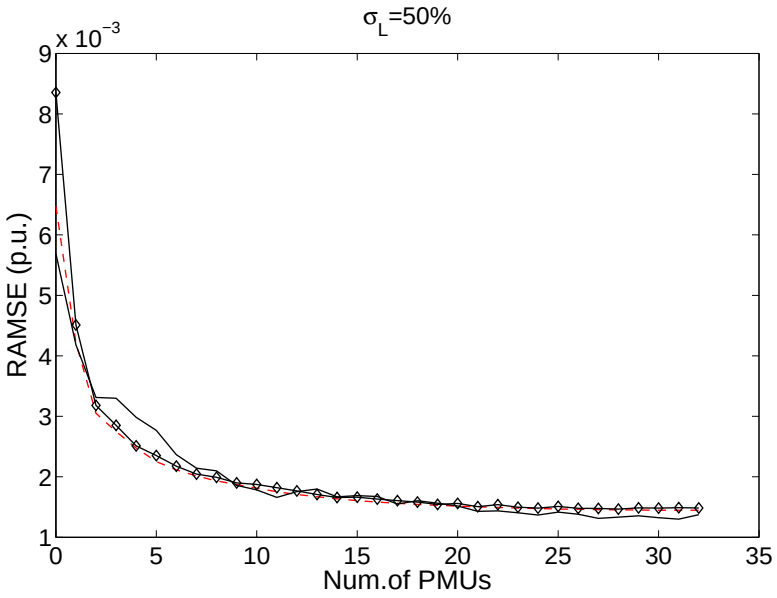

Figure 6.7: RAMSE curves as a function of number of PMUs. The relative uncertainty of pseudo-measurements is $\sigma_L = 0.5\%$. The curves are theoretical $RAMSE$ (red dashed line), BLSE (black solid line with markers) WLS (black solid line) for PMU accuracy 0.001 %. The instruments are positioned sequentially according to the greedy placement algorithm.

and TVE equal to 1%, 0.1% and 0.05% with an increasing number of PMUs placed using Algorithm 1.

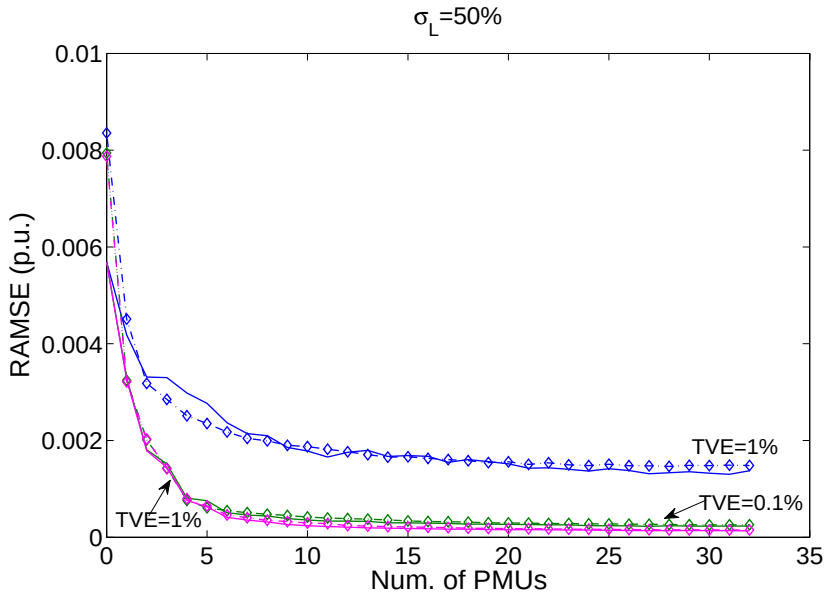

Figure 6.8: RAMSE curves as a function of number of PMUs. The relative uncertainty of pseudo-measurements is $\sigma_L = 0.5\%$. Simulation-based results associated with the BLSE(solid line with markers) and WLS (solid line) estimator for PMU with 1% (blue color), 0.1% (green color) or 0.01% (magenta color) accuracy. The instruments are positioned sequentially according to the greedy placement algorithm.

6.4 Conclusion

This chapter presents the impact of PMUs on distribution system state estimation based on the WLS algorithm and on a novel Bayesian linear approach. Once the system observability problem is solved, the benefit of using PMUs in state estimation is maximum when such instruments measure the state variables directly. In this case, the asymptotic estimation uncertainty strongly depends on instrumental accuracy. However, installing PMUs in more than about 1/3 of the network nodes is unnecessary, as this would not change performance noticeably regardless of the tolerance affecting line parameters.

In the second part of the chapter it is demonstrated that the proposed Bayesian linear state estimator (BLSE) provides the same performance as the standard WLS estimator but with a reduced computational burden. The main novelty of this approach is that its performances can be computed off-line and can be used to address several problems such as optimal PMU placement or trade-offs between number of PMUs versus their accuracy, without running extensive Monte-Carlo simulations. Moreover, because the estimation error in distribution systems tends to be dominated by uncertainty in loads and scarcity of instrumented nodes, the linearized method along with the use of high precision PMUs may be a suitable way to facilitate on-line state estimation where it was previously impractical. Future research direction include the extension of the proposed

strategy to unbalanced three-phase networks, large scale networks, possibly using dynamic state estimation techniques such as Kalman filters.

Chapter 7

Conclusions

In modern power systems frequency, amplitude and phase of electrical waveforms are subjected to quick and significant changes as well as to heavy disturbances due to the increasing presence of distributed generators, storage systems and large nonlinear loads, e.g. electric vehicles. As the penetration of these technologies grows, further and more critical dynamic conditions are expected in the grid, particularly at the distribution level. As a result, distribution networks will shift from the traditional purely passive, unidirectional and consumer-oriented structure towards a bidirectional power flow paradigm, thus becoming more similar to transmission networks.

In this context, the PMUs will play a relevant role in enhancing the next-generation wide-area measurement systems (WAMS). The synchrophasor measurement data provided by PMUs are usually affected by different uncertainty sources, such as instrument transformer contributions, magnitude and phase distortion due to the front-end acquisition stage, quantization noise, ADC nonlinear distortion, synchronization jitter, and errors due to the specific estimation algorithm employed. In order to meet the high accuracy requirements of next-generation active distribution networks, minimizing the uncertainty contributions due to the signal processing algorithm both under static and dynamic conditions is essential. In addition, responsiveness under the effect of transients (e.g. step-like changes) and computational complexity are extremely important for real-time monitoring.

The first part of this thesis is completely focused on the issues above. Starting from an introduction about the definition and the meaning of synchrophasor, in Chapter 2 useful guidelines to design the filter for the general PMU architecture suggested in the IEEE Standard C37.118.1 are proposed. Such criteria are used to meet some of the accuracy requirements described in the Standard in static and dynamic conditions for protection and measurement applications respectively. In Chapter 3 an exhaustive analysis of four selected state-of-art phasor estimators is performed. The simulation results in several testing conditions (i.e. static off-nominal frequency offset only, amplitude and phase

modulation, wide-band noise, harmonics, amplitude or phase step, frequency ramp) show that the dynamic phasor model (i.e. modeling also the phasor variations by considering the first 2 or 3 terms of the phasor Taylor's series expansion around the reference time) generally returns much better results, especially in the presence of amplitude or phase modulations. Among the considered dynamic estimators, the so-called Taylor Weighted Least Squares (TWLS) method ensures high accuracy, is optimal under the influence of noise and exhibits suitable response times after step changes in amplitude or in phase. However, it is still quite sensitive to harmonics (especially the second-order one), inter-harmonics and does not compensate perfectly the effect of static off-nominal frequency deviations. These problems are partially addressed by the synchrophasor estimation algorithm called IpD^{2}FT and presented in Chapter 4, which is still based on the same Taylor phasor dynamic model used for TWLS, but relies on three frequency samples around the fundamental and is able to estimate and to compensate iteratively the effect of off-nominal frequency offsets. After an analytical description of the algorithm, this technique has been evaluated under the same testing conditions considered in Chapter 3. The results show that its performances in dynamic conditions are slightly worse than those of the TWLS estimator, especially when the observation interval length grows. However, the IpD^{2}FT behaves generally better when just off-nominal frequency offsets and harmonics are considered, as expected. In general, the TVE accuracy requirements reported in the Standard are met in most conditions just using observation intervals of a few nominal cycles, with the only exception of the out-of-band inter-harmonics disturbances that require longer intervals to be removed. Moreover, the IpD^{2}FT estimator exhibits good responsiveness in transient conditions and a higher, but still reasonable, computational complexity, since three iterations are usually enough for convergence. Due to the relevance that phase measurements have recently gained at the distribution level, the phasor angle estimation accuracy of the IpD^{2}FT algorithm has been also analyzed and compared with the accuracy of other techniques. Again, the simulation results show that the IpD^{2}FT algorithm performs slightly better than the TWLS estimator in static conditions and slightly worse in dynamic conditions. Nonetheless, it could be a good candidate for phasor angle measurement in distribution networks.

In the second part of the thesis a complementary problem is studied, i.e. the role and the impact of PMUs on grid state estimation. After shortly recalling the problem of state estimation based on the classic Weighted Least Squares (WLS) approach, in Chapter 5 the sensitivity of the WLS-based state estimator to the uncertainty of different types of measurements is analyzed theoretically. The proposed analysis, even if with some limitations (due mainly to the fact that all measurements are assumed to be affected by the same relative standard uncertainty) provides a useful criterion to choose a minimum set

of measurements able to minimize the mean or maximum growth rate of state estimation uncertainty. The results of a heuristic optimization procedure in a simple case study show, quite interestingly, that the use of PMUs does not necessarily minimize the sensitivity to measurement uncertainty. Indeed, if the uncertainty values are comparable, a suitable mixture of PMU-based and other measurements can further improve state estimation accuracy. In Chapter 6 the impact of PMUs on distribution system state estimation based on the WLS method is investigated more in detail. Moreover, a novel linear Bayesian state estimator is proposed. The main results related to this topic can be summarized as follows: (i) the number of deployed PMUs is less important than their accuracy, i.e. a lower number of more accurate PMUs ensures generally better state estimation results than many and less accurate PMUs; (ii) if we assume that network observability is ensured by pseudo-measurements, installing PMUs and that each PMU measures just one voltage or one current only, in more than about 1/3 of the network nodes is unnecessary, as the state estimation uncertainty does not improve noticeably if additional PMUs are deployed, even when the tolerances of line parameters are significant; (iii) the linear Bayesian state estimator, despite the linearization error which can influence estimation results in almost nominal load conditions, is generally so accurate as the WLS estimator, but it has the advantage to be faster; a feature that could be relevant for active distribution networks.

At the moment various research activities are ongoing. In the area of synchrophasor algorithms for PMUs, the main idea is to use both the least-squares approach of the TWLS and the iterative frequency estimation and compensation scheme of the IpD^{2}FT technique in order to exploit the benefits of both solutions. This could improve performances in both static and dynamic conditions. It is worth emphasizing that the testing conditions described in the IEEE Standard C37.118.1 were mainly defined for transmission systems. The level of disturbances and the amount of amplitude, frequency and phase fluctuations in the case of distribution networks are still unclear and they are a subject of active research in the scientific community. Investigating this topic is of paramount importance to understand in which conditions the existing PMU technologies are acceptable or to what extent algorithms and instruments have to be improved further. For instance, DC decaying offsets are expected to be large and likely in distribution networks. For this reason, recently some attempts have been done to include this additional type of disturbances in the measurement model. As far as the use of PMUs for state estimation is concerned, the proposed uncertainty sensitivity analysis has to be extended to the case of an arbitrary number of measurement points, with no restrictions on the uncertainty level. An analysis of this kind could provide an interesting and deeper insight on the impact of PMUs on state estimation accuracy, thus extending the results and conclusions reported in Chapter 6.

Appendix A

Grid Network parameters

A.1 Network 15-bus

Table A.1: Branch data of the 15-bus distribution network described in [66].

Branch no.	**From bus**	**To bus**	$\boldsymbol{r}$ [Ω]	$\boldsymbol{x}$ [Ω]
1	1	2	1.3531	1.3235
2	2	3	1.1702	1.1446
3	3	4	0.8411	0.8227
4	4	5	1.5235	1.0276
5	2	9	2.0132	1.3579
6	9	10	1.6867	1.1377
7	2	6	2.5573	1.7249
8	6	7	1.0882	0.7340
9	6	8	1.2514	0.8441
10	3	11	1.7955	1.2111
11	11	12	2.4485	1.6515
12	12	13	2.0132	1.3579
13	4	14	2.2308	1.5047
14	4	15	1.1970	0.8074

Table A.2: Nominal real and reactive loads [66].

Bus no.	$\mathbf{P}_L$ **[kW]**	$\mathbf{Q}_L$**[kvar]**
1 (feeder)	0.0	0.0
2	44.1	44.7
3	70.0	71.0
4	140.0	142.0
5	44.1	44.7
6	140.0	142.0
7	140.0	142.0
8	70.0	71.0
9	70.0	71.0
10	44.1	44.7
11	140.0	142.0
12	70.0	71.0
13	44.1	44.7
14	70.0	71.0
15	140.0	142.0

A.2 IEEE 33-bus

Table A.3: Bus connections and line resistance/reactance values of the IEEE 33-bus radial distribution network.

Branch no.	**From bus**	**To bus**	$\boldsymbol{r}$ [Ω]	$\boldsymbol{x}$ [Ω]
1	1	2	0.0922	0.047
2	2	3	0.493	0.2511
3	3	4	0.366	0.1864
4	4	5	0.3811	0.1941
5	5	6	0.819	0.707
6	6	7	0.1872	0.6188
7	7	8	0.7114	0.2351
8	8	9	1.03	0.74
9	9	10	1.044	0.74
10	10	11	0.1966	0.065
11	11	12	0.3744	0.1298
12	12	13	1.468	1.155
13	13	14	0.5416	0.7129
14	14	15	0.591	0.526
15	15	16	0.7463	0.545
16	16	17	1.289	1.721
17	17	18	0.732	0.574
18	2	19	0.164	0.1565
19	19	20	1.5042	1.3554
20	20	21	0.4095	0.4784
21	21	22	0.7089	0.9373
22	3	23	0.4512	0.3083
23	23	24	0.898	0.7091
24	24	25	0.896	0.7011
25	6	26	0.203	0.1034
26	26	27	0.2842	0.1447
27	27	28	1.059	0.9337
28	28	29	0.8042	0.7006
29	29	30	0.5075	0.2585
30	30	31	0.9744	0.963
31	31	32	0.3105	0.3619
32	32	33	0.341	0.5302

Table A.4: Real and reactive nominal power loads of the IEEE 33-bus radial distribution network.

Bus no.	$\boldsymbol{P}_L$ [kW]	$\boldsymbol{Q}_L$ [kvar]
1	0	0
2	100	60
3	90	40
4	120	80
5	60	30
6	60	20
7	200	100
8	200	100
9	60	20
10	60	20
11	45	30
12	60	35
13	60	35
14	120	80
15	60	10
16	60	20
17	60	20
18	90	40
19	90	40
20	90	40
21	90	40
22	90	40
23	90	50
24	420	200
25	420	200
26	60	25
27	60	25
28	60	20
29	120	70
30	200	600
31	150	70
32	210	100
33	60	40

Bibliography

[1] M. Amin and J. Stringer, "The electric power grid: Today and tomorrow," *MRS Bulletin*, vol. 33, pp. 399–407, Apr. 2008.

[2] F. Rahimi and A. Ipakchi, "Demand response as a market resource under the smart grid paradigm," *Smart Grid, IEEE Transactions on*, vol. 1, no. 1, pp. 82–88, June 2010.

[3] A. Keyhani, *Design of Smart Power Grid Renewable Energy Systems*, July 2011.

[4] Report, "An interdisciplinary mit study, the future of electric grid," Dec. 2011.

[5] L. Peretto, "The role of measurements in the smart grid era," *Instrumentation Measurement Magazine, IEEE*, vol. 13, no. 3, pp. 22–25, June 2010.

[6] A. Padke and J. Thorp, *Synchronized Phasor Measurements and Their Applications*. Springer, 2008.

[7] Yih-Fang Huang, S. Werner, Jing Huang, N. Kashyap, and V. Gupta, "State estimation in electric power grids: Meeting new challenges presented by the requirements of the future grid," *IEEE Signal Processing Magazine*, vol. 29, no. 5, pp. 33–43, Sep. 2012.

[8] E. Schweitzer, D. Whitehead, G. Zweigle, K. Ravikumar, and G. Rzepka, "Synchrophasor-based power system protection and control applications," in *Modern Electric Power Systems (MEPS), 2010 Proceedings of the International Symposium*, Sept 2010, pp. 1–10.

[9] G. Liu, J. Quintero, and V. Venkatasubramanian, "Oscillation monitoring system based on wide area synchrophasors in power systems," in *Bulk Power System Dynamics and Control - VII. Revitalizing Operational Reliability, 2007 iREP Symposium*, Aug 2007, pp. 1–13.

[10] S. Corsi and G. Taranto, "A real-time voltage instability identification algorithm based on local phasor measurements," *Power Systems, IEEE Transactions on*, vol. 23, no. 3, pp. 1271–1279, Aug 2008.

[11] C.-S. Yu, C.-W. Liu, S.-L. Yu, and J.-A. Jiang, "A new pmu-based fault location algorithm for series compensated lines," *Power Delivery, IEEE Transactions on*, vol. 17, no. 1, pp. 33–46, Jan 2002.

[12] M. Ropp, S. Perlenfein, D. Joshi, C. Mettler, M. Mills-Price, M. Scharf, K. Gubba Ravikumar, and G. Zweigle, "Synchrophasors for island detection," in *Photovoltaic Specialists Conference (PVSC), 2012 38th IEEE*, June 2012, pp. 000 602–000 607.

[13] A. Borghetti and L. Peretto, "Power system islands, autonomous microgrids and relevant instrumentation," in *Innovative Smart Grid Technologies (ISGT), 2012 IEEE PES*, Jan 2012, pp. 1–7.

[14] N. Abbasy and H. Ismail, "A unified approach for the optimal pmu location for power system state estimation," *Power Systems, IEEE Transactions on*, vol. 24, no. 2, pp. 806–813, May 2009.

[15] V. Vignesh, S. Chakrabarti, and S. Srivastava, "An experimental study on the load modelling using pmu measurements," in *T D Conference and Exposition, 2014 IEEE PES*, April 2014, pp. 1–5.

[16] F. Steinhauser, C. Riesch, and M. Rudigier, "Ieee 1588 for time synchronization of devices in the electric power industry," in *Precision Clock Synchronization for Measurement Control and Communication (ISPCS), 2010 International IEEE Symposium on*, Sept 2010, pp. 1–6.

[17] "Ieee standard for synchrophasor data transfer for power systems," *IEEE Std C37.118.2-2011 (Revision of IEEE Std C37.118-2005)*, pp. 1–53, Dec 2011.

[18] "Ieee standard for synchrophasor measurements for power systems," *IEEE Std C37.118.1-2011 (Revision of IEEE Std C37.118-2005)*, pp. 1–61, Dec 2011.

[19] D. Macii, D. Petri, and A. Zorat, "Accuracy analysis and enhancement of dft-based synchrophasor estimators in off-nominal conditions," *Instrumentation and Measurement, IEEE Transactions on*, vol. 61, no. 10, pp. 2653–2664, Oct 2012.

[20] de la O JA, H. Altuve, and I. Diaz, "A new digital filter for phasor computation. i. theory," in *Power Industry Computer Applications., 1997. 20th International Conference on*, May 1997, pp. 78–83.

[21] H. Altuve, I. Diaz, and de la O JA, "A new digital filter for phasor computation. ii. evaluation," in *Power Industry Computer Applications., 1997. 20th International Conference on*, May 1997, pp. 84–89.

[22] J. de la O Serna, "Reducing the delay of phasor estimates under power system oscillations," *Instrumentation and Measurement, IEEE Transactions on*, vol. 56, no. 6, pp. 2271–2278, Dec 2007.

[23] A. Roscoe, I. Abdulhadi, and G. Burt, "P-class phasor measurement unit algorithms using adaptive filtering to enhance accuracy at off-nominal frequencies," in *Smart Measurements for Future Grids (SMFG), 2011 IEEE International Conference on*, Nov 2011, pp. 51–58.

[24] ——, "Filters for m class phasor measurement units," in *Applied Measurements for Power Systems (AMPS), 2012 IEEE International Workshop on*, Sept 2012, pp. 1–6.

[25] J. G. Proakis and M. Salehi, *Communication Systems Engineering*. Prentice Hall Int., 1994.

[26] J. de la O Serna and K. Martin, "Improving phasor measurements under power system oscillations," *Power Systems, IEEE Transactions on*, vol. 18, no. 1, pp. 160–166, Feb 2003.

[27] D. Belega and D. Petri, "Accuracy analysis of the multicycle synchrophasor estimator provided by the interpolated dft algorithm," *Instrumentation and Measurement, IEEE Transactions on*, vol. 62, no. 5, pp. 942–953, May 2013.

[28] T. Sidhu, X. Zhang, and V. Balamourougan, "A new half-cycle phasor estimation algorithm," *Power Delivery, IEEE Transactions on*, vol. 20, no. 2, pp. 1299–1305, April 2005.

[29] C.-S. Yu, Y.-S. Huang, and J.-A. Jiang, "A full- and half-cycle dft-based technique for fault current filtering," in *Industrial Technology (ICIT), 2010 IEEE International Conference on*, March 2010, pp. 859–864.

[30] M. Akke and J. Thorp, "Sample value adjustment improves phasor estimation at off-nominal frequencies," *Power Delivery, IEEE Transactions on*, vol. 25, no. 4, pp. 2255–2263, Oct 2010.

[31] J. Warichet, T. Sezi, and J. Maun, "Considerations about synchrophasors measurement in dynamic system conditions," *International Journal of Electrical Power Energy Systems*, vol. 31, no. 9, pp. 452 – 464, 2009.

[32] B. Zeng, Z. Teng, Y. Cai, S. Guo, and B. Qing, "Harmonic phasor analysis based on improved fft algorithm," *Smart Grid, IEEE Transactions on*, vol. 2, no. 1, pp. 51–59, March 2011.

[33] R. Mai, Z. He, L. Fu, B. Kirby, and Z. Q. Bo, "A dynamic synchrophasor estimation algorithm for online application," *Power Delivery, IEEE Transactions on*, vol. 25, no. 2, pp. 570–578, April 2010.

[34] W. Premerlani, B. Kasztenny, and M. Adamiak, "Development and implementation of a synchrophasor estimator capable of measurements under dynamic conditions," *Power Delivery, IEEE Transactions on*, vol. 23, no. 1, pp. 109–123, Jan 2008.

[35] J. de la O Serna and K. Martin, "Improving phasor measurements under power system oscillations," *Power Systems, IEEE Transactions on*, vol. 18, no. 1, pp. 160–166, Feb 2003.

[36] M. Platas-Garza and J. de la O Serna, "Dynamic phasor and frequency estimates through maximally flat differentiators," *Instrumentation and Measurement, IEEE Transactions on*, vol. 59, no. 7, pp. 1803–1811, July 2010.

[37] P. Castello, C. Muscas, and P. Pegoraro, "Performance comparison of algorithms for synchrophasors measurements under dynamic conditions," in *Applied Measurements for Power Systems (AMPS), 2011 IEEE International Workshop on*, Sept 2011, pp. 25–30.

[38] P. Castello, M. Lixia, C. Muscas, and P. Pegoraro, "Impact of the model on the accuracy of synchrophasor measurement," *Instrumentation and Measurement, IEEE Transactions on*, vol. 61, no. 8, pp. 2179–2188, Aug 2012.

[39] J. de la Serna, "Dynamic phasor estimates for power system oscillations," *Instrumentation and Measurement, IEEE Transactions on*, vol. 56, no. 5, pp. 1648–1657, Oct 2007.

[40] G. Barchi, D. Macii, and D. Petri, "Synchrophasor estimators accuracy: A comparative analysis," *Instrumentation and Measurement, IEEE Transactions on*, vol. 62, no. 5, pp. 963–973, May 2013.

[41] D. Petri, D. Fontanelli, and D. Macii, "A frequency-domain algorithm for dynamic synchrophasor and frequency estimation," *Instrumentation and Measurement, IEEE Transactions on*, vol. 63, no. 10, pp. 2330–2340, Oct 2014.

[42] D. Belega and D. Petri, "Accuracy analysis of the multicycle synchrophasor estimator provided by the interpolated dft algorithm," *Instrumentation and Measurement, IEEE Transactions on*, vol. 62, no. 5, pp. 942–953, May 2013.

[43] A. H. Nuttall, "Some windows with very good sidelobe behavior," *Acoustics, Speech and Signal Processing, IEEE Transactions on*, vol. 29, no. 1, pp. 84–91, Feb 1981.

[44] D. Belega, D. Macii, and D. Petri, "Fast synchrophasor estimation by means of frequency-domain and time-domain algorithms," *Instrumentation and Measurement, IEEE Transactions on*, vol. 63, no. 2, pp. 388–401, Feb 2014.

[45] M. Paolone, A. Borghetti, and C. Nucci, "A synchrophasor estimation algorithm for the monitoring of active distribution networks in steady state and transient conditions," in *Power Systems Computation Conference (PSCC), Stockholm, Sweden,*, Aug. 2011.

[46] "Ieee standard for synchrophasor measurements for power systems – amendment 1: Modification of selected performance requirements," *IEEE Std C37.118.1a-2014 (Amendment to IEEE Std C37.118.1-2011)*, pp. 1–25, April 2014.

[47] L. Ochoa and D. Wilson, "Angle constraint active management of distribution networks with wind power," in *Innovative Smart Grid Technologies Conference Europe (ISGT Europe), 2010 IEEE PES*, Oct 2010, pp. 1–5.

[48] A. Borghetti, C. Nucci, M. Paolone, G. Ciappi, and A. Solari, "Synchronized phasors monitoring during the islanding maneuver of an active distribution network," *IEEE Transactions on Smart Grid*, vol. 2, no. 1, pp. 82–91, Mar. 2011.

[49] A. von Meier, D. Culler, A. McEachern, and R. Arghandeh, "Micro-synchrophasors for distribution systems," in *IEEE PES Innovative Smart Grid Technologies Conference (ISGT)*, Feb. 2014, pp. 1–5.

[50] "Ieee standard requirements for instrument transformers." *IEEE Std C57.13-1993*, pp. i–, Mar 1994.

[51] P. Ferrari, A. Flammini, S. Rinaldi, and G. Prytz, "Evaluation of time gateways for synchronization of substation automation systems," *Instrumentation and Measurement, IEEE Transactions on*, vol. 61, no. 10, pp. 2612–2621, Oct 2012.

[52] A. Roscoe, I. Abdulhadi, and G. Burt, "P and m class phasor measurement unit algorithms using adaptive cascaded filters," *Power Delivery, IEEE Transactions on*, vol. 28, no. 3, pp. 1447–1459, July 2013.

[53] "Voltage characteristics of electricity supplied by public electricity distribution networks," *IEC EN 50160 Standard*, November 1994.

[54] P. Romano and M. Paolone, "Enhanced interpolated-dft for synchrophasor estimation in fpgas: Theory, implementation, and validation of a pmu prototype," *Instrumentation and Measurement, IEEE Transactions on*, vol. PP, no. 99, pp. 1–1, 2014.

[55] C. De Dominicis, P. Ferrari, A. Flammini, S. Rinaldi, and M. Quarantelli, "On the use of ieee 1588 in existing iec 61850-based sass: Current behavior and future challenges," *Instrumentation and Measurement, IEEE Transactions on*, vol. 60, no. 9, pp. 3070–3081, Sept 2011.

[56] K. Moslehi and R. Kumar, "A reliability perspective of the smart grid," *IEEE Transactions on Smart Grid*, vol. 1, no. 1, pp. 57–64, Jun. 2010.

[57] T. Stuart and C. Herczet, "A sensitivity analysis of weighted least squares state estimation for power systems," *IEEE Transactions on Power Apparatus and Systems*, vol. PAS-92, no. 5, pp. 1696–1701, Sep. 1973.

[58] R. Minguez and A. Conejo, "State estimation sensitivity analysis," *IEEE Transactions on Power Systems*, vol. 22, no. 3, pp. 1080–1091, Aug. 2007.

[59] A. Abur and A. Exposito, *Power System State Estimation (Theory and Implementation)*. Marcel Dekker, 2004.

[60] S. Sarri, M. Paolone, R. Cherkaoui, A. Borghetti, F. Napolitano, and C. Nucci, "State estimation of active distribution networks: Comparison between wls and iterated kalman-filter algorithm integrating pmus," in *Innovative Smart Grid Technologies (ISGT Europe), 2012 3rd IEEE PES International Conference and Exhibition on*, Oct 2012, pp. 1–8.

[61] M. Baran and A. Kelley, "State estimation for real-time monitoring of distribution systems," *IEEE Transactions on Power Systems*, vol. 9, no. 3, pp. 1601–1609, Aug. 1994.

[62] ——, "A branch-current-based state estimation method for distribution systems," *IEEE Transactions on Power Systems*, vol. 10, no. 1, pp. 483–491, Feb. 1995.

[63] H. Wang and N. Schulz, "A revised branch current-based distribution system state estimation algorithm and meter placement impact," *IEEE Transactions on Power Systems*, vol. 19, no. 1, pp. 207–213, Feb. 2004.

[64] Whei-Min Lin, Jen-Hao Teng, and Shi-Jaw Chen, "A highly efficient algorithm in treating current measurements for the branch-current-based distribution state estimation," *IEEE Transactions on Power Delivery*, vol. 16, no. 3, pp. 433–439, Jul. 2001.

[65] C. Audet and J. E. Dennis Jr., "Analysis of generalized pattern searches," *SIAM Journal on Optimization*, vol. 13, no. 3, pp. 889–903, Aug. 2002.

[66] D. Das, D. Kothari, and A. Kalam, "Simple and efficient method for load flow solution of radial distribution networks," *International Journal of Electrical Power and Energy Systems*, vol. 17, no. 5, pp. 335 – 346, Oct. 1995.

[67] P. Pegoraro and S. Sulis, "On the uncertainty evaluation in distribution system state estimation," in *Proc. IEEE International Conference on Smart Measurements for Future Grids (SMFG)*, Bologna, Italy, Nov. 2011, pp. 59–63.

[68] R. Zimmerman, C. Murillo-Sanchez, and R. Thomas, "Matpower's extensible optimal power flow architecture," in *Proc. IEEE Power Energy Society General Meeting (PES '09)*, Calgary, Canada, Jul. 2009, pp. 1–7.

[69] J. T. A. Phadke and K. Karimi, "State estimation with phasor measurements," *IEEE Transactions on Power Systems*, vol. 1, pp. 233–238, 1986.

[70] M. Zhou, V. Centeno, J. Thorp, and A. Phadke, "An alternative for including phasor measurements in state estimators," *Power Systems, IEEE Transactions on*, vol. 21, no. 4, pp. 1930–1937, Nov 2006.

[71] N. Manousakis, G. Korres, and P. Georgilakis, "Taxonomy of pmu placement methodologies," *Power Systems, IEEE Transactions on*, vol. 27, no. 2, pp. 1070–1077, May 2012.

[72] J. Liu, J. Tang, F. Ponci, A. Monti, C. Muscas, and P. Pegoraro, "Trade-offs in pmu deployment for state estimation in active distribution grids," *IEEE Transactions on Smart Grid*, vol. 3, no. 2, pp. 915–924, Jun. 2012.

[73] D. Laverty, R. Best, P. Brogan, I. Al Khatib, L. Vanfretti, and D. Morrow, "The openPMU platform for open-source phasor measurements," *IEEE Transactions on Instrumentation and Measurement*, vol. 62, no. 4, pp. 701–709, Apr. 2013.

[74] C. Lu, J. Teng, and W.-H. Liu, "Distribution system state estimation," *IEEE Transactions on Power Systems*, vol. 10, pp. 229–240, 1995.

[75] D. Haughton and G. Heydt, "A linear state estimation formulation for smart distribution systems," *IEEE Transactions on Power Systems*, vol. 28, no. 2, pp. 1187–1195, 2013.

[76] P. Janssen, T.Sezi, and J.-C. Maun, "Distribution system state estimation using unsynchronized phasor measurements," in *Proceedings of IEEE Innovative Smart Grid Technologies Conference Europe (ISGT2012 Europe)*, 2012.

[77] W. Yuill, A. Edwards, S. Chowdhury, and S. P. Chowdhury, "Optimal pmu placement: A comprehensive literature review," in *IEEE Power and Energy Society General Meeting*, San Diego, CA, USA, Jul. 2011, pp. 1–8.

[78] P. Babu, C. P. Rakesh, M. Kumar, G. Srikanth, and D. Reddy, "A novel approach for solving distribution networks," in *Proc. 2009 Annual IEEE India Conference (INDICON)*, Gujarat, India, Dec. 2009, pp. 1–5.

[79] R. Singh, B. Pal, and R. Jabr, "Statistical representation of distribution system loads using gaussian mixture model," *IEEE Transactions on Power Systems*, vol. 25, no. 1, pp. 29–37, Feb. 2010.

[80] G. D'Antona and M. Davoudi, "Effect of phasor measurement unit on power state estimation considering parameters uncertainty," in *Proc. IEEE International Workshop on Applied Measurements for Power Systems (AMPS)*, Aachen, Germany, Sep. 2012, pp. 1–5.

[81] S. Bolognani and S. Zampieri, "A distributed control strategy for reactive power compensation in smart microgrids," *IEEE Transactions on Automatic Control*, vol. 58, no. 11, pp. 2818–2833, 2013.

[82] ——, "On the existence and linear approximation of the power flow solution in power distribution networks," University of Padova, Technical report (available on http://arxiv.org, 2014.

[83] U. Eminoglua and M. Hocaoglub, "Distribution systems forward/backward sweep-based power flow algorithms: A review and comparison study," *Electric Power Components and Systems*, vol. 37, no. 1, pp. 91–110, 2008.

[84] W. H. Kersting, "Radial distribution test feeders," in *IEEE Power Engineering Society Winter Meeting*, vol. 2, 2001, pp. 908–912.

[85] K. Purchala, L. Meeus, D. Van Dommelen, and R. Belmans, "Usefulness of dc power flow for active power flow analysis," in *Power Engineering Society General Meeting, 2005. IEEE*, June 2005, pp. 454–459 Vol. 1.

List of Tables

List of Figures